MICROTUBULE GEOMETRY AND THERMAL MODULATION OF MOLECULAR MOTORS TUG-OF-WAR

by

Olaolu Abiola Osunbayo

A dissertation submitted to the faculty of
The University of Utah
in partial fulfillment of the requirements for the degree of

Doctor of Philosophy

Department of Biology

The University of Utah

December 2017

The University of Utah Graduate School

STATEMENT OF DISSERTATION APPROVAL

The dissertation of **Olaolu Abiola Osunbayo**

has been approved by the following supervisory committee members:

Michael Vershinin	, Chair	**08/16/2017** Date Approved
Markus Babst	, Member	**8/18/2017** Date Approved
Julie Hollien	, Member	**8/18/2017** Date Approved
Alla Borisyuk	, Member	**8/21/2017** Date Approved
Saveez Saffarian	, Member	**8/12/2017** Date Approved

and by **Denise Dearing** , Chair/Dean of

the Department/College/School of **Biology**

and by David B. Kieda, Dean of The Graduate School.

ABSTRACT

The majority of studies of intracellular transport have focused on cargos that move well over some distance. However, a significant percentage of intracellular cargos at any given time remain in a stalled or locally diffusive state. The goal of my graduate work was to study the processes that lead to localized non-motile or weakly motile cargos.

In my first work (Chapter 2), I showed that cargos driven by a team of kinesins can spend a significant amount of time at microtubule (MT) intersections, especially when the intersecting MTs are counter-aligned. The work in Chapter 2 was done in two dimensions (2D) with MT attached to the surface of a coverslip. To enable more biologically faithful studies, I contributed to the development of a novel technique (Chapter 3) to manipulate MTs in three dimensions (3D). This work now enables the construction of MT structures in a controlled environment in a fully suspended geometry.

The study in Chapter 4 was motivated by the need to understand cold block of MT-based transport seen in some mammalian neurons and how this is overcome in cold adapted organisms. I have explored the differences in how temperature affects the activity of biological motors and helped model how these differences modulate the tug-of-war between the two opposite directed motors.

Lastly, it is critical in the study of nearly immotile cargos to distinguish when the cargo is not moving due to opposite-directed motor activity from when it is driven by a thermally-driven random process such as Brownian diffusion. I showed (Chapter 5) that

in contrast to diffusion, tug-of-war follows Arrhenius kinetics which reflects motor activation energy. I used a bi-directional kinesin NCD N340K mutant, on a single MT *in-vitro.* I also showed that this system of tug-of-war displays complex behavior. In contrast to thermal diffusion, this tug-of-war is sub-diffusive at short time intervals and it only becomes effectively diffusive at longer time intervals. In addition, I showed that the tug-of-war leads to an unexpected skewed distribution of diffusion coefficients within experimental sample range and I have helped develop a theoretical understanding of how this could arise in my model system.

To the loving memory of my father, Morakinyo Cornelius Osunbayo.

To my mother, Eunice Olayemi Osunbayo, who has been there for me all my life.

To my wife, Nnenna Osunbayo, for her support.

To my daughter, Toluwani Osunbayo.

TABLE OF CONTENTS

LIST OF FIGURES

Figures

ACKNOWLEDGMENTS

I will start by acknowledging my advisor, Dr. Michael Vershinin, without whom there could not have been this dissertation. Thank you for accepting me as your student. Thank you for your patience and mentoring. I could not have asked for a better mentor. You are the best.

I am also very grateful for the participation and mentoring by my committee members: Dr. Markus Babst, Dr. Julie Hollien, Dr. Saveez Saffarian, and Dr. Alla Borisyuk. Thank you for being there for me over the years.

I would also acknowledge my former and current lab mates: Weili Hong, Jared Bergman, Florence Doval, Abhimanyu Sharma, and Michael Shaw. Thank you all for your assistance along the way. My gratitude also goes to my collaborator, Chris Miles.

Lastly, I am very grateful for the support and the understanding of my family.

CHAPTER 1

INTRODUCTION

A eukaryotic cell is a complex, densely crowded environment. Like a huge metropolis, it critically needs efficient transportation to control the distribution of cellular components in a manner that is both spatially and temporally optimal. The principal enabler of the long-distance transport in the cell is the microtubules (MT)-based transport system. The MT system is involved in the routing and distribution of components within the cell body and in inter-flagellar transport [1–3]. The breakdown of the MT transport system is deeply involved in and may even be causative for diseases like Lissencephaly and Alzheimer's [4–7].

Transport in the cell is often naively envisioned as a cannonball run between origin and destination but in reality, it is complicated by a variety of factors. This dissertation is focused on the complications. One important factor is the complex geometry of MTs. MT cytoskeleton is a complex network with multiple intersections [8,9]. This may lead to a tug-of-war between different motors on the same organelle and frequent cargo pauses and switches to different MT track. Another compounding factor is the presence of dissimilar motors with different directional propensities on a transported cargo in the cell. This may also lead to a tug-of-war between the opposing motors and results in bi-directional motility [10–14] or extended pauses in cargo motion. My

graduate work was dedicated to finding experimental approaches to tell what was behind a cargo's lack of motility and a better understanding of tug-of-war phenomena.

Below, I introduce the main components of the relevant cytoskeletal machinery with a focus on those aspects which are most relevant to my graduate work.

1.1 Microtubules

MTs are polymers of tubulin dimers. A tubulin dimer is made up of one α-tubulin and one β-tubulin monomer, "glued" together by a Guanosine-5'-triphosphate (GTP) that does not hydrolyze [15,16]. The MT is geometrically polarized with α-tubulin orientated towards the negative end of the MT and β-tubulin orientated towards the positive end of the MT. The dimers polymerize to form a hollow MT of about 25 nm in diameter (Figure 1.1). The tubule is made of protofilaments (linear repeating unit of tubulin dimers) with 8-17 MT protofilaments stacked together [17].

The MT polymerization and de-polymerization is an important target of cellular regulation and therapeutic interventions. MT can be stabilized by MT-associated proteins, like end-binding protein 1 (EB1) which binds to MT at the positive end and prevents "catastrophe" and promotes MT polymerization [18–20]. On the other hand, members of the kinesin -13 family are known to promote MT depolymerization [21–23]. The MT dynamics is also sensitive to ambient temperature. At 4 ^{0}C, which is a relevant temperature for Chapter 4 and 5 of this dissertation, MTs are known to rapidly depolymerize [24]. The cell can utilize proteins like the stable-tubule-only-polypeptide (STOP) to counteract MT depolymerization during cold shock [25,26]. On the other hand, the heat shock protein, Hsp90, is known to protect MTs from depolymerization at high

temperature [27]. The MT stability can also be regulated via man-made chemicals. Many small molecules are known to promote or inhibit MT stability *in-vitro* and *in-vivo.* My work used paclitaxel (brand name Taxol) to stabilize MTs and to promote MT cold and heat stability.

1.2 Molecular motors

Kinesin and cytoplasmic dynein are two superfamilies of motors that transport cellular cargos on MT "highways". Kinesin motor classification includes fourteen related sub-families [28]. Twelve of these transport cargos towards the positive end of MT. The cytoplasmic dynein transported cargos are typically moved toward the negative end of MT.

1.2.1 Kinesin

The kinesin heavy chain (HC), its main polypeptide chain, consists of the motor domain, the neck-linker, and the coil-coil stalk region. The motor or head contains the catalytic region that is crucial in the conversion of adenosine triphosphate (ATP) hydrolysis to mechanical motion along the MT track [29,30].

Kinesin 1, known as conventional kinesin, is the most studied member of the kinesin family [31] . Henceforth, kinesin will be used to denote kinesin 1. The main functional unit of kinesin is a dimer made of two heavy chains. Each heavy chain contains a subdomain often called "head" which is approximately 330 amino acids long and is highly conserved in all kinesin superfamilies. It is the site of ATP binding and hydrolysis. The kinesin head can convert chemical energy in ATP, after hydrolysis of the

terminal gamma phosphate on ATP, into mechanical work for translocation on MT.

For kinesin to be processive (repeating enzymatic steps while attached) on a MT, at least one head must be bound at all times. The two motor domains of kinesin walk in "hand over hand" fashion along MT tracks. Kinesin takes a step of 8 nm in each walking cycle. The kinesin nucleotide state modulates each head's affinity to MT as kinesin walks on MT track [32,33].

The typical velocity of kinesin-1 at room temperature and standard pressure is around 600 to 700 nm/sec. A single kinesin can produce about 5-7 pN force on ATP hydrolysis [34,35]. For kinesin, there exists a nonlinear effect of an opposing load on kinesin processivity and velocity [36]. At saturating ATP concentration, force-velocity relationship of a kinesin is convex, which means that kinesin is at first insensitive to an opposing force with increasing opposing load and then the velocity rapidly declines until the stall force of about 6 pN [37]. On the other hand, processivity of kinesin declines rapidly with an increasing opposing force at low force and rate of decline reduces as it approaches stall force [36,38]. Single molecule kinesin can take approximately 100 steps and go processively for about 800 nm before falling off the MT track [39,40]; ensembles of kinesin can walk for a significantly longer distance [41,42]. The processivity of kinesin is dependent on the rate of phosphate release after ATP hydrolysis. The processivity of kinesin is longer when the rate of phosphate release is reduced [38]. I have used temperature variation to look at the enzymatic activity of kinesin. This approach is an important physical technique in the study of biological enzymes [43–45]. In the simplest case, enzymes obey Arrhenius kinetics, $rate \propto e^{\frac{-E_a}{k_b T}}$, where E_a represents the activation energy, k_b is the Boltzmann constant, and T is the temperature in Kelvin. Kinesin activity has been

studied as a function of temperature in MT gliding assays and in single molecule experiments [46–50]. In all these studies, kinesin activity was observed above 15 ^{0}C. This dissertation has extended these studies to much lower temperatures (Chapter 4).

1.2.2 Kinesin NCD

Another family of kinesin important for this dissertation is Drosophila melanogaster nonclaret disjunctional protein (NCD). It is a member of the kinesin-14 family that is important for chromosomal segregation during mitosis. Like conventional kinesin, NCD contains a dimer of heavy chains possessing enzymatic activity. In contrast to conventional kinesin, NCD has the head domain at the C-terminal end and its powerstroke is directed towards the negative end of the MT [51]. However, there is 30% probability of a powerstroke towards the positive end of MT [52]. Also unlike conventional kinesin, NCD is a nonprocessive motor, which means a single NCD head takes a single power stroke and detaches from MT. NCD lacks the neck-linker and ATP binding on the MT bound head has the effect of causing 70^0 rotation in the neck with an overall negative end directed MT motion [53]. Another important difference between conventional kinesin and NCD is that the orientation of the NCD head is rotated about 120^0 in respect to the kinesin head (Figure 1.2) [54]. Furthermore, crystal structure analysis reveals that kinesin's unbound head is positioned to bind the next binding site towards the positive MT whereas the unbound head of NCD is oriented towards the negative end of MT [54].

A N340K mutation in the neck of NCD creates an electrostatic repulsive interaction with K640 (Figure 1.3) residue within the motor domain [55]. As I stated in the previous paragraph, wild type NCD has only 30% probability of moving towards the

positive end of MT; however, the electrostatic repulsion created by N340K mutation "unhinged" the neck from the motor domain, resulting in a balanced probability of moving towards either end of the MT [55]. I make use of this bi-directional property in Chapter 5 of this dissertation, as it simplifies modeling of motors tug-of-war.

1.2.3 Cytoplasmic dynein

There are two classes of dynein: cytoplasmic and axonemal dynein [56]. In this work, I am mostly focused on cytoplasmic dynein. Cytoplasmic dynein, a protein identified in 1987 [57], is the second major class of biological motors that transports cargos in the cell. Henceforth, dynein will be used to denote cytoplasmic dynein. In contrast to kinesin, dynein walks predominantly towards the negative end of the MT [31]. Its structure is fundamentally different from kinesin; this suggests a completely disparate evolutionary track. Dynein is an ATPase that belongs to the AAA+ superfamily [58–60]. AAA+ ATPases are hexameric protein rings that undergo conformational changes on ATP hydrolysis to perform mechanical work. Examples of the mechanical work performed are ripping apart DNA and RNA duplexes, breaking macromolecular complexes, and unfolding of proteins [60–63]. Dynein contains a homodimer of two heavy chains (HCs) with each HC having an hexameric AAA+ ATPase ring (Figure 1.4) [64]. The two HCs dimerize at the N-terminal region. The ATP hydrolysis in the HC is converted into mechanical motion with translocation along the MT track.

There are other important polypeptide chains that are part of the dynein complex: a dimer of intermediate chains, a dimer of light intermediate chains, and three dimers of light chains (LC8, Roadblock, and Tctex). These chains add additional regulatory control

to dynein which may include specificity of bound cargos.

Dynein interacts with additional regulatory proteins which are not part of the permanent complex. However, work on dynein with regulatory co-factors is beyond the scope of my dissertation work and is an interesting research direction for the future.

Unlike kinesin-1, cytoplasmic dynein can take steps which are 8 nm and larger [65]. Also, unlike conventional kinesin, dynein can take lateral steps and occasionally translocate processively towards the positive end of the MT [66,67].

Temperature is an important tool in single molecule study of dynein (similar to kinesin, discussed above). Studies on how temperature affects the activity of cytoplasmic dynein are rare. Temperature study has been done on axonemal dynein [68–70]. My work in Chapter 4 helps bridge some of knowledge gaps for cytoplasmic dynein temperature dependent properties at a single molecule. This is important in order to better understand temperature dependent transport phenotype like cold block of neurons MT dependent transport [71] and how cold adapted organism might have overcome the cold transport block. While it was known that *S. cerevisiae* cytoplasmic dynein velocity is much slower (about 70 nm/sec) [66,67] than that of mammalian cytoplasmic dynein (about 1000 nanometer/sec) at room temperature [72], the study in Chapter 4 uncovers more interesting differences in their properties as a function of temperature in terms of a break in their Arrhenius kinetics. Another major difference is that *S. cerevisiae* cytoplasmic dynein can produce force between 5-7 pN [67], while mammalian cytoplasmic dynein can produce about 1-2 pN [65,72]. There is evidence that under a high opposing force greater than stall force, yeast and mammalian dynein can move processively towards the MT plus end [67,72]. The velocity of dynein decreases under increasing opposing load. Yeast dynein shows

high persistence under load while mammalian dynein is less persistent but this property can be modulated by co-factors [67,72,73].

1.3 Ensemble properties of molecular motors

More than one motor is usually involved in the transport of cellular cargos [74,75] . This raises an important scientific question on how multiple motors cooperate. One possible outcome of multiple motors interaction is longer run length. While single molecule kinesin takes about 800 nm before dissociating from MT, multiple kinesins can synergistically move for a relatively long distance [41,76]. The mean field theoretical prediction for how the number of kinesin motors transporting a cargo, N, affects the run length is approximately given by $5^{N-1}/N$ micrometers under standard assay conditions and also assuming the motors are perfectly clustered in a singler spot on the cargo [76]. Experiments have also reported a longer run length for multiple motors [41,42]. Another point to note is that the on rate used in the theory is temperature dependent, and I confirmed in Chapter 4 that by reducing the temperature, the run length is reduced. Multiple motors can also cooperatively move against greater opposing load than an individual motor [42,77].

An important area of research in the field of molecular motors is the ensemble behaviors of opposite directed motors on a cargo. Opposite directed motors are seen on all types of cargo in the cell which can lead to their bi-directional motion and near immotile "diffusive" transport [13,78]. One major hypothesis for their joint behavior is the tug-of-war model [78]. A recent study which experimentally examined the a tug-of-war between a team of yeast dyneins and a team of kinesins concluded that "*the ratio of*

dynein to kinesin dictated cargo directionality" [13]. For mammalian dynein, one expects something similar, but mammalian dynein is much weaker than kinesin (without co-factor regulation). So force balance in that case would require many dyneins to balance out each kinesin [73]; however, many dynein motors have significantly higher net persistence on the MT which then favors minus-end directed transport for force balanced ensembles. I also show in Chapter 4 that at low temperature, there is a qualitative change: a team of kinesins wins in a force balanced tug-of-war with dyneins, due to temperature dependent change in dynein kinetics.

Tug-of-war can result in a near immotile phase of the transport that is driven by opposite directed motors [13]. This near immotile phase of transport is the main focus of Chapters 2 and 5 of this dissertation. In particular, I make use of the nonprocessive bi-directional kinesin NCD N340K mutant discussed previously in section 1.2.2 as the model motor to study the question three and four. Unlike the work of Derr et al., my system was inherently fully bi-directionally balanced which allowed me to focus very specifically on the nearly immotile transport. I characterized the ensemble properties of the near immotile state as a function of temperature and showed how the tug-of-war can be distinguished from thermally activated diffusion in the cell.

Overall, my graduate work has helped to understand how molecular motors oppose each other and what is behind the long-ignored part of cargo motility: pauses and near-stationary periods. I also helped established variable temperature microscopy as a key technique for looking at the mechanistic details of cargo immobility

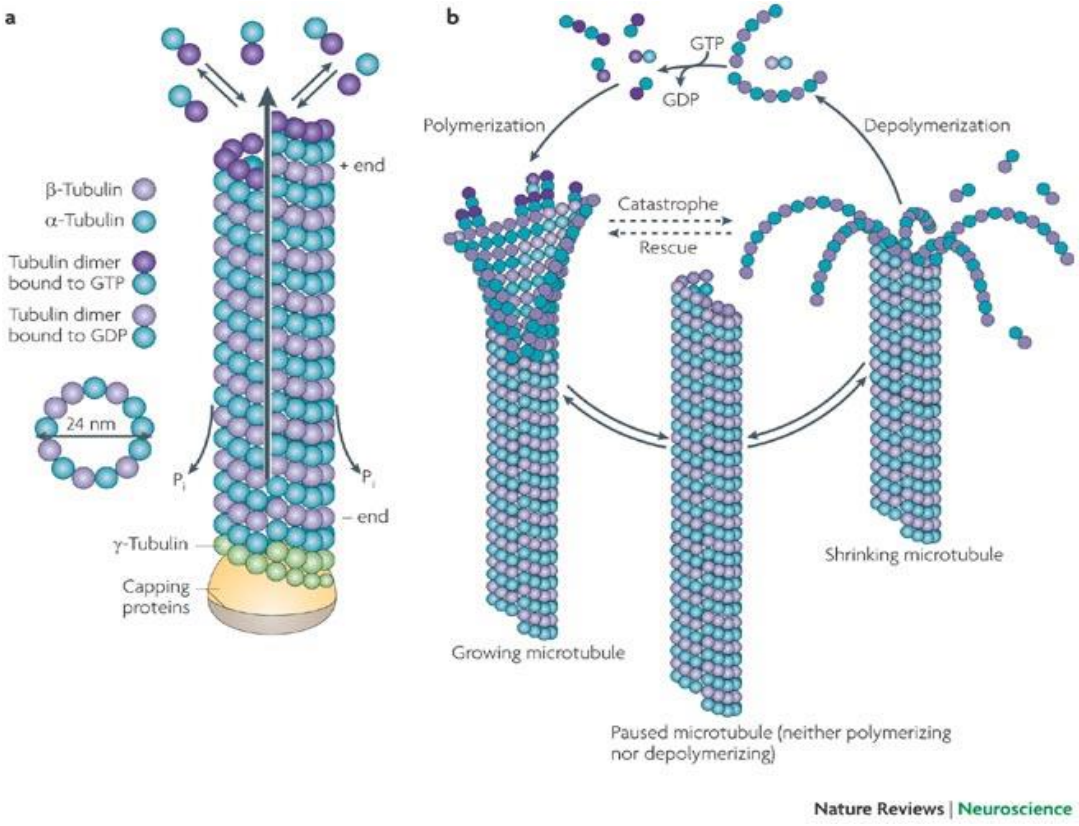

Figure 1.1 Microtubules dynamics [15]. Reprinted with permission from Nature Publishing group.

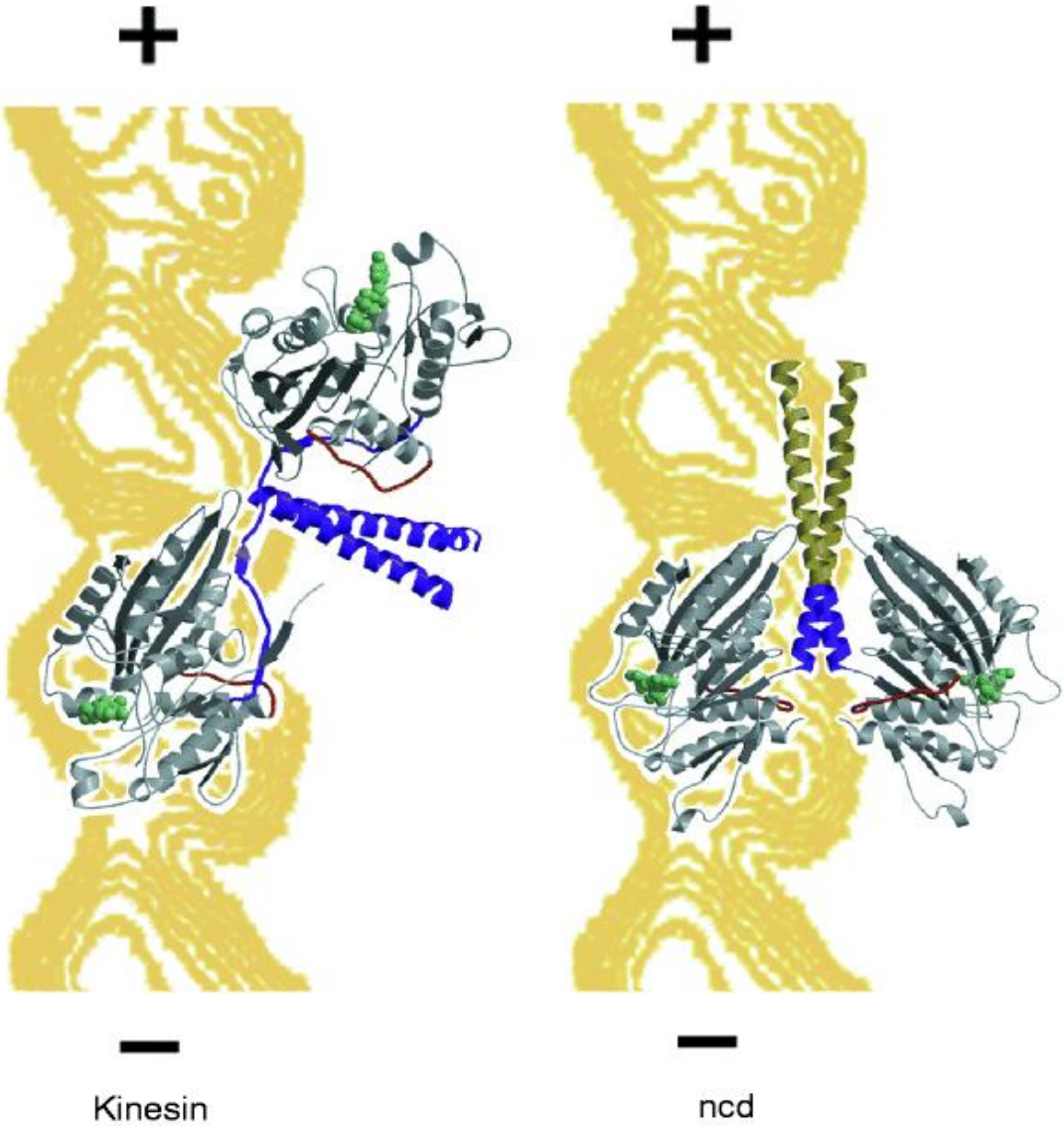

Figure 1.2 Structure of kinesin and NCD orientation on the MT [54]. Reprinted with permission from Nature Publishing group.

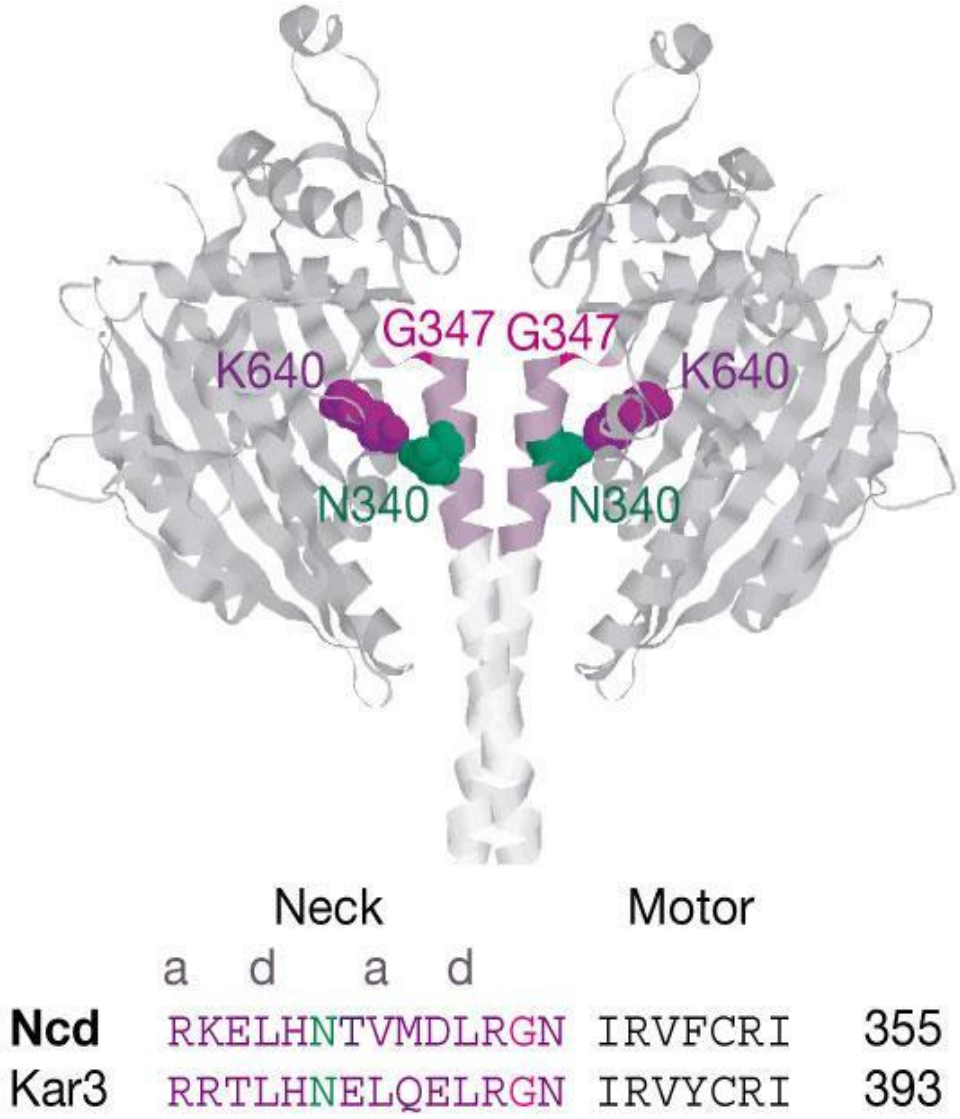

Figure 1.3. The crystal structure of NCD N340K bi-directional motor [55]. Reprinted with permission from Nature Publishing group.

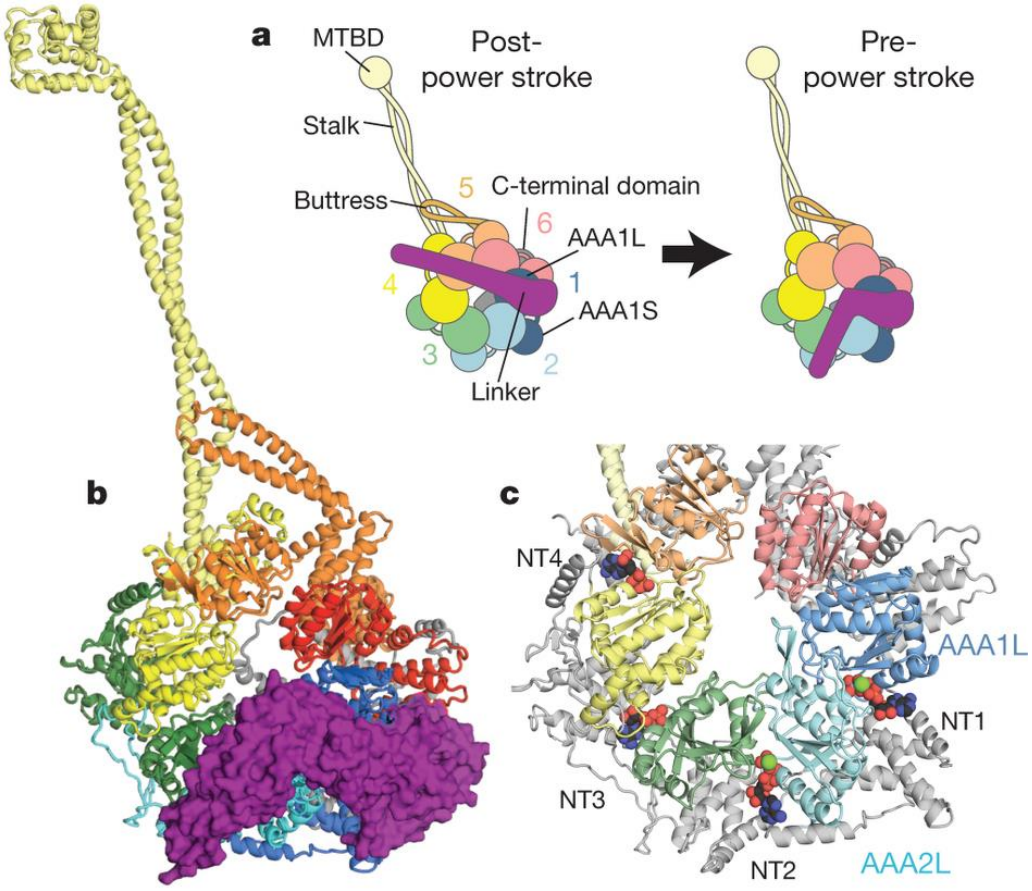

Figure 1.4 Crystal structure of dynein [64]. Reprinted with permission from Nature Publishing group.

1.4 References

1. Goodenough, U. W. & Heuser, J. E. Substructure of inner dynein arms, radial spokes, and the central pair/projection complex of cilia and flagella. *J Cell Biol* **100,** 2008–2018 (1985).

2. Schmoranzer, J. & Simon, S. M. Role of microtubules in fusion of post-Golgi vesicles to the plasma membrane. *Mol Biol Cell* **14,** 1558–1569 (2003).

3. Steinberg, G. & Fuchs, U. The role of microtubules in cellular organization and endocytosis in the plant pathogen Ustilago maydis. *J Microsc* **214,** 114–123 (2004).

4. Cash, A. D. *et al.* Microtubule reduction in Alzheimer's disease and aging is independent of tau filament formation. *Am J Pathol* **162,** 1623–1627 (2003).

5. Mochida, G. H. Molecular genetics of lissencephaly and microcephaly. *Brain Nerve* **60,** 437–444 (2008).

6. Grundke-Iqbal, I. *et al.* Abnormal phosphorylation of the microtubule-associated protein tau (tau) in Alzheimer cytoskeletal pathology. *Proc Natl Acad Sci U S A* **83,** 4913–4917 (1986).

7. Sapir, T., Elbaum, M. & Reiner, O. Reduction of microtubule catastrophe events by LIS1, platelet-activating factor acetylhydrolase subunit. *EMBO J* **16,** 6977–6984 (1997).

8. Zhang, Z., Nishimura, Y. & Kanchanawong, P. Extracting microtubule networks from superresolution single-molecule localization microscopy data. *Mol Biol Cell* **28,** 333–345 (2017).

9. Huang, B., Jones, S. A., Brandenburg, B. & Zhuang, X. Whole-cell 3D STORM reveals interactions between cellular structures with nanometer-scale resolution. *Nat Methods* **5,** 1047–1052 (2008).

10. Hancock, W. O. Bidirectional cargo transport: moving beyond tug of war. *Nat Rev Mol Cell Biol* **15,** 615–628 (2014).

11. Schuster, M., Lipowsky, R., Assmann, M.-A., Lenz, P. & Steinberg, G. Transient binding of dynein controls bidirectional long-range motility of early endosomes. *Proc Natl Acad Sci U S A* **108,** 3618–3623 (2011).

12. Müller, M. J. I., Klumpp, S. & Lipowsky, R. Tug-of-war as a cooperative mechanism for bidirectional cargo transport by molecular motors. *Proc Natl Acad Sci U S A* **105,** 4609–4614 (2008).

13. Derr, N. D. *et al.* Tug-of-war in motor protein ensembles revealed with a programmable DNA origami scaffold. *Science* **338,** 662–665 (2012).

14. Welte, M. A., Gross, S. P., Postner, M., Block, S. M. & Wieschaus, E. F. Developmental regulation of vesicle transport in Drosophila embryos: forces and kinetics. *Cell* **92,** 547–557 (1998).

15. Conde, C. & Cáceres, A. Microtubule assembly, organization and dynamics in axons and dendrites. *Nat Rev Neurosci* **10,** 319–332 (2009).

16. Feit, H., Slusarek, L. & Shelanski, M. L. Heterogeneity of tubulin subunits. *Proc Natl Acad Sci U S A* **68,** 2028–2031 (1971).

17. Fourniol, F. J. *et al.* Template-free 13-protofilament microtubule-MAP assembly visualized at 8 A resolution. *J Cell Biol* **191,** 463–470 (2010).

18. Fong, K.-W. *et al.* Microtubule plus-end tracking of end-binding protein 1 (EB1) is regulated by CDK5 regulatory subunit-associated protein 2. *J Biol Chem* **292,** 7675–7687 (2017).

19. Mimori-Kiyosue, Y., Shiina, N. & Tsukita, S. The dynamic behavior of the APC-binding protein EB1 on the distal ends of microtubules. *Curr Biol* **10,** 865–868 (2000).

20. Nakamura, M., Zhou, X. Z. & Lu, K. P. Critical role for the EB1 and APC interaction in the regulation of microtubule polymerization. *Curr Biol* **11,** 1062–1067 (2001).

21. Cross, R. A. & McAinsh, A. Prime movers: the mechanochemistry of mitotic kinesins. *Nat Rev Mol Cell Biol* **15,** 257–271 (2014).

22. Mennella, V. *et al.* Functionally distinct kinesin-13 family members cooperate to regulate microtubule dynamics during interphase. *Nat Cell Biol* **7,** 235–245 (2005).

23. Desai, A., Verma, S., Mitchison, T. J. & Walczak, C. E. Kin I kinesins are microtubule-destabilizing enzymes. *Cell* **96,** 69–78 (1999).

24. Tilney, L. G. & Porter, K. R. Studies on the microtubules in heliozoa. II. The effect of low temperature on these structures in the formation and maintenance of the axopodia. *J Cell Biol* **34,** 327–343 (1967).

25. Slaughter, T. & Black, M. M. STOP (stable-tubule-only-polypeptide) is preferentially associated with the stable domain of axonal microtubules. *J Neurocytol* **32,** 399–413 (2003).

26. Bosc, C., Andrieux, A. & Job, D. STOP proteins. *Biochemistry* **42,** 12125–12132 (2003).

27. Weis, F., Moullintraffort, L., Heichette, C., Chrétien, D. & Garnier, C. The 90-kDa heat shock protein Hsp90 protects tubulin against thermal denaturation. *J Biol Chem* **285,** 9525–9534 (2010).

28. Lawrence, C. J. *et al.* A standardized kinesin nomenclature. *J Cell Biol* **167,** 19–22 (2004).

29. Kuznetsov, S. A., Vaisberg, Y. A., Rothwell, S. W., Murphy, D. B. & Gelfand, V. I. Isolation of a 45-kDa fragment from the kinesin heavy chain with enhanced ATPase and microtubule-binding activities. *J Biol Chem* **264,** 589–595 (1989).

30. Ingold, A. L., Cohn, S. A. & Scholey, J. M. Inhibition of kinesin-driven microtubule motility by monoclonal antibodies to kinesin heavy chains. *J Cell Biol* **107,** 2657–2667 (1988).

31. Vale, R. D. The molecular motor toolbox for intracellular transport. *Cell* **112,** 467–480 (2003).

32. Yildiz, A., Tomishige, M., Vale, R. D. & Selvin, P. R. Kinesin walks hand-over-hand. *Science* **303,** 676–678 (2004).

33. Nitta, R., Kikkawa, M., Okada, Y. & Hirokawa, N. KIF1A alternately uses two loops to bind microtubules. *Science* **305,** 678–683 (2004).

34. Coppin, C. M., Finer, J. T., Spudich, J. A. & Vale, R. D. Measurement of the isometric force exerted by a single kinesin molecule. *Biophys J* **68,** 242S–244S (1995).

35. Svoboda, K. & Block, S. M. Force and velocity measured for single kinesin molecules. *Cell* **77,** 773–784 (1994).

36. Schnitzer, M. J., Visscher, K. & Block, S. M. Force production by single kinesin motors. *Nat Cell Biol* **2,** 718–723 (2000).

37. Visscher, K., Schnitzer, M. J. & Block, S. M. Single kinesin molecules studied with a molecular force clamp. *Nature* **400,** 184–189 (1999).

38. Milic, B., Andreasson, J. O. L., Hancock, W. O. & Block, S. M. Kinesin processivity is gated by phosphate release. *Proc Natl Acad Sci U S A* **111,** 14136–14140 (2014).

39. Hackney, D. D. Highly processive microtubule-stimulated ATP hydrolysis by dimeric kinesin head domains. *Nature* **377,** 448–450 (1995).

40. Block, S. M., Goldstein, L. S. & Schnapp, B. J. Bead movement by single kinesin molecules studied with optical tweezers. *Nature* **348,** 348–352 (1990).

41. Gross, S. P., Vershinin, M. & Shubeita, G. T. Cargo transport: two motors are sometimes better than one. *Curr Biol* **17,** R478–86 (2007).

42. Vershinin, M., Carter, B. C., Razafsky, D. S., King, S. J. & Gross, S. P. Multiple-motor based transport and its regulation by Tau. *Proc Natl Acad Sci U S A* **104,** 87–92 (2007).

43. Boon, M. A., Janssen, A. E. M. & Riet, K. V. Effect of temperature and enzyme origin on the enzymatic synthesis of oligosaccharides. *Enzyme and Microbial Technology* **26**, 2–4, 271-281 (2000).

44. Houslay, M. D. & Palmer, R. W. Changes in the form of Arrhenius plots of the activity of glucagon-stimulated adenylate cyclase and other hamster liver plasma-membrane enzymes occurring on hibernation. *Biochem J* **174,** 909–919 (1978).

45. Fink, A. L. & Cartwright, S. J. Cryoenzymology. *CRC Crit Rev Biochem* **11,** 145–207 (1981).

46. Kawaguchi, K. & Ishiwata, S. Temperature dependence of force, velocity, and processivity of single kinesin molecules. *Biochem Biophys Res Commun* **272,** 895–899 (2000).

47. Kawaguchi, K. & Ishiwata, S. Thermal activation of single kinesin molecules with temperature pulse microscopy. *Cell Motil Cytoskeleton* **49,** 41–47 (2001).

48. Nara, I. & Ishiwata, S. Processivity of kinesin motility is enhanced on increasing temperature. *Biophysics (Nagoya-shi, Japan)* **2,** 13–21 (2006).

49. Böhm, K. J., Stracke, R., Baum, M., Zieren, M. & Unger, E. Effect of temperature on kinesin-driven microtubule gliding and kinesin ATPase activity. *FEBS Lett* **466,** 59–62 (2000).

50. Mazumdar, M. & Cross, R. A. Engineering a lever into the kinesin neck. *J Biol Chem* **273,** 29352–29359 (1998).

51. Walker, R. A., Salmon, E. D. & Endow, S. A. The Drosophila claret segregation protein is a minus-end directed motor molecule. *Nature* **347,** 780–782 (1990).

52. Butterfield, A. E., Stewart, R. J., Schmidt, C. F. & Skliar, M. Bidirectional power stroke by ncd kinesin. *Biophys J* **99,** 3905–3915 (2010).

53. Endres, N. F., Yoshioka, C., Milligan, R. A. & Vale, R. D. A lever-arm rotation drives motility of the minus-end-directed kinesin Ncd. *Nature* **439,** 875–878 (2006).

54. Sablin, E. P. *et al.* Direction determination in the minus-end-directed kinesin motor ncd. *Nature* **395,** 813–816 (1998).

55. Endow, S. A. & Higuchi, H. A mutant of the motor protein kinesin that moves in both directions on microtubules. *Nature* **406,** 913–916 (2000).

56. Koonce, M. P., Grissom, P. M. & McIntosh, J. R. Dynein from Dictyostelium: primary structure comparisons between a cytoplasmic motor enzyme and flagellar dynein. *J Cell Biol* **119,** 1597–1604 (1992).

57. Paschal, B. M., Shpetner, H. S. & Vallee, R. B. MAP 1C is a microtubule-activated ATPase which translocates microtubules in vitro and has dynein-like properties. *J Cell Biol* **105,** 1273–1282 (1987).

58. King, S. M. Integrated control of axonemal dynein AAA(+) motors. *J Struct Biol* **179,** 222–228 (2012).

59. Firestone, A. J. *et al.* Small-molecule inhibitors of the AAA+ ATPase motor cytoplasmic dynein. *Nature* **484,** 125–129 (2012).

60. Neuwald, A. F., Aravind, L., Spouge, J. L. & Koonin, E. V. AAA+: A class of chaperone-like ATPases associated with the assembly, operation, and disassembly of protein complexes. *Genome Res* **9,** 27–43 (1999).

61. Ogura, T. & Wilkinson, A. J. AAA+ superfamily ATPases: common structure--diverse function. *Genes Cells* **6,** 575–597 (2001).

62. Davey, M. J., Jeruzalmi, D., Kuriyan, J. & O'Donnell, M. Motors and switches: AAA+ machines within the replisome. *Nat Rev Mol Cell Biol* **3,** 826–835 (2002).

63. Singleton, M. R., Dillingham, M. S. & Wigley, D. B. Structure and mechanism of helicases and nucleic acid translocases. *Annu Rev Biochem* **76,** 23–50 (2007).

64. Schmidt, H., Zalyte, R., Urnavicius, L. & Carter, A. P. Structure of human cytoplasmic dynein-2 primed for its power stroke. *Nature* **518,** 435–438 (2015).

65. Mallik, R., Carter, B. C., Lex, S. A., King, S. J. & Gross, S. P. Cytoplasmic dynein functions as a gear in response to load. *Nature* **427,** 649–652 (2004).

66. Reck-Peterson, S. L. *et al.* Single-molecule analysis of dynein processivity and stepping behavior. *Cell* **126,** 335–348 (2006).

67. Gennerich, A., Carter, A. P., Reck-Peterson, S. L. & Vale, R. D. Force-induced bidirectional stepping of cytoplasmic dynein. *Cell* **131,** 952–965 (2007).

68. Shimizu, T. The Alkaline Adenosine Triphosphatase Activity of 30S Dynein after Modification of the SH Groups. *The Journal of Biochemistry* **86**, 4, 1139-1145 (1979).

69. Hoshino, M. Interactions of Tetrahymena dynein with microtubule protein. Tubulin-induced stimulation of dynein ATPase activity. *Biochimica et Biophysica Acta (BBA) - Bioenergetics* **462,** 49–62 (1977).

70. Zhang, K. *et al.* Single-molecule imaging of NGF axonal transport in microfluidic devices. *Lab Chip* **10,** 2566–2573 (2010).

71. Cancalon, P. Influence of temperature on various mechanisms associated with neuronal growth and nerve regeneration. *Prog Neurobiol* **25**, 27-92 (1985).

72. McKenney, R. J., Vershinin, M., Kunwar, A., Vallee, R. B. & Gross, S. P. LIS1 and NudE induce a persistent dynein force-producing state. *Cell* **141,** 304–314 (2010).

73. Rai, A. K., Rai, A., Ramaiya, A. J., Jha, R. & Mallik, R. Molecular adaptations allow dynein to generate large collective forces inside cells. *Cell* **152,** 172–182 (2013).

74. Ashkin, A., Schütze, K., Dziedzic, J. M., Euteneuer, U. & Schliwa, M. Force generation of organelle transport measured in vivo by an infrared laser trap. *Nature* **348,** 346–348 (1990).

75. Shubeita, G. T. *et al.* Consequences of motor copy number on the intracellular transport of kinesin-1-driven lipid droplets. *Cell* **135,** 1098–1107 (2008).

76. Klumpp, S. & Lipowsky, R. Cooperative cargo transport by several molecular motors. *Proc Natl Acad Sci U S A* **102,** 17284–17289 (2005).

77. Mallik, R., Petrov, D., Lex, S. A., King, S. J. & Gross, S. P. Building complexity: an in vitro study of cytoplasmic dynein with in vivo implications. *Curr Biol* **15,** 2075–2085 (2005).

78. Soppina, V., Rai, A. K., Ramaiya, A. J., Barak, P. & Mallik, R. Tug-of-war between dissimilar teams of microtubule motors regulates transport and fission of endosomes. *Proc Natl Acad Sci U S A* **106,** 19381–19386 (2009).

CHAPTER 2

CARGO TRANSPORT AT MICROTUBULE CROSSINGS: EVIDENCE FOR PROLONGED TUG-OF-WAR BETWEEN KINESIN MOTORS

Reprinted with permission from Biophysical Journal

Osunbayo, O., Butterfield, J., Bergman, J., Mershon, Rodionov, V., and Vershinin, M. (2015). Cargo transport at microtubule crossings: evidence for prolonged tug-of-war between kinesin motors. Biophys J *108*, 1480–1483.

1480 Biophysical Journal Volume 108 March 2015 1480–1483

Article

Cargo Transport at Microtubule Crossings: Evidence for Prolonged Tug-of-War between Kinesin Motors

Olaolu Osunbayo,[1] Jacqualine Butterfield,[1] Jared Bergman,[1] Leslie Mershon,[1] Vladimir Rodionov,[3] and Michael Vershinin[1,2,*]

[1]Department of Physics and Astronomy and [2]Center for Cell and Genome Science, University of Utah, Salt Lake City, Utah; and [3]Department of Cell Biology, University of Connecticut, Farmington, Connecticut

ABSTRACT Intracellular transport of cargos along microtubules is often complicated by the topology of the underlying filament network. The fundamental building blocks for this complex arrangement are filament intersections. The navigation of cargos across microtubule intersections remains poorly understood. Here, we demonstrate that kinesin-driven cargos are engaged in a tug-of-war at microtubule intersections. Tug-of-war events result in long pauses that can last from a few seconds to several minutes. We demonstrate that the extent of the tug-of-war and the duration of pauses change with the number of motors on the cargo and can be regulated by ionic strength. We also show that dwell times at intersections depend on the angle between crossing microtubules. Our data suggest that local microtubule geometry can regulate microtubule-based transport.

INTRODUCTION

Cargo transport along microtubules (MTs) is a logistics technology that is essential for the function and survival of eukaryotic cells. Many key aspects of MT-based logistics in cells are only now coming into focus. There is growing interest in how cargos driven by multiple motors navigate MT intersections (1–3). Such crossings are a common feature of the cytoskeleton and can potentially regulate intracellular logistics in an entirely different fashion—via network topology, as opposed to environmental or chemical regulation. In addition, MT intersections are also likely to be the loci of local chemical regulation in cells (1,4). However, relatively little is known about the processes involved in cargo travel across MT-MT junctions.

To gain insight into the behavior of organelles at MT intersections in vivo, we examined transport of melanosomes to the cell periphery (pigment dispersion) in *Xenopus* melanophores. At early stages of pigment dispersion, melanosomes move to the plus-ends of cytoplasmic MTs driven predominantly by the kinesin-2 motors (5). Time sequences of images of melanophores with fluorescently labeled MTs (6,7) showed that melanosomes often had a reduced velocity of movement or completely stopped at MT intersections (Fig. 1 *A*; Movie S1 in the Supporting Material). Furthermore, MTs often buckled when melanosomes moving along them attached to other MTs that crossed their path (Fig. 1 *A*; Movie S1). This remarkable behavior of MTs was consistent with the application of force by cargo-bound kinesin motors simultaneously interacting with adjacent MTs.

However, other interpretations were also possible because additional motors (cytoplasmic dynein and myosin V) were also bound to melanosomes (8). Although these motors are largely inactive during pigment dispersion (8), in principle, they could generate force for MT buckling. Therefore, to examine the behavior at MT intersections of cargoes transported by kinesin motors alone, we employed a purified in vitro system. We show that cargos driven by many kinesin motors can spend extensive amounts of time at MT intersections, that such events are likely associated with a tug-of-war between multiple kinesin motors on the same cargo, and that MT bending is common if the filament deformations are not otherwise restricted (e.g., by bonds to a substrate such as a glass slide).

MATERIALS AND METHODS

Data acquisition in *Xenopus* melanophores

Xenopus melanophores were cultured in 70% L15 medium supplemented with antibiotics, 10% fetal bovine serum, and 5 mg/ml of insulin at 27°C (7). To induce pigment dispersion, cells were treated with melanocyte-stimulating hormone (10^{-8} M).

For fluorescence labeling of MTs, cells were pressure injected with Cy3-labeled bovine brain tubulin (6). Injected cells were incubated for at least 1 h at 27°C to allow for the incorporation of labeled tubulin subunits into MTs.

Fluorescence images of melanophores were acquired using a Nikon Eclipse Ti (Nikon Instrucments, Melville, NY) inverted microscope equipped with a Plan apochromat ×100 1.4 NA objective lens, and an Andor iXon EM-CCD sensor (Andor Technology USA, South Windsor, CT) driven by Metamorph image acquisition and analysis software (Molecular Devices, Sunnyvale, CA). To reduce photobleaching and photodamage,

Submitted August 6, 2014, and accepted for publication February 20, 2015.

*Correspondence: vershinin@physics.utah.edu

Editor: Ram Dixit.

0006-3495/15/03/1480/4 $2.00

http://dx.doi.org/10.1016/j.bpj.2015.02.016

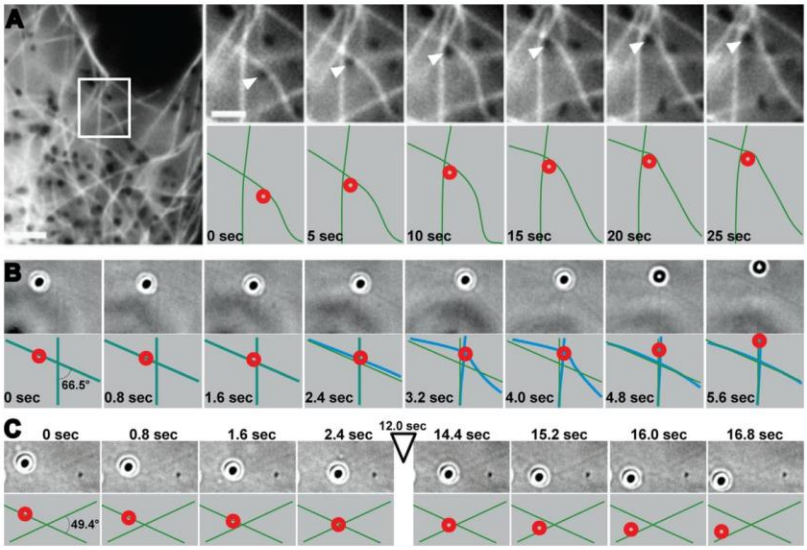

FIGURE 1 Examples of cargo dynamics at MT intersections in vivo and in vitro. (*A*) A melanosome moving along a MT in a melanophore in vivo encounters another MT that crosses its movement path. Left panel: low-magnification fluorescence image of the melanophore periphery. Right panel, top row: successive high-magnification images of the boxed images are shown in the left panel; bottom row: schematic representation of the position of the melanosome (*red circle*) and MTs (*green lines*) in the images shown in the top row. Numbers indicate time in seconds; magnification bars are 10 μm (*left panel*) and 5 μm (*right panel*). A collision of the melanosome with the crossing MT blocks its movement and leads to deformation of both crossing MTs. (*B* and *C*) Examples of cargo dynamics at MT crossings in vitro: an MT deformation event (*B*) and a very long dwell event (*C*). Numbers indicate time in seconds. Top rows: still frames of beads and MTs. Bottom rows: schematic representations of the positions of beads (*red*) and MTs (*green*) in the images shown in the top row (frame timing indicated). Blue lines show deformed geometries; fields of view: 8.5 $\times$ 4.3 μm (*B*) and 6.0 $\times$ 9.4 μm (*C*).

cells were treated with the oxygen-depleting agent Oxyrase before image acquisition.

Data acquisition in vitro

KIF5A KHC dimers were expressed in an *E. coli* system as previously described (9). Porcine tubulin was acquired from Cytoskeleton (Denver, CO) and MTs were reconstituted according to the manufacturer's protocol. Buffers and slides were prepared as previously described (1). The assay buffer was PMEE (35 mM Pipes, 5 mM $MgCl_2$, 1 mM EGTA, 0.5 mM EDTA), pH 7.2. Briefly, the flow cells were cleaned with a KOH wash, incubated with poly-L-lysine solution, and attached to a glass slide with double-sided tape. The flow chambers were assembled in a cross-flow geometry as previously described (1). Taxol-stabilized MTs were first diluted in flow buffer (assay buffer + 20 μM taxol + 1 mM GTP) and then injected into the flow cells, with a 15-min incubation after each orthogonal-direction injection. The unattached MTs were then washed away and the surface was blocked with buffer containing 20 mg/mL casein (Sigma-Aldrich, St. Louis, MO).

Carboxylated polystyrene beads (Ø1 μm or Ø3 μm; Polysciences, Philadelphia, PA) were incubated at room temperature with different concentrations of kinesin KIF5A for 15 min in the presence of dithiothreitol (2mM) and saturating ATP (2 mM ATP), and then immediately injected into the flow cells.

To achieve equivalent binding fractions in Ø1 μm and Ø3 μm bead assays, the motor concentration was increased 27-fold for the latter case. The scaling factor differs from the expected 9-fold increase in bead surface area. However, Polysciences does not produce beads with titrated concentration of carboxylic groups per bead. A similar manufacturing process used by Bangs Laboratories is known to have a wide variation of carboxyl group concentrations between bead lots (e.g., 17–207 μM carboxyl groups per 1 g of beads for Ø1 μm beads). Therefore, our ratio is well within the expected range. Due to the large variability between bead lots, we chose to use the binding fraction measurements as a direct estimate of motor activity on the beads.

Measurements were performed as previously described (10). Briefly, beads and MTs were viewed using a Nikon Eclipse Ti microscope equipped with a high-magnification, high-NA objective (Nikon Plan Apo VC 100$\times$ oil, 1.40 NA). A high-resolution camera (iXon+ DU897; Andor Technology USA, South Windsor, CT) and Nikon NIS elements AR software (Nikon Instruments, Melville, NY) were used to record experiments. Custom-built image-processing, speed-tracking, and angle-measuring software written in MATLAB (The MathWorks, Natick, MA) was used. Further analysis and curve fitting were performed with OriginPro software (OriginLab, Northampton, MA).

Most MT-MT crossing events were associated with low cargo velocities so that the beginning and the end of such dwell events could be identified from tracks of bead position for all frames. A dwell time of zero was recorded for events with no drop in cargo velocity during video records in which a cargo and both MTs visually overlapped.

Statistical tests were performed using the Wilcoxon-Mann-Whitney test. Student's *t*-test was not used, because most of the distributions tested were long tailed (not Gaussian).

RESULTS AND DISCUSSION

We used polystyrene beads with preadsorbed, recombinant, full-length dimers of heavy chains (KHC) of conventional kinesin KIF5A as model synthetic cargos. To facilitate interaction of motors with MTs, we used high surface densities of kinesin motors (Fig. S1) that significantly exceeded the densities used in previous studies (1,2). To examine MT-MT intersections for a variety of angles, we employed the crossed-flow geometry (1,2) and admitted MTs into flow cells at low flow to diminish the flow alignment of MTs on the coverslips. In our experiments, MTs were attached to coverslips via poly-L-lysine chains and the attachment was often very loose, with long MT segments free from surface constraints. This experimental setup allowed us to generate MT-MT junctions with a variety of angles (Fig. 1, *B* and *C*; Movies S2 and S3).

We found that, in agreement with in vivo data, cargo activity often deformed MTs at intersections, typically in a reversible fashion such that MTs returned to their original configuration upon cargo passage (Fig. 1, *B* and *C*). Cargos driven by high numbers of kinesin-1 motors (baseline concentration, marked by * in Fig. S1) dwelled for extended periods of time at MT intersections: 55.0% of events (60 of 109) lasted for more than 1 s. Outlier dwells as long as 60 s were observed (Fig. 2).

To examine whether the effect was due to a motor tug-of-war, we increased the effective motor number on the cargos using two strategies: 1) we incubated beads with a 10× higher motor concentration (** in Fig. S1), and 2) we used 10× diluted motility buffer (since kinesin's affinity for MTs depends on the overall salt concentration). In both cases, we observed an increase in the percentage of dwells longer than 1 s: 68.2% (58 of 85) for the 10× motor assay and 61.8% (63 of 102) for the low-ionic-strength assay. The mean dwell times increased for all angle ranges: the increases were significant for the 0–30° and 30–60° angle ranges, but marginally insignificant for the 60–90° range. In addition, nearly half of the dwells that were longer than 5 s in the 10× KIF5A and 0.1 salt assays were associated with MT bending (16 of 34 and 11 of 27, respectively). Our results are consistent with the hypothesis that motors at MT intersections undergo tug-of-war events, and that such competition can lead to exceedingly long cargo dwell times. The lack of or marginal change in dwell times across our assays for nearly normal intersections is consistent with theoretical prediction (11).

Most of the exceedingly long dwell times occurred for very acute junction angles. For example, in our baseline assay, all pauses longer than 50 s occurred for angles below 30°. Conversely, cargo dwell times for angles above 70° were all below 1 s. The dwell times for the crossings in the 60–90° range were significantly lower than those for the 0–30° range ($p <$ 1e-5 for all assays).

For long pauses, the tracking records were often long enough for us to examine the dynamics at the intersection (Fig. 3). Cargo velocities during the time the cargos were associated with two MTs were variable. In some cases, noise made identification of segments of constant velocity ambiguous. However, even selecting only the clear segments of constant velocity still showed a dramatic slowdown, on average <300 nm/s in all assays discussed above (Fig. 3 *B*). Cargos were not slowing down due to high number of motors working together (12) or motor crowding (10,11), since motor velocities appeared healthy away from MT crossings (Fig. S2).

The fact that cargos were not precisely stationary suggests that the motors were not blocked by an obstacle on

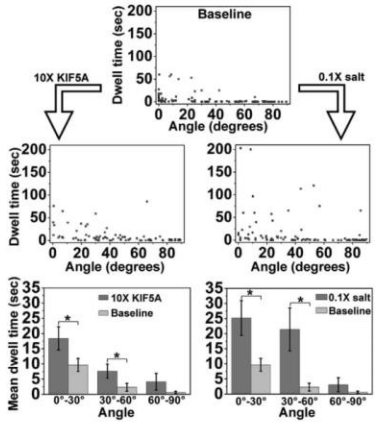

FIGURE 2 Effect of motor number on dwell times at MT intersections as a function of angles between undeformed MTs. Top: baseline assay (n = 109). Middle: assays with 10× motor number (n = 83) or low ionic strength (n = 95), as indicated by angled arrows. Bottom: comparison of mean dwell times in 30°-wide bins for top and middle panel data (error bars: mean ± SE). Significant increases are indicated by asterisks (left to right: p = 0.0496, 0.0088, 0.0044, 1.2e-4).

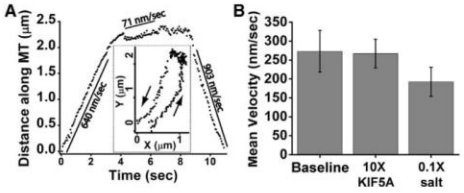

FIGURE 3 Long dwells consist of slow cargo motions. (*A*) Example of motion along nearly antiparallel MTs, projected along the MT direction. Healthy kinesin-1 motility is interrupted by a region of slow motion. Solid lines highlight select regions of nearly constant velocity (values shown). Inset: the actual track is shown. Arrows show the direction of cargo motion. (*B*) Bar graph of average velocities observed during dwells for assays in Fig. 2 as indicated.

MTs, so a tug-of-war is confirmed as the likeliest scenario. The velocities were low enough that they could not have arisen due to a plausible sideways load on the motors (15). Instead, the kinesin force-velocity relationship (15) suggests that individual motors had to experience at least 3.5 pN of backward load to match the observed slowdown. The actual slowdown was likely greater and the load per motor was even closer to stall because we excluded segments whose velocity was too low to extract from noise.

Why would a tug-of-war result in long dwell times? It is possible that geometry plays a direct role: a bead is in position to experience a tug-of-war so long as it overlaps both MTs (or is within motor length of both), so a nearly antiparallel layout of MTs could lead to longer dwell events. Our data do not rule this out, but its contribution is likely small. First, dwell events at an antiparallel MT geometry were often spatially localized (Fig. 3 *A*), suggesting that geometry is not the limiting factor for a tug-of-war. Furthermore, one can preferentially increase the bead-MT overlap for MT intersection angles close to 90° by using larger beads (the overlap for nearly aligned MTs is not limited by bead size). Experiments with 3 μm beads showed dwell times comparable to those observed with 1 μm beads (Fig. S3).

We propose that a more prominent contribution to long dwells may be made by extended kinesin-MT attachment times under high load (see Figs. S4 and S5 and Text S1 for further discussion) and reduced kinesin-MT attachment times under sideways load (12,13). The former could produce long dwells, while the latter could restrict long dwells to events with nearly antiparallel geometries. Further modeling in the future is needed to attain a quantitative description of the switching process.

CONCLUSIONS

In this study, we demonstrate that kinesin motors bound to cargoes can engage in an extended tug-of-war at MT intersections. Our data highlight the importance of factors that control the geometry of MT networks, and local regulators of the motor-MT affinity for MT-based transport. We also find that intersecting MTs that are not firmly fixed in space can be bent by passing cargos. Therefore, we propose that future efforts aimed at modeling cargo traversals of MT-MT crossings need to take into account MT deformations and the elastic properties of MTs rather than strictly focus on a fixed filament geometry.

Our finding that an increased number of motors on cargos leads to longer dwell events is consistent with the proposal that local agents that reduce motor-MT affinity can reduce or alleviate extended cargo pausing (1). Finally, our study also raises the question of how long-distance kinesin-driven transport occurs when antiparallel MT arrangements are present in cells (14).

SUPPORTING MATERIAL

Supporting Results and Discussion, five figures, and three movies are available at http://www.biophysj.org/biophysj/supplemental/S0006-3495(15)00181-2.

REFERENCES

1. Vershinin, M., B. C. Carter, …, S. P. Gross. 2007. Multiple-motor based transport and its regulation by Tau. *Proc. Natl. Acad. Sci. USA.* 104: 87–92.
2. Ross, J. L., H. Shuman, …, Y. E. Goldman. 2008. Kinesin and dynein-dynactin at intersecting microtubules: motor density affects dynein function. *Biophys. J.* 94:3115–3125.
3. Bálint, Š., I. Verdeny Vilanova, …, M. Lakadamyali. 2013. Correlative live-cell and superresolution microscopy reveals cargo transport dynamics at microtubule intersections. *Proc. Natl. Acad. Sci. USA.* 110:3375–3380.
4. Kosaka, S., H. Takuma, …, H. Mori. 2004. The distributions of tau short and long isoforms fused with EGFP in cultured cells. *Osaka City Med. J.* 50:19–27.
5. Tuma, M. C., A. Zill, …, V. Gelfand. 1998. Heterotrimeric kinesin II is the microtubule motor protein responsible for pigment dispersion in Xenopus melanophores. *J. Cell Biol.* 143:1547–1558.
6. Semenova, I., and V. Rodionov. 2007. Fluorescence microscopy of microtubules in cultured cells. *Methods Mol. Med.* 137:93–102.
7. Ikeda, K., I. Semenova, …, V. Rodionov. 2010. Melanophores for microtubule dynamics and motility assays. *Methods Cell Biol.* 97: 401–414.
8. Nascimento, A. A., J. T. Roland, and V. I. Gelfand. 2003. Pigment cells: a model for the study of organelle transport. *Annu. Rev. Cell Dev. Biol.* 19:469–491.
9. Smith, T. E., W. Hong, …, M. Vershinin. 2013. Single-molecule inhibition of human kinesin by adociasulfate-13 and -14 from the sponge Cladocroce aculeata. *Proc. Natl. Acad. Sci. USA.* 110:18880–18885.
10. Butterfield, J., W. Hong, L. Mershon, and M. Vershinin. 2013. Construction of a high resolution microscope with conventional and holographic optical trapping capabilities. *J. Vis. Exp.* http://dx.doi.org/10.3791/50481.
11. Erickson, R. P., S. P. Gross, and C. C. Yu. 2013. Filament-filament switching can be regulated by separation between filaments together with cargo motor number. *PLoS ONE.* 8:e54298.
12. Bieling, P., I. A. Telley, …, T. Surrey. 2008. Processive kinesins require loose mechanical coupling for efficient collective motility. *EMBO Rep.* 9:1121–1127.
13. Leduc, C., K. Padberg-Gehle, …, J. Howard. 2012. Molecular crowding creates traffic jams of kinesin motors on microtubules. *Proc. Natl. Acad. Sci. USA.* 109:6100–6105.
14. Conway, L., D. Wood, …, J. L. Ross. 2012. Motor transport of self-assembled cargos in crowded environments. *Proc. Natl. Acad. Sci. USA.* 109:20814–20819.
15. Block, S. M., C. L. Asbury, …, M. J. Lang. 2003. Probing the kinesin reaction cycle with a 2D optical force clamp. *Proc. Natl. Acad. Sci. USA.* 100:2351–2356.

Supplemental Material

Full title:

Cargo transport across microtubule intersections: evidence for prolonged tug of war between kinesin motors.

Running head:

Cargo transport across MT intersections

Olaolu Osunbayo*, Jacqualine Butterfield*, Jared Bergman*, Leslie Mershon*, Vladimir Rodionov[#], Michael Vershinin*[†]

* Department of Physics and Astronomy, University of Utah, Salt Lake City, Utah, 84112, USA

[†] Center for Cell and Genome Science, University of Utah, Salt Lake City, Utah, 84112, USA

[#] Department of Cell Biology, University of Connecticut, Farmington, Connecticut, 06030, USA

Fig. S1 Kinesin concentration reference curve. The binding fraction measurements for kinesin bead assays (∅1 μm) were well fit by a single motor curve (red). Motor incubation concentrations used in this study are shown by arrows and stars (* : 0.064 nM ; ** : 0.64 nM). Nominal motor to bead molar ratios were 850:1 and 8500:1 respectively. For comparison with previously published results, note that here kinesin concentration is shown on logarithmic scale.

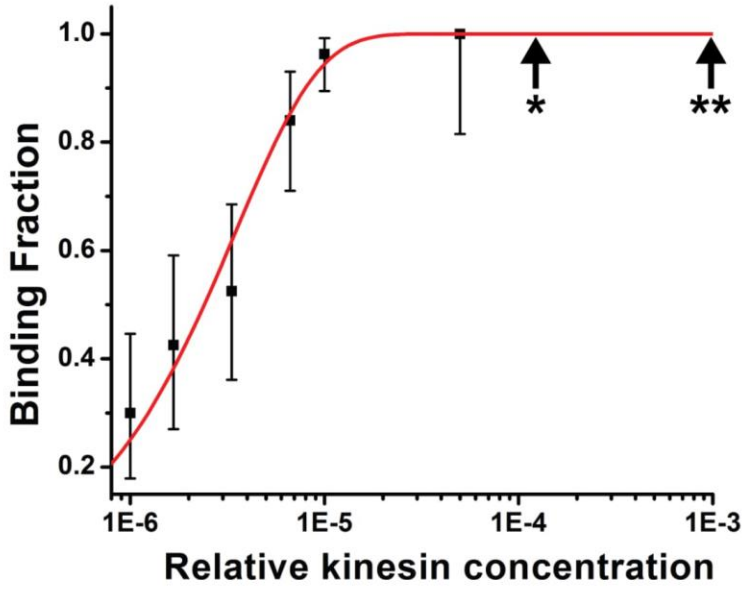

Fig. S2 Cargo velocity when moving along stand-alone MTs. Motor velocities were broadly peaked around 746 ± 51 nm/sec (mean ± SE).

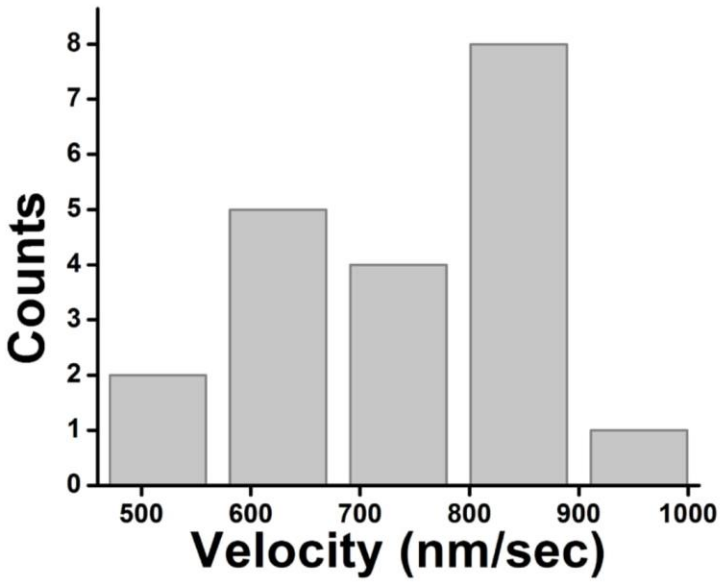

Fig. S3 The angular dependence of dwell times for different size beads. Bead assays for ∅1 μm and ∅3 μm beads were conducted to establish binding fraction curves and in each case an equivalent assay (** in Fig. S1) was used to quantify cargo dwell times ar MT intersections. High motor concentration was chosen to maximize the probability of motor engagement on both MTs during each crossing event and thereby to minimize the probability of undercounting the more localized tug-of-war events. The observed differences were not significant. We observed no evidence that higher bead-MT overlap at intersections (as would be the case for larger beads) leads to a more uniform distribution of dwell times.

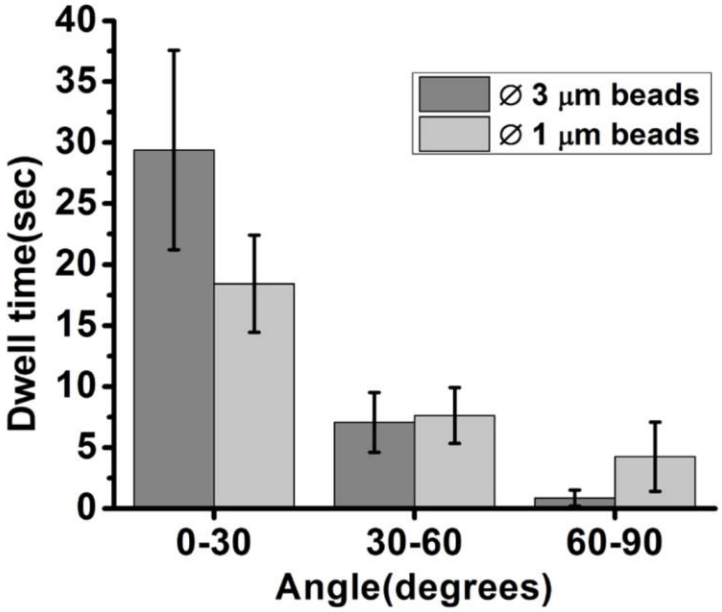

Fig. S4 The effect of MT-MT orientation on dwell times. Dwell times for cargos at intersections for baseline (left, n=59), high motor concentration (middle, n=44) and low salt concentration (right, n=40) assays are shown as a function of MT-MT angle. 180° angle corresponds to parallel MTs with identical polarity.

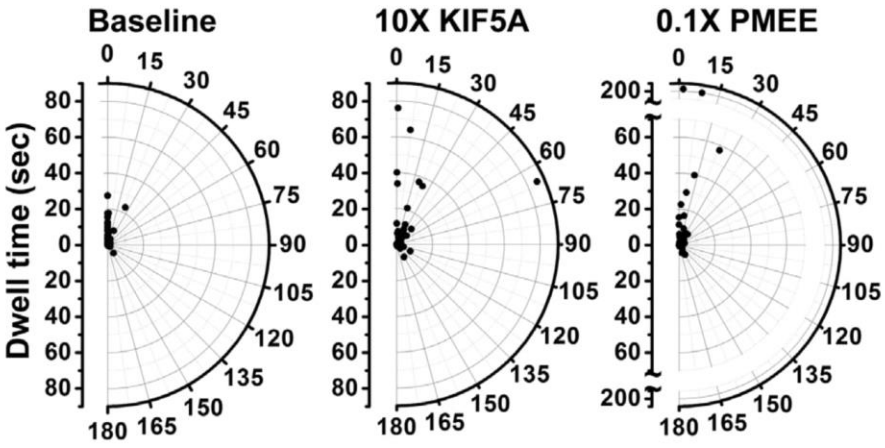

Fig. S5 Histograms of dwell times for intersections of MTs with known polarity. Dwell time distributions lower than 30 s are well fit by exponential decays (red lines) for the baseline, low salt, and high motor concentration assays. See Fig. S4 for angular distribution of these dwell times. Decays times extracted from fits are 3.2±0.4, 4.0±0.8, 5.3±0.4 s (left, middle, right panels respectively). Note that even though an exponential fit is a convenient way to characterize the decay of dwell time distributions, individual motor detachment times are likely to be less than 1 sec – far smaller than the bin size. Therefore it is not possible to tell whether the actual distribution is exponential or e.g. a higher order gamma distribution. We therefore cannot speculate whether single or multiple motor detachment events are associated with termination of dwells.

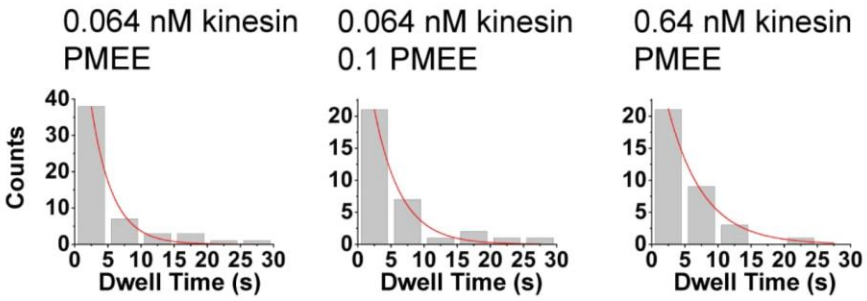

Supplemental Text S1

If cargo dwells at MT crossings are indeed due to opposing action of kinesin motors then one would expect this to occur preferentially for those acute intersection angles where MT polarity was opposite. We therefore attempted to segregate the latter acute angle crossings based on whether MT minus-plus directions were roughly aligned or roughly anti-aligned. We focused on a subset of MT crossings for which cargos switched filaments. In such cases, MT polarity could be inferred for both crossing filaments from the direction of cargo motion, and so the angles between positive directions of MT axes could be quantified.

The crossing angles for known MT polarity cases thus ranged between 0° and 180° rather than 0° to 90° for polarity-agnostic case (Fig. S4). The dwell times for MT crossing angles between 0° and 60° were significantly longer than for higher angles ($p = 0.039$ for baseline assay, $p<0.01$ for high motor and low salt assays). We further examined the 60°-120° range of crossing angles. All pausing events above 4 sec in duration for such crossings involved significant MT deformations. For example, the extreme outlier seen for high motor assay (Fig. S4, middle panel) corresponds to the case where MT crossing had an un-deformed angle of 65.9° but became completely anti-parallel due to cargo activity. The distribution of dwell times for all intersection angles pooled together in all cases was well approximated by an exponential decay (Fig. S5) with a few notable outliers. All outlier events occurred for crossings with nearly opposite MT polarities (0°-30° range), though in the special case discussed above the alignment resulted from MT bending rather than a priori geometry.

Legends to supplemental movies.

Supplemental Movie 1. Cargo motion across an intersection in vivo. Melanosome moving along fluorescently labeled MT in a melanophore encounters another MT, and this encounter leads to buckling of MT that serves as a transport track, and eventual pausing of the melanosome. Numbers indicate time in seconds. Magnification bar is 5 μm.

Supplement Movie 2. Cargo motion across an intersection *in vitro*. An example movie of a crossing event with substantial MT deformation during the crossing. This event corresponds to a sequence of frames shown in Fig. 1B Conformations of MTs before and after the event is comparable. Magnification bar is 2 μm.

Supplement Movie 3. Cargo motion across an intersection *in vitro*. An example movie of a crossing event with a long pause at the intersection during the crossing. This event corresponds to a sequence of frames shown in Fig. 1C. Magnification bar is 4 μm.

CHAPTER 3

CONSTRUCTING 3D MICROTUBULE NETWORKS USING HOLOGRAPHIC OPTICAL TRAPPING

Bergman, J., Osunbayo, O., and Vershinin, M. (2015). Constructing 3D microtubule networks using holographic optical trapping. Sci Rep 5, 18085.

www.nature.com/scientificreports

SCIENTIFIC REPORTS

OPEN

Constructing 3D microtubule networks using holographic optical trapping

Received: 09 September 2015
Accepted: 11 November 2015
Published: 10 December 2015

J. Bergman, O. Osunbayo & M. Vershinin

Developing abilities to assemble nanoscale structures is a major scientific and engineering challenge. We report a technique which allows precise positioning and manipulation of individual rigid filaments, enabling construction of custom-designed 3D filament networks. This approach uses holographic optical trapping (HOT) for nano-positioning and microtubules (MTs) as network building blocks. MTs are desirable engineering components due to their high aspect ratio, rigidity, and their ability to serve as substrate for directed nano-transport, reflecting their roles in the eukaryotic cytoskeleton. The 3D architecture of MT cytoskeleton is a significant component of its function, however experimental tools to study the roles of this geometric complexity in a controlled environment have been lacking. We demonstrate the broad capabilities of our system by building a self-supporting 3D MT-based nanostructure and by conducting a MT-based transport experiment on a dynamically adjustable 3D MT intersection. Our methodology not only will advance studies of cytoskeletal networks (and associated processes such as MT-based transport) but will also likely find use in engineering nanostructures and devices.

Precisely constructed networks of rigid filaments are of broad interest. MTs are intriguing building blocks for nanoscale construction and mechanical engineering due to their small diameter, high rigidity and ability to sustain directed transport. For example, biomimetic engineering applications are starting to adopt MT-based motility to route and deliver nanoscale cargo[1–4] but are severely limited by the lack of suitable nano-assembly techniques. Traditional *in vitro* approaches predominantly feature MTs fixed to a flat (typically coverslip) surface. Pillars and ridges on the coverslip surface have been used to produce suspended MTs that overhang freely or bridge several attachment points[5,6]. Such techniques are sufficient to sustain basic nano-transport but are neither flexible nor precise. Filaments cannot be positioned or re-positioned as needed, and 3D layouts are either impossible to achieve or highly restricted. Thus, existing approaches do not allow one to construct custom designed networks (whether the design is biologically inspired or technologically required).

Interest in constructing MT networks is further motivated by their importance in biological research. MT cytoskeletal networks in living cells are critical for tasks such as cell organization, and cargo transport. Despite this, the complexity of the 3D network and its role in cargo routing remains poorly characterized. It is often necessary to study cytoskeletal processes under controlled conditions[7] but current *in vitro* techniques are unable to model complex 3D networks[8,9]. For example, cargo distribution within living cells cannot be fully understood without taking into account the cytoskeleton's 3D nature e.g.[10,11]. *In vivo* research is advancing rapidly to accommodate this need. Live cell 3D particle tracking techniques are steadily growing in number and sophistication e.g. [12–14]. A live cell's 3D MT network can now be visualized via super-resolution microscopy[15,16], yet it is currently impossible to replicate the observed arrangement *in vitro*. Therefore, it is impossible to decouple the effects of intracellular regulation from the role of cytoskeletal topological complexity in a parallel *in vitro* study.

Our approach directly addresses these concerns. First, we demonstrate how to manipulate individual MTs in 3D. Refractive microspheres cross-linked to MTs serve as 3D positioning nodes which can be held and moved independently with HOTs. Key advantages of holography[17] are scalability (hundreds of traps can be created and manipulated independently), 3D capability (traps can be defined anywhere within the accessible flow cell volume) and compatibility (often, HOT can be added to a system without modifying the pre-existing optical setup[18]). Prior related HOT-based techniques e.g. [19,20] served as an inspiration for our work but cannot be directly applied to MTs.

Department of Physics & Astronomy, Department of Biology, Center for Cell and Genome Science, University of Utah, 84112 Salt Lake City UT. Correspondence and requests for materials should be addressed to M.V. (email: vershinin@physics.utah.edu)

Second, we show how to scale up our technique to assemble fully 3D MT networks, including efficient methodologies for assembling, storing, and integrating network building blocks. Finally, we demonstrate how our technique can be utilized to model and direct molecular motor transport by assembling 3D MT-MT crossings with dynamic control over filament angle and separation: features important for cargo routing[16,21].

Results

In this work we manipulate MTs devoid of artificially induced chemical modifications, or MT-associated proteins, to retain maximum flexibility in modeling MT-based transport and biomechanics (chemical complexity can be introduced via a straightforward alteration of our assay). We orient individual MTs by tethering refractive microspheres (hereafter bead handles or BHs) along each filament (Fig. 1) which can then be manipulated in 3D via HOTs to construct complex 3D MT networks (Figs 2 and 3). Model cargos with enzymatically active motors (hereafter motorized cargos or MCs) and chemical factors regulating their activity may be incorporated to study transport on these networks (Figs 1 and 4). This strategy presents several challenges: (1) BHs need to have robust affinity for MTs so that adsorption onto MTs is efficient and stable; (2) BHs with many high affinity MT sites on their surfaces may serve to cluster MTs, so special care must be taken to ensure MTs can be manipulated individually. Below we describe how each challenge was addressed in detail.

(1) BH-MT affinity. Silica is our chosen BH material due to its high density (see below). We biotinylate the BHs' surface (Biotin-PEG-Silane) and then attach biotin-tris-NTA via a neutravidin bridge (Fig. 1b). Finally, we specifically attach a full-length enzymatically dead kinesin-1 mutant (E237A in hKIF5A) with a C-terminus HIS6 tag to confer BH-MT affinity (Fig. 1a–c). BH surfaces can be functionalized with various amounts of E237A kinesins to tune the robustness of BH-MT attachment.

(2) BH-MT clustering. BH and MT concentrations can be tuned to prevent BHs and MTs from forming unintended mesh-works (Supplementary Video 1) during mixing. Optionally, BHs and MTs can be co-incubated briefly on a nutator to facilitate occasional BH-MT association (Figs 1d and 2a). Long term separation between these components within the flow cell is achieved by using high density materials for BHs (e.g. silica). Upon admission into the flow cell, BHs sink while MTs float, thus quickly and reliably separating these otherwise coalescing species. Note: coverslip surface must be blocked well to prevent BH and MT coverslip adhesion (see Methods).

Ideally, a flow chamber will exhibit sparse MT coverage with about 2–3 BHs per field of view. As discussed above, it is often easiest to start network construction by capturing a BH pre-attached to a MT (Fig. 2a) in one HOT. A standalone BH may then be captured by an independent HOT and held near the MT at a desired displacement from the already attached BH (Fig. 2b). Firm attachment is quickly observed for BHs functionalized with high amounts of enzymatically dead kinesin. We refer to BH-MT-BH assemblies as "dumbbells" due to their shape. Dumbbells are tested for structural integrity and are then moved by repositioning one or both of the BHs with a HOT (Fig. 2c).

It is often desirable to ascertain that two BHs are connected by a single MT rather than a MT bundle, however doing so via direct imaging often proves difficult. A third "reporter" bead may then be attached to the dumbbell a few microns away from the BHs (Supplementary Fig. 1) and its diffusion can be analyzed (Supplementary Fig. 2) to evaluate the stiffness of the dumbbell's backbone, similar to previous approaches[22]. This technique is convenient enough in practice to be used *in situ* as a generic quality control step. Other optical trapping based techniques[23] are also compatible with our setup.

Our assay also allows mechanical properties of filament networks to be varied. For example, BH-MT linkage stiffness can be tuned by varying the number of motor cross-bridges and/or the nature of the cross-bridges (e.g. using shorter motor constructs). Alternatively, mechanical and chemical properties of MTs could be adjusted by varying tubulin polymerization conditions or adding MT-associated proteins[24]. Notably, mechanical properties of individual MTs can be easily pre-screened (Supplementary Fig. 1,2), so that mechanically heterogeneous networks can be easily designed and built with our approach.

To increase network construction efficiency, building blocks (free BHs, single beads with an attached MT, or whole dumbbells) can be captured and/or fabricated anywhere within the flow cell and then stockpiled in a designated location for subsequent use. An added benefit of silica beads is their propensity to remain relatively stationary upon settling to the surface. This allows all building blocks to be stored in designated areas. A sample stage equipped with absolute position gauge with micron-scale readout precision facilitates repeatedly accessing the stockpile location.

To study transport across complex 3D MT networks, MCs can be added to the assay buffer (Fig. 1a,c,d) prior to admission into the flow cell (here: silica beads with WT hKIF5A motors). Beads of significantly different diameters are used to distinguish MCs from BHs. MT polarity for each dumbbell is readily determined *in situ* by observing the motility direction of an MC driven by a known motor type, e.g. kinesin-1 (Fig. 2d–g).

To demonstrate basic dynamic network construction, we depict assembly of a 3D MT-MT intersection - the fundamental unit of network complexity. Two dumbbells are stretched taut. One MT (horizontal MT, Fig. 3a and Supplementary Video 2) is raised high enough to move over the perpendicular MT without forming inadvertent BH-MT attachments (Fig. 3b), since BHs bind MTs nearly instantaneously on contact. After MT-MT cross formation, filament separation and intersection angle can be freely adjusted (Fig. 3c,d). Z-axis positioning is easily calibrated (Supplementary Fig. 3,4) and positioning precision of 50 nm is reliably achieved. This is comparable to or better than the relevant *in vivo* length scale[16].

Our approach also allows us to cross-link MT filaments into stable 3D arrangements, i.e. self-supporting 3D networks. Figure 3e–l demonstrates this capability. A MT cross (Fig. 3g) is initially deformed into a dome shape by HOTs (Fig. 3i). Additional dumbbells are then used to cross-link the base of the dome structure (Fig. 3i, j), resulting in a dome that maintains its shape without HOT support (Fig. 3k,l). This geometry was chosen for demonstration purposes because it is visually simple, while displaying the key features: all MTs are substantially bent so the integrity of the structure is immediately apparent upon inspection and the shape has significant extent in all three dimensions (no single plane intersects all the beads in this network).

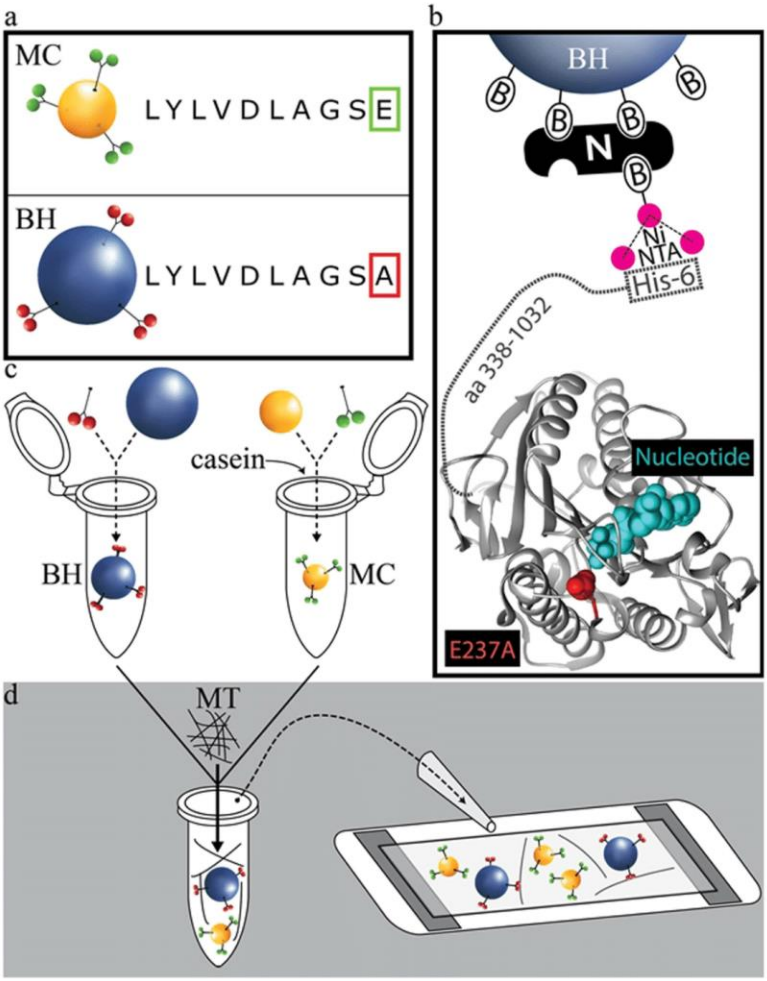

Figure 1. Basic BH-MT tethering strategy and preparation of assay constituents. (**a**) Motorized cargos are functionalized with WT hKIF5A while bead handles are functionalized with non-motile mutant hKIF5A (E237A). Construct sequences for kinesin-1 are otherwise identical, consisting of full length KHC and a HIS6 tag at the C-terminus. (**b**) BHs are specifically bound to E237A hKIF5A via a biotin-neutravidin-biotin sandwich (B-N-B in the figure) functionalized with a Nickel-activated tris-NTA molecule that binds with high affinity to the HIS6 tag on the E237A hKIF5A construct. Protein structure shows kinesin-1 motor domain. E237A mutation is highlighted in red and is in close proximity with a nucleotide (cyan). (**c**,**d**) BHs and MCs are prepared separately (see Methods), then combined together with MTs in assay buffer and finally are introduced into a flow chamber to allow filament network assembly.

The construction capabilities we show above are fully compatible with most established *in vitro* motility assay types (we also envision construction of 3D filament structures as a scaffolding for cell culture experiments). For example, kinesin-1 motors show robust motility when moving along a MT suspended above the surface (Supplementary Fig. 5a). More complex experiments, e.g. studies of kinesin inhibitors are also easy to implement. Kinesin motility can be partially inhibited, for example by the addition of ATPγS (Supplementary Fig. 5b). The resultant magnitude of inhibition we observe is similar to what is expected from previous reports[25,26].

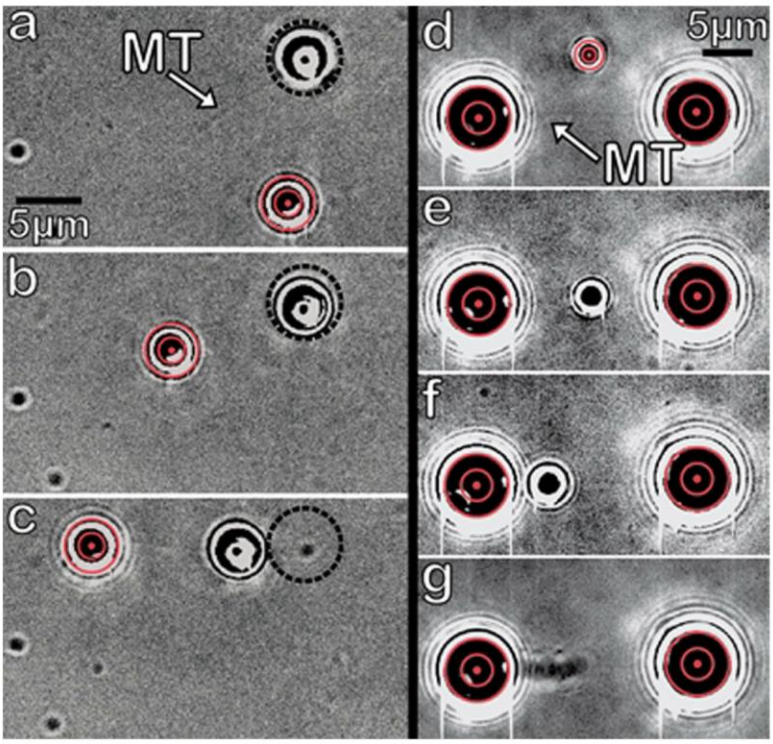

Figure 2. Dumbbell assembly and polarity characterization. (**a**) BH (highlighted by dotted black circle) starts out pre-attached to a MT and resting on the surface with second stand-alone BH close-by (red bulls-eye indicates it is being held in a HOT). (**b**) Trapped BH is maneuvered into close proximity to the "free" end of the MT. (**c**) MT attaches to trapped BH, and whole dumbbell assembly is moved by repositioning the HOT. Dotted black circle highlights original bead position. (**d**) A dumbbell is held taut by 2 HOTs, with a trapped MC nearby. (**e**) The MC is positioned to interact with the MT and is released upon binding. (**e**–**g**) The MC's displacement indicates the MT's polarity (here: plus end on the left). Movie frames corresponding to MC motion are averaged together to highlight that MC displacement is steady and continuous, rather than a result of detachment and reattachment.

In fact, our approach is advantageous over techniques using MT attachment to glass slides even for the simplest motility assays because cargos (artificial or *ex vivo*) can be positioned far away from the glass slide, eliminating concerns regarding non-specific cargo-glass interactions, or variations in biophysical or chemical parameters near the surface.

A model *in vitro* transport experiment (Fig. 4 and Supplementary Video 3) demonstrates the additional advantages of our approach to enable more complex motility experiments. An MC is maneuvered (via an independent HOT) to engage one of the MTs making up a pre-built 3D MT-MT intersection. The MC attaches to a MT far from the crossing site and proceeds through the intersection with a clearly observable tug of war event (Fig. 4a–f). Characterizing the forces involved in such low motor number tug-of-war events is straightforward in our suspended MT system by examining BH displacement in their respective HOTs (Supplementary Fig. 6); this is essentially impossible with prior techniques. In our system, we routinely observe teams of kinesin motors (on a single cargo) engaging in a tug of war when interacting with transverse MT filaments at an intersection. These events are common *in vivo* and play a significant role in cargo transport at MT intersections[21].

Such tug of war events affect cargo velocity and direction of motion, as well as the final outcome of the crossing events *in vitro*[9] (e.g. whether the cargo proceeds along the original MT or switches to the intersecting filament). The same dynamics is likely important *in vivo*[16]. Intracellular transport cannot be fully understood without first quantitatively studying cargo routing in a baseline environment free of confounding cellular regulatory factors[7]. Our ability to characterize forces associated with tug of war events in our system is therefore essential to accurately

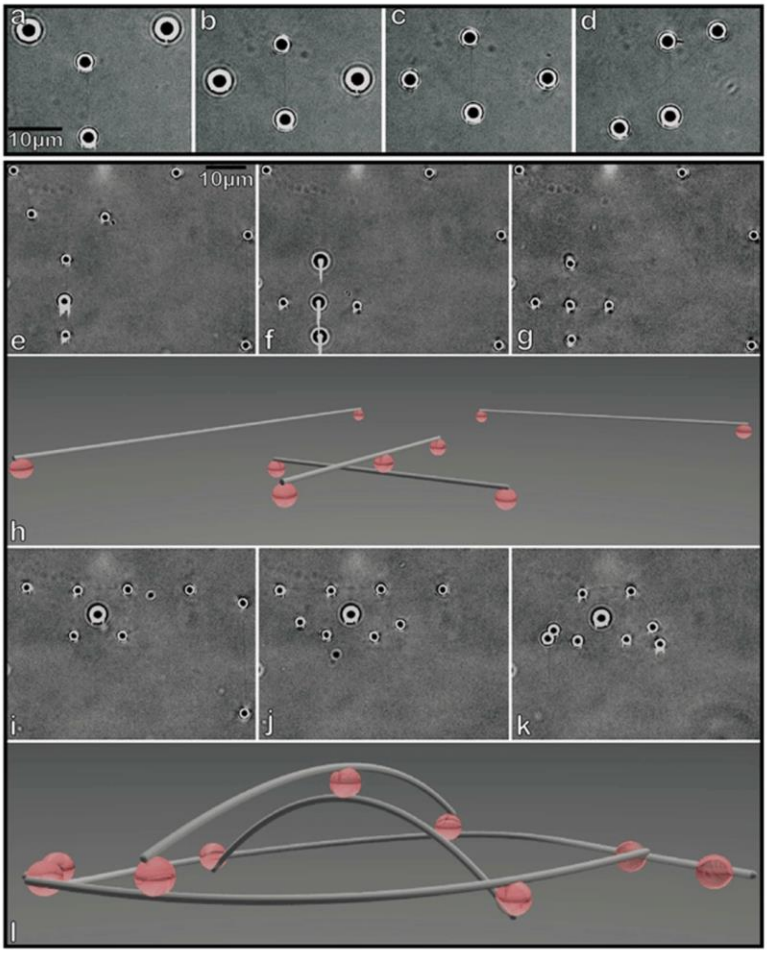

Figure 3. 3D network assemblies. Demonstration of dynamic control of a MT intersection **(a–d).** 2 dumbbells are situated perpendicular to one another with the horizontal dumbbell raised relative to the vertical dumbbell by approximately 5 μm (**a**). The dumbbells are overlaid (**b**), then positioned at the same height (**c**), then reoriented to make a 45° angle (**d**), demonstrating the ability to adjust MT network geometry on demand. Assembly of a static 3D network (**e–l**). Four dumbbells are assembled, with one dumbbell featuring a BH attached in the middle (**e**). Two dumbbells are overlaid (**f**) and then bound together via the BH at the point of intersection (**g**). The 3D schematic of the resulting arrangement is shown in (**h**). The MT cross is reoriented and the outlying BHs are brought closer to the center until the central BH is displaced by ~3.5 μm out of the base plane (**i**). The apparent diameter of the central bead is larger due to the bead being displaced from plane of focus. Additional dumbbells are then "wound" around the cross's peripheral BHs (**i,j**). The 3D assembly is then let go by the HOTs (**k**) and is able to maintain its own structure. 3D schematic for the final assembly is shown in (**l**).

model the general problem of cargo routing. A more detailed study is clearly desirable but is outside the scope of this work.

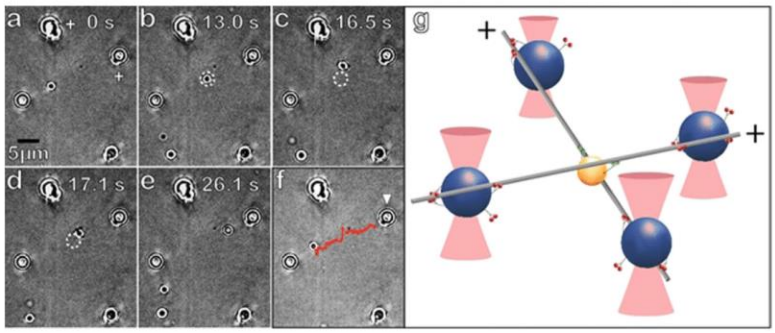

Figure 4. Technique validation for motility assays. (**a**) A MT crossing with 500 nm vertical filament separation is shown. An MC starts out progressing towards the intersection on the overlying MT. (**b**) MC reaches intersection and a tug of war ensues. The MC which is engaged on both MTs, starts to migrate up the transverse MT (**c**), but then after 0.6 seconds, disengages the transverse MT and snaps back (**d**) to once again solely translocate along the original MT (**e**). (**f**) Trace of the MC's progression (red) overlaid on the original frame of the sequence shown in (**a**). This event is representative for assays with MC-MT binding fraction slightly below saturation. White arrow in (**f**) indicates the BH whose position is tracked (Supplement Fig. 6). (**g**) Graphical model (not to scale) depicting the key aspects of the set-up in (**a**–**f**) and tug of war scenario in frame (**c**).

Discussion

Our technique has two key features which set it apart from existing approaches: 1) the ability to control individual filament positioning in 3D with high fidelity and 2) the ability to incorporate multiple filaments to create complex 3D MT networks. Our approach is not only useful for motility assays and biomechanics experiments but can also be used to "wire up" nanodevices for molecular motor based transport e.g. [3]. For example, some proposed biosensor designs[3] rely on molecular motors to transport targeted analytes throughout distinct microchip compartments in a bead assay configuration. This concept has been validated[3], but an inability to design definitive MT networks has hampered the technology's progress. Our method finally enables the construction of arbitrary MT networks to route cargo in a customized manner. Our approach can also be easily integrated with other experimental protocols, which for example, may allow investigations of the effects of MT-associated proteins on motor-driven transport in the context of complex 3D MT networks.

Holographic technology is limited by the rate at which trap positions can be updated. This precludes using the HOT technology for experiments such as probing elastic moduli of networks over a wide frequency range[27], or as force clamps[28]. This shortcoming has been overcome in our system by adding a conventional trap with fast repositioning capability to the optical train[18], but at the expense of increased setup complexity.

Another limitation of our system is that construction of structures takes many minutes. Therefore, once constructed, a given network is likely to be reused for many experiments (e.g. motility assays). This allows experiments to be performed in a nearly identical environment which is usually advantageous for experimental design but also places a premium on the ability to visualize MTs without relying on fluorophores that photobleach quickly under intense illumination for a long duration. In addition, since MTs are likely to be arranged without alignment along one direction, we found conventional DIC imaging to be suboptimal for visualization. We have found that direct brightfield illumination imaging[29] works best but our technique would benefit from extremely photostable labeling which could be demonstrated to not affect MT-based transport and elastic properties of the filaments. We stress that better visualization could help speed up the workflow and help scale the system toward more complexity, but this is not currently a critical limitation.

As we show above, our method is also well suited to create interconnected 3D MT geometries to construct shapes and engineering components. Mechanical properties of the filament building blocks can be altered by varying the number of motor cross-bridges, and/or the nature of the cross-bridges (e.g. using shorter motor constructs.) Mechanical properties of individual dumbbells can also be varied within the same assay[24] and can then be easily pre-screened (Supplementary Fig. 1,2) prior to assembly, so that mechanically heterogeneous networks can be easily designed and built with our approach.

Our approach is highly scalable. A typical volume accessible in a single field of view is far larger than typical cellular volume. This potentially allows intracellular MT networks to be replicated *in vitro*, even allowing substantial homothetic magnification. Modern HOT control software (including our setup) allows for 100–200 traps to be simultaneously created and controlled, which is sufficient to construct many MT networks of biological and technological interest. Of course, it is already conceivable that this number of traps will present a limitation if highly complex networks become desirable. In addition, for high number of traps, network visualization will become increasingly difficult and it is likely that highly complex filament structures, such as micron-scale scaffolding or mechanical metamaterials, will require extensions of the technique to permit automated assembly.

In summary, due to its high precision and extreme scalability, our approach enables a wide range of experiments, from single molecule assays to large scale construction of rigid filament scaffolding or cellular scale transport networks. Similarly, many previously inaccessible biomimetic engineering designs become feasible with our system.

Methods

BH preparation. Monodisperse 2 μm silica beads 1% (w/v) (Microspheres-Nanospheres, Cold Spring, NY) were diluted by 20x in EtOH and were reacted with Biotin-PEG-Silane (MW 3400, Laysan Bio, Arab, AL). Biotin-PEG-Silane was added to a final concentration of 11.75 mg/ml per manufacturer recommendation. This amount of Biotin-PEG-Silane ensured we had at least 100X molar excess relative to reactive sites on the 2 μm silica beads (assuming 4.9 OH groups / nm^2 for silica beads[30]). The beads were allowed to react for 1 hour at room temperature, then were washed 3 times in ultrapure water and were re-suspended in ultrapure water to maintain a 1% (w/v) bead concentration.

These biotinylated beads are incubated with an equal volume of 10 mg/ml of neutravidin (Thermo Fisher Scientific, Waltham, MA). The high molar ratio of neutravidin:surface biotin groups (~10:1) ensures that biotin groups are saturated with neutravidin. For daily use, an aliquot of the neutravidin-biotin-silica beads is incubated with 0.1 mg/ml of biotin-tris-NTA, a trivalent NTA derivative crosslinker (Biotechrabbit, Hennigsdorf, Germany) for 15 minutes. Assuming that each neutravidin has three available binding sites after being attached to the bead surface via a biotin ligand, the molar ratio of biotin-tris-NTA : neutravidin sites was at least 10:1. These beads, referred to hereafter as tris-NTA beads, are then activated with a 3X molar amount of $NiCl_2$ or other metal salt such as $CoCl_2$. After a 5 minute incubation, the Ni-NTA beads are diluted 7.5x in BH buffer (35 mM PIPES, 5 mM MgSO4 pH 7.2, supplanted with 1 mM GTP, 2.67 mM ATP, and optionally 40 μM Taxol.) Immotile E237A hKIF5A (full length HC construct, C-terminal HIS6 tag) is then added to a desired concentration (50–70 nM typically), and incubated for 30 minutes. Tris-NTA to HIS6 binding is reversible via the addition of various metal chelators or imidazole[31], which is useful for control experiments.

In summary, our strategy is to saturate previously created surface functionalizing binding sites at every step, and then use as little E237A hKIF5A as functionally necessary (a generally applicable consideration, considering that E237A hKIF5A is effectively a custom made reagent). Our kinesin to glass surface attachment strategy is similar to the one described by the Surrey lab[32].

Motorized Cargo Preparation. Monodisperse 1 μm silica beads 1% (w/v) (Microspheres-Nanospheres, Cold Spring, NY) are diluted 20x in MC buffer (35 mM PIPES, 5 mM MgSO4 pH 7.2, supplanted with 5mM ATP, 5 mM DTT). The use of silica for MCs ensures that the model cargo will have a preferred downward orientation when attached to a MT. Bead materials with density matched to our buffer result in more diffusive MC motion. The desired concentration of wild-type hKIF5A (full length HC construct, C-terminal HIS6 tag) are then added to the motorized cargo buffer, and incubated for 30 minutes. Casein (40 mg/mL stock; 100X final dilution; MP Biomedicals) is added with the motors to block the surface and reduce clumping.

Assay Buffer Preparation. Due to surface passivation, adding components sequentially will displace materials administered prior. Therefore, BHs and MTs are combined and incubated for 2 minutes. Thereafter MCs are added to the solution. The volume ratio of BH:MC:MT components is 85:10:5. The resulting mix is then quickly admitted into the flow cell.

Coverslip Silanization. #1.5 Borosilicate coverslips (VWR, Radnor, PA) are subjected to a chemical etch in Piranha solution for 1 hr. Coverslips are then washed 3 times in ultrapure water and then are dried in an oven for 1 hour at 100 degrees. The coverslips are then incubated in a beaker containing 10% Hexamethyldisilazane (HMDS) (Gelest, Morrisville, PA) solution in toluene for at least 1 hour (overnight is better). These HMDS-treated coverslips are then washed 3 times in EtOH, once in ultrapure water and are then cured in the oven at 100 degrees for 1 hour.

Flow Chamber Preparation. A flow chamber is constructed by attaching an HMDS-treated coverslip to a coverslide via parallel strips of double-sided tape (3 M, Saint Paul, MN). 1 flow chamber volume of 10% pluronic F-127 (Sigma-Aldrich, St. Louis, MO) in ultrapure water is admitted and allowed to incubate for 15 minutes. Then 2 flow chamber volumes of casein (40 mg/ml in PMEE) is administered and allowed to sit for 15 minutes.

Our approach is similar to the one described previously[33] however we find that additional blocking with casein improves surface blocking performance. Many similar techniques have been developed e.g. [33,34]. They are likely to provide similar or better performance. However, casein blocking alone, even using κ-casein isoform exclusively, does not provide acceptable blocking for our assays.

Optics and imaging. Imaging was performed using a Nikon Eclipse-Ti microscope equipped with a high-magnification, high-NA objective (Nikon Plan Apo VC 100 oil, 1.40 NA). A high-resolution camera (iXON DU897; Andor Technology USA) and Nikon NIS elements AR software (Nikon Instruments USA, Melville, NY) were used to record experiments. Typical field of view size for this work was ~55μm × 55μm.

The holographic optical trap system was set up as previously described[18]. Briefly, a spatial light modulator (Boulder Nonlinear Systems, Lafayette, CO) was installed in an optical plane conjugate to the back focal plane of the objective. BioRyx software (Haemonetics, Braintree, MA) was used to define and control holographic trap arrangement.

Microtubule Preparation. Porcine tubulin (Cytoskeleton, Denver, CO) was polymerized according to the manufacturer's protocol to produce MTs with a tubulin concentration of 140 μM. All MTs used in this work were

taxol-stabilized. Polymerized MTs are then diluted 100x in MT buffer (35 mM PIPES, 5 mM MgSO4 pH 7.2, supplanted with 1 mM GTP, and 40 μM Taxol.)

Kinesin Purification. hKIF5A KHC dimers (wildtype sequence with HIS6 tag on C-terminus) were expressed in an E. coli system as previously described[35]. Briefly, full length KHC with N-terminus MBP solubility tag was expressed and purified. The MBP tag was then proteolytically cleaved as a final purification step.

References

1. Hess, H. & Vogel, V. Molecular shuttles based on motor proteins: active transport in synthetic environments. *J. Biotechnol.* **82,** 67–85 (2001).
2. Muthukrishnan, G., Hutchins, B. M., Williams, M. E. & Hancock, W. O. Transport of semiconductor nanocrystals by kinesin molecular motors. *Small* **2,** 626–630 (2006).
3. Carroll-Portillo, A., Bachand, M., Greene, A. C. & Bachand, G. D. *In vitro* Capture, Transport, and Detection of Protein Analytes Using Kinesin-Based Nanoharvesters. *Small* **5,** 1835–1840 (2009).
4. Aoyama, S., Shimoike, M. & Hiratsuka, Y. Self-organized optical device driven by motor proteins. *Proc. Natl. Acad. Sci. USA.* **110,** 16408–16413 (2013).
5. Roos, W. H. *et al.* Dynamic kinesin-1 clustering on microtubules due to mutually attractive interactions. *Phys. Biol.* **5,** 046004 (2008).
6. Tarhan, M. C., Orazov, Y., Yokokawa, R., Karsten, S. L. & Fujita, H. Suspended microtubules demonstrate high sensitivity and low experimental variability in kinesin bead assay. *The Analyst* **138,** 1653–1656 (2013).
7. Vale, R. D. The role of reconstitution in cytoskeleton research. *Methods Enzymol.* **540,** xix–xxiii (2014).
8. Huber, F. *et al.* Emergent complexity of the cytoskeleton: from single filaments to tissue. *Adv. Phys.* **62,** 1–112 (2013).
9. Ross, J. L., Ali, M. Y. & Warshaw, D. M. Cargo transport: molecular motors navigate a complex cytoskeleton. *Curr. Opin. Cell Biol.* **20,** 41–47 (2008).
10. Dupont, A. *et al.* Single Particle Tracking in Living Cells: Is the Third Dimension Worth It? *Biophys. J.* **104,** 650a (2013).
11. Liu, S.-L. *et al.* Three-Dimensional Tracking of Rab5- and Rab7-Associated Infection Process of Influenza Virus. *Small* **10,** 4746–4753 (2014).
12. Liu, S.-L. *et al.* Fast and High-Accuracy Localization for Three-Dimensional Single-Particle Tracking. *Sci. Rep.* **3** (2013).
13. Katayama, Y. *et al.* Real-time Nanomicroscopy via Three-Dimensional Single-Particle Tracking. *Chemphyschem Eur. J. Chem. Phys. Phys. Chem.* **10,** 2458–2464 (2009).
14. Toprak, E., Balci, H., Blehm, B. H. & Selvin, P. R. Three-Dimensional Particle Tracking via Bifocal Imaging. *Nano Lett.* **7,** 2043–2045 (2007).
15. Huang, B., Wang, W., Bates, M. & Zhuang, X. Three-Dimensional Super-Resolution Imaging by Stochastic Optical Reconstruction Microscopy. *Science* **319,** 810–813 (2008).
16. Bálint, Š., Vilanova, I. V., Álvarez, Á. S. & Lakadamyali, M. Correlative live-cell and superresolution microscopy reveals cargo transport dynamics at microtubule intersections. *Proc. Natl. Acad. Sci.* **110,** 3375–3380 (2013).
17. Grier, D. G. & Roichman, Y. Holographic optical trapping. *Appl. Opt.* **45,** 880–887 (2006).
18. Butterfield, J., Hong, W., Mershon, L. & Vershinin, M. Construction of a high resolution microscope with conventional and holographic optical trapping capabilities. *J. Vis. Exp. JoVE* (2013). doi: 10.3791/50481
19. Plewa, J., Tanner, E., Mueth, D. & Grier, D. Processing carbon nanotubes with holographic optical tweezers. *Opt. Express* **12,** 1978–1981 (2004).
20. Agarwal, R. *et al.* Manipulation and assembly of nanowires with holographic optical traps. *Opt. Express* **13,** 8906 (2005).
21. Osunbayo, O. *et al.* Cargo Transport at Microtubule Crossings: Evidence for Prolonged Tug-of-War between Kinesin Motors. *Biophys. J.* **108,** 1480–1483 (2015).
22. Pampaloni, F. *et al.* Thermal fluctuations of grafted microtubules provide evidence of a length-dependent persistence length. *Proc. Natl. Acad. Sci. USA.* **103,** 10248–10253 (2006).
23. van Mameren, J., Vermeulen, K. C., Gittes, F. & Schmidt, C. F. Leveraging Single Protein Polymers To Measure Flexural Rigidity†. *J. Phys. Chem. B* **113,** 3837–3844 (2009).
24. Hawkins, T., Mirigian, M., Selcuk Yasar, M. & Ross, J. L. Mechanics of microtubules. *J. Biomech.* **43,** 23–30 (2010).
25. Schliwa, M., Shimizu, T., Vale, R. D. & Euteneuer, U. Nucleotide specificities of anterograde and retrograde organelle transport in Reticulomyxa are indistinguishable. *J. Cell Biol.* **112,** 1199–1203 (1991).
26. Cohn, S. A., Ingold, A. L. & Scholey, J. M. Quantitative analysis of sea urchin egg kinesin-driven microtubule motility. *J. Biol. Chem.* **264,** 4290–4297 (1989).
27. Mizuno, D., Head, D. A., MacKintosh, F. C. & Schmidt, C. F. Active and Passive Microrheology in Equilibrium and Nonequilibrium Systems. *Macromolecules* **41,** 7194–7202 (2008).
28. Lang, M. J., Asbury, C. L., Shaevitz, J. W. & Block, S. M. An Automated Two-Dimensional Optical Force Clamp for Single Molecule Studies. *Biophys. J.* **83,** 491–501 (2002).
29. Gutiérrez-Medina, B. & Block, S. M. Visualizing individual microtubules by bright field microscopy. *Am. J. Phys.* **78,** 1152–1159 (2010).
30. Zhuravlev, L. T. The surface chemistry of amorphous silica. Zhuravlev model. *Colloids Surf. Physicochem. Eng. Asp.* **173,** 1–38 (2000).
31. Huang, Z., Hwang, P., Watson, D. S., Cao, L. & Szoka, F. C. Tris-Nitrilotriacetic Acids of Sub-nanomolar Affinity Toward Hexahistidine Tagged Molecules. *Bioconjug. Chem.* **20,** 1667–1672 (2009).
32. *Microtubules, in vitro*, Volume 115, Second Edition. (Academic Press, 2013).
33. Dixit, R. & Ross, J. L. Studying plus-end tracking at single molecule resolution using TIRF microscopy. *Methods Cell Biol.* **95,** 543–554 (2010).
34. Ionov, L., Synytska, A., Kaul, E. & Diez, S. Protein-Resistant Polymer Coatings Based on Surface-Adsorbed Poly(aminoethyl methacrylate)/Poly(ethylene glycol) Copolymers. *Biomacromolecules* **11,** 233–237 (2010).
35. Smith, T. E. *et al.* Single-molecule inhibition of human kinesin by adociasulfate-13 and -14 from the sponge Cladocroce aculeata. *Proc. Natl. Acad. Sci. USA.* **110,** 18880–18885 (2013).

Acknowledgements

The authors gratefully acknowledge helpful discussions with Dr. Steven Gross and Dr. Saveez Saffarian for helpful discussions. The authors also acknowledge Leslie Mershon for help with experiments and Alyssa Jorgensen for help with figure artwork. Focused ion beam etching made use of University of Utah USTAR shared facilities supported, in part, by the MRSEC Program of the NSF under Award No. DMR-1121252.

Author Contributions

M.V. initiated and guided the project. J.B. and O.O. performed experiments and refined the conceptual implementation. J.B., O.O. and M.V. wrote the manuscript.

Additional Information

Supplementary information accompanies this paper at http://www.nature.com/srep

Competing financial interests: The authors declare no competing financial interests.

How to cite this article: Bergman, J. *et al.* Constructing 3D microtubule networks using holographic optical trapping. *Sci. Rep.* **5**, 18085; doi: 10.1038/srep18085 (2015).

Supplementary Information for

Constructing 3D microtubule networks using holographic optical trapping

J. Bergman, O. Osunbayo, M. Vershinin*

Department of Physics & Astronomy,
Department of Biology,
Center for Cell and Genome Science,
University of Utah,
Salt Lake City UT 84112

**e-mail address: vershinin@physics.utah.edu*

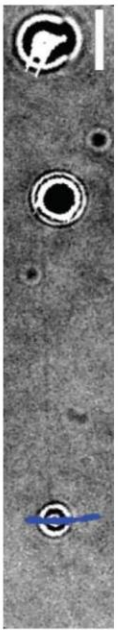

Supplementary Figure 1: MT stiffness assay. MTs were held in the imaging plane via two BHs spaced several microns apart and held in holographic optical traps at maximum displacement to assure no slack in the MT. The free end of the MT was then allowed to move under the influence of Brownian fluctuations. A BH acting as fiduciary marker was then placed on the MT to report MT displacements. Bead displacements were predominantly in the transverse direction (blue). Scale bar: 10 μm.

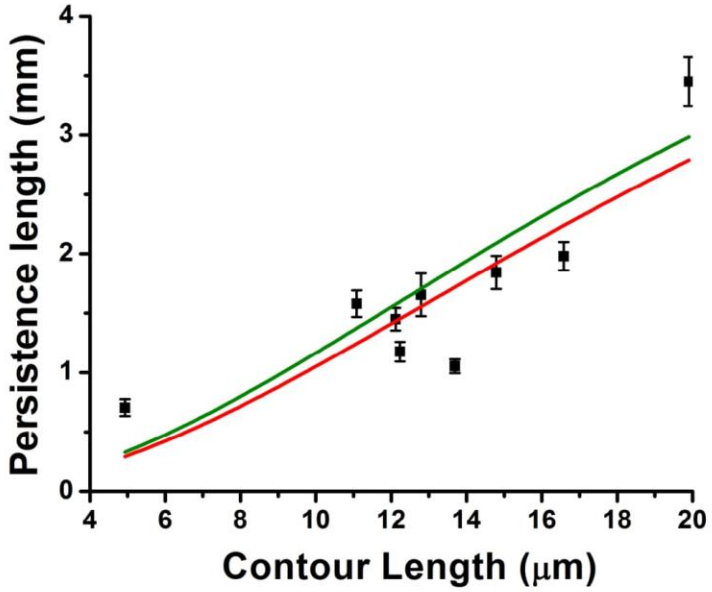

Supplementary Figure 2: MT stiffness analysis. The data acquired as shown in Supplement Figure 1 was analyzed similar to Pampaloni et al. (ref. 20, main text). Though MT lengths in our experiments were not sufficient to accurately estimate saturation level for persistence length of MTs, our data fits well to eqn. 4 in Pampaloni et al. if this parameter value is set at 6.3 mm (red curve). The cross-over length for our data (22.4 ± 1.3 μm) is close to the previously reported fit (green curve).

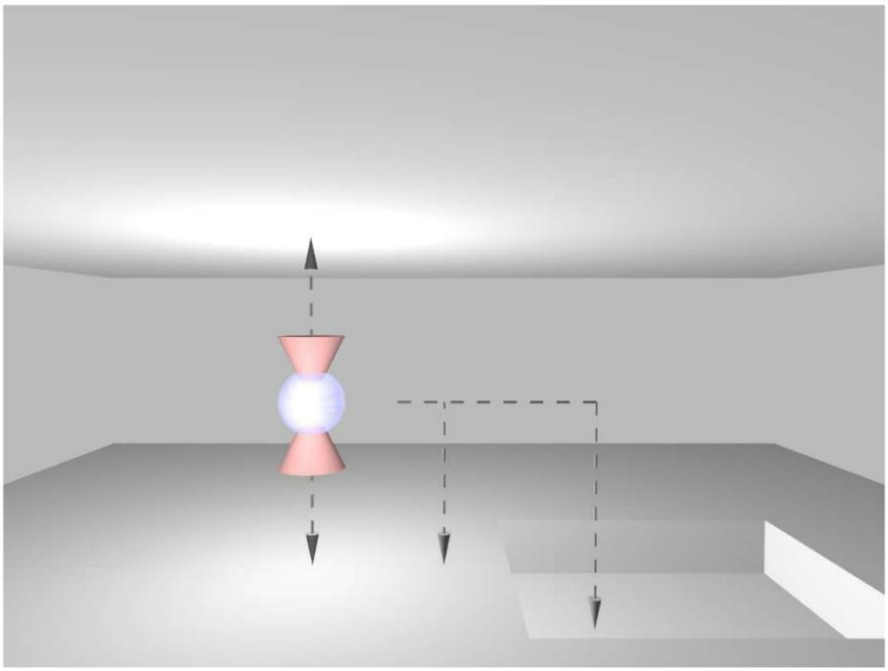

Supplementary Figure 3: Z-axis calibration. Unlike X and Y bead displacements (i.e. movement along axes orthogonal to the microscope axis), the Z-axis displacement cannot be estimated directly from video record. To calibrate Z-axis positioning, we have raised and lowered a NIST traceable silica bead (Microspheres-Nanospheres, Cold Spring, NY) in a holographic optical trap until the bead touched the bounding surface of the flow cell. In one method, the bead was limited by the upper and lower flow cell walls separated by a known distance (left dashed lines and arrows). 10µm polystyrene beads (CV=5%) (Polysciences, Warrington, PA) were typically used as spacers though other spacers (e.g. 5 µm thick double sided tape 68556, TESA, Charlotte, NC) produced nearly identical calibration values. We calibrated the HOT software Z-axis positioning units (i.e. voxel height) by dividing the bead probe's range of motion by the corresponding number of voxels. In another method, we have used focused ion beam to etch a flat bottom trench or a staircase (supplementary figure 4) into a coverslip. Etched trench depths were measured with an atomic force microscope and used as reference distance for voxel height calibration (right dashed lines and arrows). With either approach, when the focal plane of the objective coincided with the bottom plane of the flow cell our voxel height was 131 ± 2 nm (100X NA oil objective). The calibrations for other focal planes of the objective were within 10% of this value.

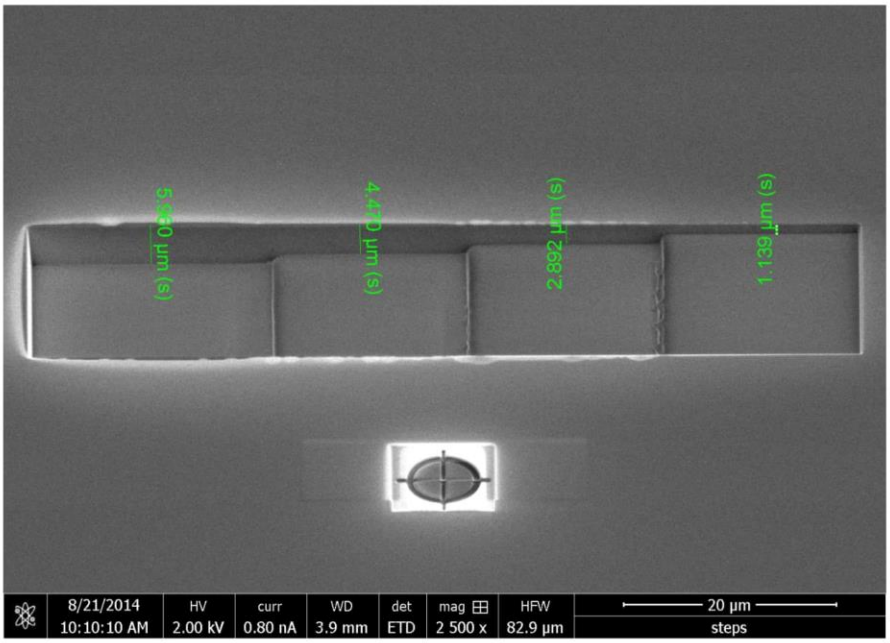

Supplementary Figure 4. Example of 3D coverslip steps used to calibrate voxel height. Focused ion beam etching was used to create step structures which could then be used for Z-axis calibration (Supplement Fig. 3). Steps of ~1µm height were typically used.

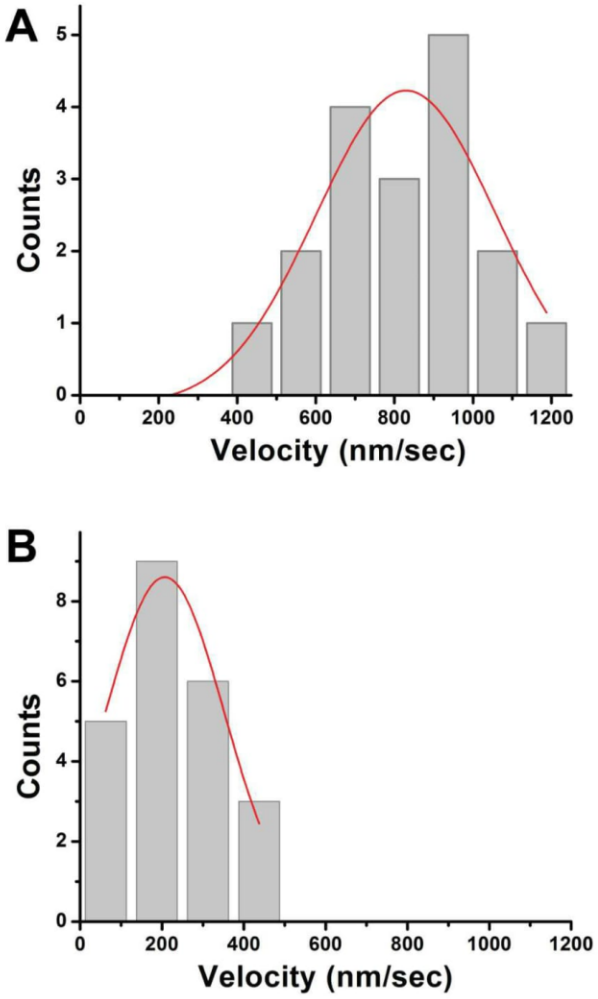

Supplementary Figure 5. Motility assays on suspended MTs. Healthy motor velocities (814±45 nm/sec; n=18; mean±SEM) are seen for kinesin-1 driven MCs (A). However, adding ATPγS inhibitor (ATP: ATPγS molar ratio 2.25:1) reduces the velocities significantly (233±117 nm/sec; n=23; mean±SEM); t-test $p<10^{-13}$.

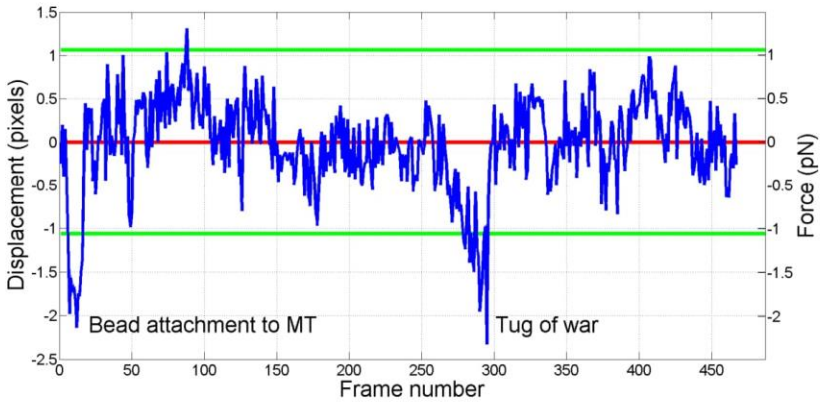

Supplementary Figure 6. BH tracking and force readout. Tracking of the position of the upper right BH in Fig. 4 and Supplementary Video 2 (bead is highlighted by arrow in Fig. 4f). The bead generally shows limited diffusion around its median bead position (red line) and instantaneous bead position is typically within 2 standard deviations of the median (green lines). However two sustained deviation outside of these limits are observed. First occurs when an MC is placed on the MT connected to the BH being tracked. The force is exerted on the BH because the MC is initially moved by the HOT resulting in a perturbation when the MC engages on the MT. The second event occurs during MC navigation at the intersection and provides direct readout of the tug of war forces involved in the process. Here the maximum pulling force of 1.4 pN is observed (107 nm/px imaging; 0.95 pN/100 nm optical trap stiffness).

Supplementary Video 1: MT asters on BHs can be induced via prolonged BH co-incubation on a nutator with an excess of MTs. Such asters are easy to discern during an experiment. The video is included for contrast with the controlled assembly we achieve when prolonged co-incubation is avoided.

Supplementary Video 2: Assembly and dynamic adjustment of MT cross arrangement shown in Fig. 3.

Supplementary Video 3: Kinesin-1 driven bead traverses a MT crossing as shown in Fig. 4.

Supplement Text 1: As discussed in the main text, it may be desirable to ascertain that dumbbells consist of two beads connected by a singular MT rather than a MT bundle. In practice, a typical dumbbell we construct is >10 μm in length. Most MTs we and others produce via polymerization under normal conditions are much shorter than this [1]. Therefore the probability of two extremely long MTs being aligned between two beads is very low. A greater concern is that it is difficult to see if shorter MTs are present near a long MT which is linking the dumbbell together. Shorter MTs will not cross-link the dumbbell but may interfere with 3D structural assembly or motility experiments. To test for these unwanted conditions, a third bead may be placed on the dumbbell as shown in Supplement Figure 1. One can then track the displacement of the marker bead (lowest bead in Supplement Figure 1) while holding the other two beads trapped. With this data, one may then conduct MT flexural rigidity analysis as shown in Supplement Figure 2 and evaluate the hypothesis that the persistence length of the dumbbell is on par with a single MT, or a bundle of MTs.

Note that most of the persistence lengths in Supplement Figure 2 are for contour lengths between 11 and 17 μm and the standard deviation for this data is ~0.33 mm (if one subtracts the fitted trend then the standard deviation becomes ~0.32 mm so that our estimate of overall noise is not notably skewed by the slope in the trend). If two MTs were connecting the dumbbell (and therefore if two MTs were diffusing together as one unit) then the second moment of MT cross-section would at least double (greater increase is likely depending on the relative geometric arrangement of the two MTs) leading to a commensurate increase in the observed persistence length. The data uncertainty is likely to add in quadrature leading to a standard deviation estimate of ~0.47 mm. Therefore, we propose discarding all dumbbells (for this range of contour lengths) with persistence length above 2*6.3*(1+(22.4/L)^2)-2*0.47 where L is contour length. In other words, we propose discarding all dumbbells whose persistence lengths are higher than or within two standard deviations of double the fitted trend. More data for the very longest dumbbells will be needed to establish that this criterion works in those cases. However in practice, all dumbbells we have tested to date have passed such a test. As expected, the probability of doubling up of MTs for dumbbells above 10 μm in length is a very unlikely possibility and this likelihood will only decrease as the dumbbell length increases (due to a decrease in number of very long MTs). Thus, such occurrences appear to be of negligible likelihood for the longest dumbbells (>20 μm) and may not be worth explicit testing.

Another consideration yields similar conclusions, though less directly. If we assume that doubling up of MTs in a dumbbell occurs randomly, then half of such dumbbells would be cross-linked by oppositely oriented MTs. In that case, kinesins on MCs would be free to engage on both MTs and such engagements would produce observable tug of war events [2]. Therefore, the healthy unidirectional MC motion routinely observed in our work further argues that dumbbells crosslinked by two or more MTs are negligibly rare.

Supplement Text 2: The development of this technique took several years and was interrupted several times due to technical difficulties. We discuss some of these difficulties below in hopes it will help other implementations of our approach. By far the biggest problem for us was our strict requirement that MTs must remain unmodified except where BHs bind to them. For example, we avoided using biotinylated MTs because we could not envision a way to ascertain that the MT-bound biotins would not interfere with the binding of any MT-associated protein under any conditions or that they would not affect any MT mechanical properties. This put a premium on finding a good agent to put on BHs to serve as "glue". Our trials of a vast number of antibodies have all been fruitless. All antibodies we tested would "slide" along MTs under applied load. Incubating beads with extremely high amounts of antibodies would result in bead clumping. Similarly many MAPs may slide along MTs under applied load and cannot be relied upon to provide a robust fixed attachment point between a bead and a MT, consistent with recent reports [3].

In addition, we desired a "glue" which would allow for nearly instantaneous binding as soon as bead and MT were brought near each other because any significant delay could affect structure assembly rate and binding reliability especially for larger structures. Therefore, our requirements placed a premium on molecular solutions where the binding site was flexibly attached to the tag which we could use to functionalize our BHs. The recombinant expression of enzymatically dead kinesin-1 HC dimers fulfilled all our requirements, although efficient expression of full length kinesins without aggregation initially proved very challenging.

The problem of separating BHs and MTs to prevent aster formation was comparatively easier. We started with polystyrene bead BHs and used extremely high bead and MT dilutions so that it often took us minutes of searching across the flow cell to find any MTs and beads. At such low dilutions, simplest structural assemblies were possible so the proof of principle was obtained early. However, extremely low dilutions and extremely long searches were not practical and moreover polystyrene beads were hard to store for later use because they diffused too readily. We therefore switched to silica beads which readily sunk to the bottom. However, casein-blocked surfaces were not blocked well-enough and beads would bind to the surface after some time. We therefore developed better surface passivation techniques which solved our issues with the storage of prebuilt components for later assembly. Through routine use of such assays we discovered that silica beads sunk fast enough that they could be mixed with MTs for a short time, then admitted into glass slides and they would efficiently spatially segregate from the MTs if MTs were at a low enough concentration as described in the main text. This finally made all the pieces we needed readily available for fast and efficient workflow.

The final challenge for us was finding a way to reliably attach enzymatically dead motors to beads. This is essential because if the attachment is not robust then such dead motors may detach from BHs and reattach along MTs. This was observed early on and efforts were made to improve bead to motor attachments.

As the technique stands today, many MT crosses and similar simple 3D structure can be assembled and used in one day by one operator. The typical assembly time for such simple structures is a few minutes

for a trained experimentalist. The workflow is convenient and practical, especially since many experimental designs allow complex 3D structures to be subjected to many repeated experiments.

References Cited:

1. Lin, Y.-C., Koenderink, G. H., MacKintosh, F. C. & Weitz, D. A. Viscoelastic Properties of Microtubule Networks. *Macromolecules* **40,** 7714–7720 (2007).
2. Osunbayo, O. *et al.* Cargo Transport at Microtubule Crossings: Evidence for Prolonged Tug-of-War between Kinesin Motors. *Biophys. J.* **108,** 1480–1483 (2015).
3. Hinrichs, M. H. *et al.* Tau Protein Diffuses along the Microtubule Lattice. *J. Biol. Chem.* **287,** 38559–38568 (2012).

CHAPTER 4

THE EFFECT OF TEMPERATURE ON MICROTUBULE-BASED TRANSPORT BY CYTOPLASMIC DYNEIN AND KINESIN-1 MOTORS

Reprinted with permission from Biophysical Journal

Hong, W., Takshak, A., Osunbayo, O., Kunwar, A., and Vershinin, M. (2016). The Effect of Temperature on Microtubule-Based Transport by Cytoplasmic Dynein and Kinesin-1 Motors. Biophys J 111, 1287–1294

Biophysical Journal
Article

Biophysical Society

The Effect of Temperature on Microtubule-Based Transport by Cytoplasmic Dynein and Kinesin-1 Motors

Weili Hong,[1] Anjneya Takshak,[3] Olaolu Osunbayo,[2] Ambarish Kunwar,[3] and Michael Vershinin[1,2,*]
[1]Department of Physics & Astronomy and [2]Department of Biology, University of Utah, Salt Lake City, Utah; and [3]Department of Biosciences and Bioengineering, Indian Institute of Technology Bombay, Powai, Mumbai, Maharashtra, India

ABSTRACT Cytoplasmic dynein and kinesin are both microtubule-based molecular motors but are structurally and evolutionarily unrelated. Under standard conditions, both move with comparable unloaded velocities toward either the microtubule minus (dynein) or plus (most kinesins) end. This similarity is important because it is often implicitly incorporated into models that examine the balance of cargo fluxes in cells and into models of the bidirectional motility of individual cargos. We examined whether this similarity is a robust feature, and specifically whether it persists across the biologically relevant temperature range. The velocity of mammalian cytoplasmic dynein, but not of mammalian kinesin-1, exhibited a break from simple Arrhenius behavior below 15°C—just above the restrictive temperature of mammalian fast axonal transport. In contrast, the velocity of yeast cytoplasmic dynein showed a break from Arrhenius behavior at a lower temperature (~8°C). Our studies implicate cytoplasmic dynein as a more thermally tunable motor and therefore a potential thermal regulator of microtubule-based transport. Our theoretical analysis further suggests that motor velocity changes can lead to qualitative changes in individual cargo motion and hence net intracellular cargo fluxes. We propose that temperature can potentially be used as a noninvasive probe of intracellular transport.

INTRODUCTION

Intracellular transport along microtubules (MTs) facilitates and maintains cellular order, and makes possible the existence of spatially extended cells such as neurons. In most cells, cargo transport operates in a variety of environmental conditions, including a wide range of temperatures. Even for mammals, this range can be as wide as 5–45°C for hibernating species (1). The temperature dependence of in vivo transport velocities has often been reported to be Arrhenius-like (2), but non-Arrhenius deviations, including cold block of transport below ~12°C, are also well established (2). The origin of this rich set of in vivo phenotypes is unclear.

Intracellular transport is often driven by small ensembles (n = ~2–6) of molecular motors (3,4). When opposite polarity motors are present in the same ensemble, the sign and magnitude of net cargo velocity reflect the balance of competitive or alternating mechanochemical activity of various motors (5–7). Thus, it is impossible to gain a quantitative understanding of temperature-dependent in vivo phenotypes without knowing the temperature dependence of the enzymatic activity of individual kinesin and dynein motors that drive transport. However, this aspect of motor function is poorly understood. Previous variable-temperature in vitro motility assays with kinesins (8–10) have been limited to a relatively narrow temperature window that roughly covers the survival range of most mammals. Broader ranges have been explored via biochemical methods (11,12), but not biophysical ones. Although published data on kinesin is somewhat limited, scant variable temperature data are available for cytoplasmic dynein. In this work, we aimed to address this gap in understanding by examining kinesin and cytoplasmic dynein motilities under controlled in vitro conditions, with identical environmental factors affecting motor activity.

We first used bead assays to examine how the velocities and force-production abilities of kinesin-1 and mammalian cytoplasmic dynein motors change with temperature. Measurements of velocity were prioritized over measurements of the motor enzymatic rate because mechanochemical coupling efficiency remains controversial for many motors (especially cytoplasmic dynein) even at the single-molecule

Submitted December 7, 2015, and accepted for publication August 2, 2016.
*Correspondence: vershinin@physics.utah.edu
Editor: Jennifer Ross.
http://dx.doi.org/10.1016/j.bpj.2016.08.006

level. We were surprised to find significant differences between kinesin and dynein motilities as a function of temperature. We use theoretical modeling to examine how our findings relate to motor ensemble performance, and further discuss the implications of our data for biological phenotypes and cell biology experiments.

MATERIALS AND METHODS

Motor purification

Mammalian cytoplasmic dynein was purified from rat brain as previously described (13). Full-length KIF5A heavy-chain dimers were expressed and purified as previously described (14). The minimal, GST-dimerized *Saccharomyces cerevisiae* dynein construct (15) (purified protein) was a generous gift from the lab of Dr. Ronald Vale.

In vitro motility assay

In vitro motility assays involving attachment of motor proteins to 1-μm-diameter polystyrene beads were performed as previously described (14). Motility and force production were determined using a 980 nm laser trap in accordance with previously described protocols (16) except that bead positions were recorded using a high-speed video camera (MQ003MG-CM; Ximea, Golden, CO) at 4000 fps and subsequently tracked using custom software (MATLAB, The MathWorks, Natick, MA). This approach was used to avoid condenser contact with the sample and thereby ensure better temperature uniformity and control. Note that the pKa shift of our PIPES-based buffers was negligible over the relevant temperature range.

For motility measurements, the optical trap was shut off as soon as bead binding to MTs was observed. Processivity was measured for bead binding fractions of 0.3 or below.

Temperature control

The full details of our setup differ from existing variable-temperature optical trapping setups (10,17–19) and will be described in detail elsewhere. Briefly, a customized Peltier thermoelectric stage (PE120; Linkam, Tadworth, UK) was used to control the slide temperature. A sapphire cover glass was used to maximize heat conductivity between the temperature control plate and the assay. We ensured good temperature contact by using a thin layer of water between the sapphire cover glass and the thermal stage. We also minimized heat sinking by eliminating condenser contact with the sapphire cover glass. To do so, we avoided using back focal plane interferometry to record and track bead positions, and instead used a high-speed camera (recording rate: 4000 fps) and custom video tracking software for this purpose. We calibrated the assay sample temperature with ± 0.5°C precision using several independent noncontact methods, including measuring bead diffusion (20–22), performing fixed-point calibration, and measuring the thermal shift of the peak of emission spectra for Cd-Se and Cd-Te quantum dot fluorescence (23). Further details of the temperature control and calibration will be published elsewhere.

Simulations

We used the stochastic model developed by Kunwar et al. (24,25) to simulate the temperature dependence of bidirectional cargo transport by multiple molecular motors of opposite types. The details of our model are further described in Supporting Materials and Methods in the Supporting Material.

RESULTS

We first examined the temperature dependence of the velocity of mammalian cytoplasmic dynein and mammalian kinesin-1 (Fig. 1). The velocities of beads driven by the kinesin-1 family member KIF5A and mammalian cytoplasmic

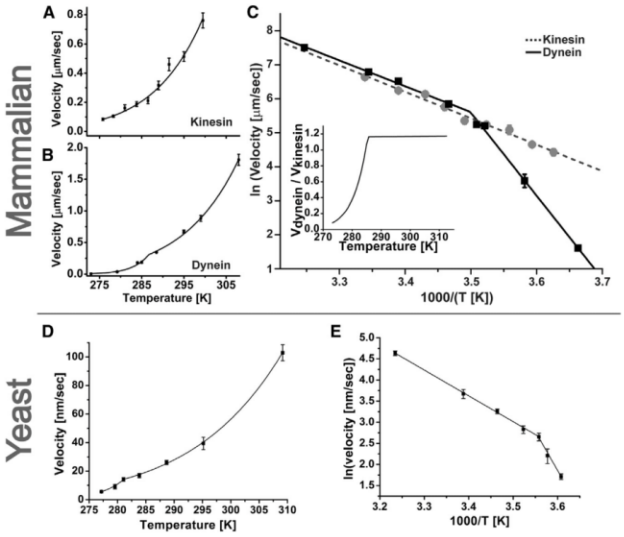

FIGURE 1 Temperature impacts the velocities of kinesin and mammalian cytoplasmic dynein differently. (*A*) Kinesin velocity and Arrhenius fit (*solid line*) down to 8°C. (*B*) Dynein velocity and fit to a piecewise Arrhenius trend (*solid line*) with a crossover at ~15°C. (*C*) Direct comparison of the trends in (*A*) (*dashed gray line*) and (*B*) (*solid black line*) on the logarithmic Arrhenius plot. Inset: ratio of the fit curves obtained in (*A*) and (*B*) plotted on a linear scale. (*D*) Yeast cytoplasmic dynein velocity and fit to a piecewise Arrhenius trend (*solid line*) with a crossover at ~8°C (activation energy 50.5 kJ/mol and 151.5 kJ/mol above and below 8°C, respectively). (*E*) Arrhenius plot of (*D*). Error bars, mean ± SE.

dynein (in the absence of any regulatory cofactors; Fig. S1) were similar between ~15°C and ~27°C (Fig. 1 *A*) and followed a simple Arrhenius temperature dependence in this range. The activation energy extracted from the Arrhenius fit to the velocity data was ~65 kJ/mol, which is slightly higher than that previously reported for another kinesin-1 isoform, KIF5B (9). This trend persisted above 27°C when velocity was measured within ~10 min of temperature change. However, beads were increasingly immotile on MTs afterward, consistent with previous reports of kinesin denaturation at elevated temperatures (8,10). The activation energy for mammalian cytoplasmic dynein above ~15°C was just slightly below that of KIF5A: ~59 kJ/mol and dynein showed no signs of motor degradation up to 37°C.

In contrast to kinesin-1, the velocity of mammalian cytoplasmic dynein (but not kinesin-1) crossed over to a distinct Arrhenius trend below 15°C (Fig. 1, *B* and *C*) with an effective activation energy of ~154 kJ/mol. The net effect was that the dynein velocity declined far more quickly than the kinesin velocity (Fig. 1 *C*). To test whether the rapid decline in velocity at low temperatures is a universal feature of cytoplasmic dyneins, we measured the temperature dependence of velocity for a minimal recombinant *S. cerevisiae* cytoplasmic dynein construct whose movement has biophysical characteristics similar to those of native yeast dynein (15). We found that this dynein also showed a break from simple Arrhenius behavior, but at a much lower temperature: the Arrhenius trend at high temperatures had an activation energy of 50.5 kJ/mol above 8°C and 151.5 kJ/mol below that point (Fig. 1, *D* and *E*).

The striking divergence between dynein and kinesin velocities at low temperatures prompted us to examine whether other key motility parameters showed a comparable change at low temperatures (Fig. 2). We found that cytoplasmic dynein's processivity was 0.69 ± 0.09 μm/s at 10°C. This value is within error bars of the processivity measured for identically purified cytoplasmic dynein at room temperature (0.74 ± 0.08 μm/s (13)). We observed a statistically significant decline in processivity for kinesin-1, from 841.5 ± 0.2 μm/s at room temperature to 497.7 ± 0.09 μm/s at 5°C, confirming a previous qualitative observation of a decline in kinesin's processivity with temperature (10). We also measured kinesin (Fig. 2 *D*) and dynein (Figs. 2 *E* and S2) force production at the lowest temperatures where motility was fast enough to allow for reliable force measurements, and observed no statistically significant changes relative to room temperature. In the case of KIF5A kinesin-1, this parallels and slightly extends a previous report for KIF5B (10).

Among the above results, the divergence of kinesin-1 and cytoplasmic dynein velocities at low temperatures stands out as the major qualitative effect because dynein-based motility essentially shuts down below 15°C. By comparison, the decline of kinesin's processivity is significant, but is not sufficient to effectively abrogate transport. This contrast

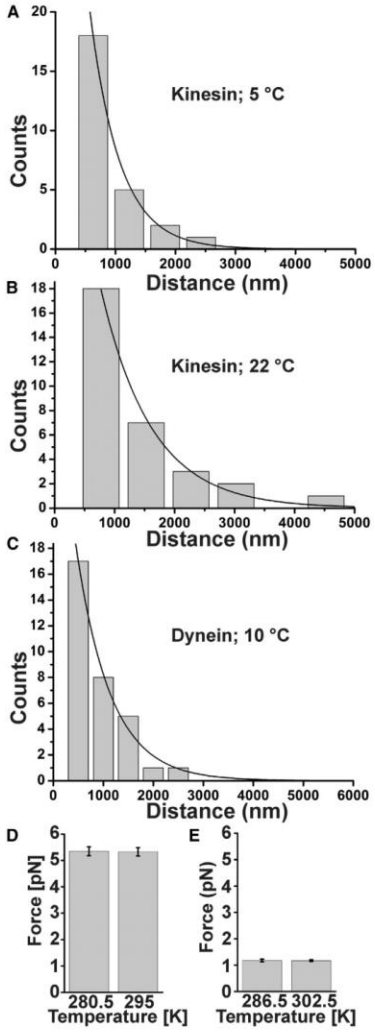

FIGURE 2 Temperature dependence of kinesin and mammalian cytoplasmic dynein processivity and stall force. (*A* and *B*) Kinesin processivity at 5°C (*A*) is 497.7 ± 0.09 nm/s, which is significantly lower than the 841.5 ± 0.2 nm/s obtained at room temperature (*B*). (*C*) Dynein processivity is 0.69 ± 0.09 μm/s at 10°C. Error bars, mean ± SE. (*D* and *E*) Force production by single kinesin (*D*) and mammalian cytoplasmic dynein (*E*) motors (kinesin: 5.3 ± 0.2 pN at 295 K vs. 5.2 ± 0.2 pN at 280.5 K; dynein: 1.2 ± 0.1 pN at 286.5 K vs. 1.2 ± 0.1 pN at 302.5 K; error bars: mean ± SE).

suggests that the net velocities of cargos driven by heterogeneous ensembles of cytoskeletal motors should show an unusual temperature dependence. Without intracellular regulation, kinesin (but not dynein) could effectively move along MTs at low temperatures. Therefore, we expect that cargos that show net retrograde motion at room temperature will move in the anterograde direction at low temperatures. As dynein activity becomes negligible with decreasing temperature, its main contribution to cargo transport will increasingly consist of just binding-unbinding dynamics. In cases where the force production of kinesins and dyneins on the same cargo is balanced (so that four to six dyneins are available for transport versus each kinesin (6,7)), we expect that kinesin activity will almost always be opposed by a team of bound dynein motors, and therefore its role will be to bias the cargo position toward the MT plus end so that rebinding events for dynein motors will be biased in that direction. As a result, this transport has the essential character of a Brownian ratchet whereby the random attachment-detachment kinetics is rectified by an enzymatically active agent.

The effect predicted above is essentially qualitative. Consider motor ensembles in which dynein motors dominate transport at room temperature. If the dyneins shut down at low temperature, then, absent additional regulation, the kinesins would be expected to win by default (using sports terminology). We therefore expect that the prediction would be broadly applicable for biological transport, even though, e.g., dynein's processivity can be modulated substantially by its cofactors (26,27). However, it is also clear that the predicted effect should be amenable to regulation, including regulation of motor parameters other than velocity. For example, kinesin-based cargo motility can effectively shut down at low temperature if, e.g., the motor processivity drops to near zero. We therefore decided to explore quantitatively the range of conditions in which our predicted effect could be observable. To do this, we performed bidirectional transport simulations for a variable number of kinesin and dynein motors under a variety of realistic motor parameters. In this report, we focus primarily on the case of one kinesin versus four dyneins; however, we also considered a case in which kinesin and dynein forces were balanced, and an example of such a simulation is shown in Fig. S3.

Our simulations indeed demonstrate the change in transport directionality at low temperatures (Figs. 3 and 4; see Supporting Materials and Methods for simulation details). Furthermore, they predict this effect not only for realistic motor parameters (Figs. S4 and S5) but also for parameter values that were recently obtained in the presence of dynein cofactors:

Processivity. Our simulations revealed reversals in transport directionality even when dynein processivity was changed by as much as 10-fold (Figs. 4 *B* and S6) (26,27). In addition, we also expect the effect to be present regardless of whether kinesin's processivity is temperature dependent (Fig. S4) or independent (Fig. S5).

Motor force production. Reversals in transport directionality also occurred in simulations in which dynein and kinesin motor stall forces were balanced. The stall force of 2.5 pN was chosen to model the case in Ref. (28) (Fig. S3); however, a different stall force choice would not alter the conclusions qualitatively.

Motor persistence. The detachment rate of kinesin and dynein motors is known to strongly affect the character of bidirectional transport (24). Therefore, we simulated ensemble motor motility using detachment kinetics measured previously by Kunwar et al. (24). The reversal of directional bias with temperature was again a prominent feature of the simulated cargo tracks (Fig. 4, *A–C*). Simulations in which kinesin and dynein persistence under superstall load was varied also showed a directionality reversal with temperature.

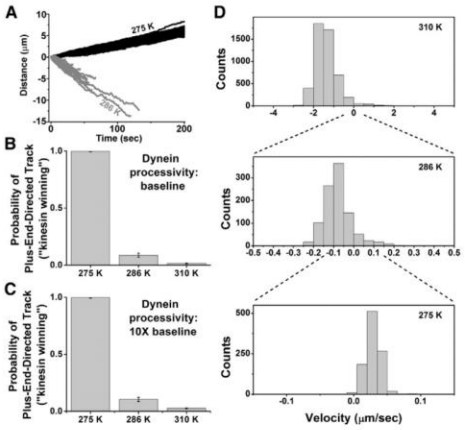

FIGURE 3 Simulations of cargo transported by a team of one kinesin and four dyneins (5 pN and 1.25 pN stall force, respectively). Motors were simulated using the anisotropic force-detachment relationship (Fig. S4 and Supporting Materials and Methods). (*A*) Independent traces of simulated bead motion at 275 K (*black*) and 286 K (*dark gray*) are shown superimposed (100 traces for each temperature). (*B* and *C*) Probability that a simulated trace will have a positive final location (i.e., the probability of kinesin winning) for (*B*) baseline and (*C*) 10× higher dynein processivity values at high, intermediate, and low temperatures (310 K, 286 K, 275 K). (*D*) Transport velocity histograms illustrate that the directional preference reverses sign as a function of temperature. Note that the velocity undergoes large changes with temperature, necessitating the rescaling of the *x* axis.

DISCUSSION

We have observed that mammalian kinesin-1 and cytoplasmic dynein show divergent mechanochemical activity

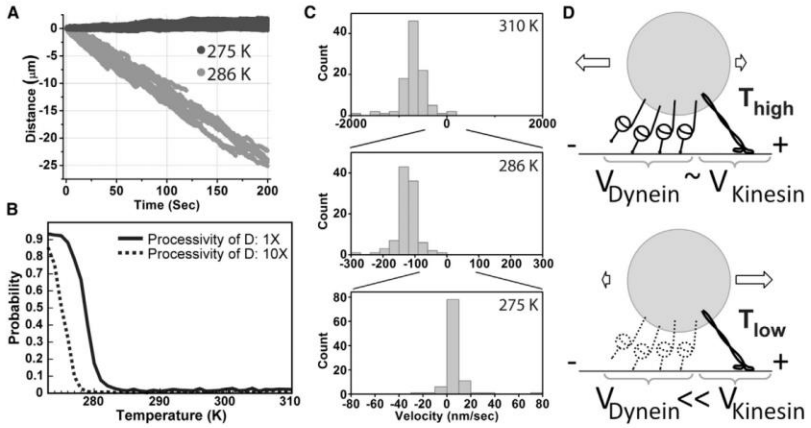

FIGURE 4 Simulations of cargo transported by a team of one kinesin and four dyneins (5 pN and 1.25 pN stall force, respectively). Motors were simulated using the isotropic force-detachment relationship (model B, Fig. S5). (*A*) Independent traces of simulated bead motion at 275 K (*dark gray*) and 286 K (*light gray*) are shown superimposed (100 traces for each temperature). (*B*) Probability that a simulated trace will have a positive final location (i.e., the probability of kinesin winning) for baseline (1×: *solid line*) and 10× (*dashed line*) higher dynein processivity values. (*C*) Transport velocity histograms reveal that the directional preference reverses sign as a function of temperature. Note that the velocity undergoes large changes with temperature, necessitating the rescaling of the *x* axis. (*D*) Model: when all motors are active at high temperatures (*top*), some ensembles of kinesin and dynein motors will exhibit motility with an overall bias in the minus-end direction on MTs. However, at low temperatures (*bottom*), dynein steps dramatically more slowly than kinesin, leading to an overall transport bias in the plus-end direction, as well as other potentially observable effects (Movies S1, S2, and S3).

trends. The extremely high activation energy for dynein at low temperatures means that within just a few degrees below 15°C, dynein transport essentially shuts down relative to kinesin motility. This observation naturally lends itself to understanding the mechanistic origins behind the long-standing mystery of cold block, a phenomenon in which fast axonal transport (FAT) in mammals ceases below ~12°C, even in animals capable of hibernating (2,29). It has long been established that cold block cannot be explained by MT depolymerization at low temperatures (29). On the other hand, the strong temperature-dependent decline of dynein-based motility would likely be sufficient to cause a shutdown of dynein-based and kinesin-based FAT at low temperatures in vivo: a halt of dynein motility by means other than temperature typically results in a gradual stoppage of kinesin-based transport as well, due to intracellular motor regulation (30).

If our hypothesis is correct, one may expect the dynein activation energy to evolve smoothly through 15°C in organisms that are not prone to cold block. Indeed, although we observe a similar piecewise Arrhenius trend in yeast cytoplasmic dynein, the trend break occurs at 8°C. This trend break likely carries no physiological implications: cytoplasmic dynein is nonessential in yeast (31), and in addition, MT stability (and hence MT-associated activity) is compromised at such low temperatures (32).

Many biological enzymes show a simple Arrhenius trend for enzymatic activity near room or physiological temperature but break from this trend at low temperatures, i.e., they have a limited thermal dynamic range (33). We propose that the architecture of cytoplasmic dynein allows for tuning of this dynamic range between species. In principle, the observed cytoplasmic dynein velocity trend break at low temperatures could be due to either a change in the enzymatic rate of the motor or a change in mechanochemical coupling between the two motor domains of dynein. In this context, it is very suggestive that the activation energies above and below the break temperature are extremely close for mammalian and yeast dyneins, and in particular are very high at low temperatures. Thus, we speculate that the thermal dynamic range of cytoplasmic dyneins may be tunable via the same mechanism. If so, we propose that regulation of dynein's thermal dynamic range could occur via its enzymatic domain(s). The AAA ring of dynein certainly has ample complexity (34) to potentially allow for such a mechanism. Coordination between dynein heavy chains is less likely to be the culprit because the velocity of cytoplasmic dyneins is not strongly dependent on the amount of coordination between motor domains (35–37). Furthermore, if such coordination were important under some conditions, one might naively expect the effect to be different for an artificial dimer (the yeast construct we examined) versus a full cytoplasmic dynein complex.

It is also worthwhile to contrast our observations with recent work (36) that identified the C-terminus domain of the dynein heavy chain (present in mammalian but not yeast

motors) as a regulator of dynein's top force production, which likely accounts for the observed differences between yeast and mammalian motor stall forces. It is conceivable that this effect is due to an interaction between the C-terminus domain and the AAA1 domain (36). However, the unchanged activation energy for motor velocity between yeast and mammalian dynein hints that perhaps the force production is not exclusively set within the enzymatically active part of the motor. For instance, the possibility of the C-terminus domain interacting with dynein's linker domain (directly or indirectly) has been put forth before (37), and an allosteric effect is structurally feasible (38). One can therefore envision scenarios in which the C-terminus domain modulates linker docking. This would be conceptually (though not structurally) similar to what is seen in kinesin, where the cover-neck bundle affects the neck-linker affinity for the motor domain during the powerstroke, thereby directly affecting motor force production (39,40).

Our simulations suggest that the reversal of the overall transport direction as a function of temperature is likely to be a very robust effect. This is because the effect arises with very few extremely relaxed starting assumptions. First, bidirectional transport at room temperature needs to be dominated by dynein—a condition that is known to occur for many intracellular cargos. The specific properties of individual dynein motors (processivity, force production, persistence under load, etc.) are not critically important here. All that critically matters is that the dynein ensemble on average wins over the kinesin ensemble at some temperature above the dynein crossover point. The other thing that is needed for directionality reversal is for dynein to effectively cease motility at low temperatures so that the dynamics of the dynein ensemble would be mostly reduced to simple on/off kinetics. We make explicit assumptions in our simulations about the temperature dependence of the on/off rates of dynein as a function of temperature. However, all we really need is for these rates to not differ by many orders of magnitude from the rates at high temperatures. This is a reasonable assumption in light of our experimental data, and would be expected a priori from general biochemistry considerations. Finally, we need the kinesin ensemble to still be active at low temperatures. With these conditions in place, the net cargo motility at low temperatures arises from random binding and unbinding of dynein motors. Indeed, the average number of engaged dyneins remains nearly identical at low temperatures, but the difference grows appreciably at high temperatures as dynein's processivity increases 10-fold (Fig. S7). This remains true regardless of the force-dissociation model we use for kinesin and dynein motors. The fluctuations are minimally biased by any remnant dynein motility, but they are appreciably biased by the kinesin activity. Our simulations show that regardless of the force-dissociation model we use for kinesin and dynein motors, and for both $1\times$ and $10\times$ choices of dynein processivity, the fraction of time in which kinesin is pulling the cargo with a force equal to or exceeding its stall force grows very gradually as the temperature declines and is above 60% at the lowest temperatures (Fig. S8). Any unbinding dynein motor will diffuse around its anchor point on the cargo, which is displaced however slightly by kinesin motor(s) toward the MT plus end. This dynein is then likely to rebind with an average displacement toward the MT plus end (relative to its previous bound position).

From a biophysics perspective, kinesin activity drives the system far from equilibrium and rectifies the on/off fluctuations of the dynein ensemble. In other words, the multiple motor ensemble at low temperatures behaves mostly as a Brownian ratchet (41), whereas the displacement at high temperatures has a significant or even dominant contribution from the powerstroke mechanism. This transition is at the core of why the effect we propose is robust and likely to be quite insensitive to individual motor properties. What is particularly remarkable about this system is that the transition can happen over a very small temperature window relative to the absolute temperature scale.

Keeping in mind that the directionality reversal is likely to be a robust effect, we propose that temperature regulation may present an opportunity to develop a new approach for probing intracellular transport. The qualitative directionality reversal effect should be observable in cell culture or even in vivo after an acute cold shock to $\leq 10^{\circ}$C. The shock would need to occur much faster than any possible cold-shock protein expression (42) to provide a temporal window during which a plus- versus minus-end-directed motility imbalance would be observable and quantifiable. In addition, cold shock can induce cell permeabilization with resultant changes in, e.g., metal ion concentrations and cellular pH (42)—all factors that need to be controlled for. Despite such immediate experimental challenges, we envision that the above approach will become increasingly feasible when the response of cell culture to cold shock is generally better understood.

Also of note, activation energies are not identical (12) across the many kinesin families. Therefore, even though the velocities of cytoplasmic dynein and KIF5A measured here (Fig. 1) are fairly well matched above 15°C, this situation cannot hold for all kinesins. We thus speculate that in other systems (e.g., motor ensembles including kinesin-3), bidirectional transport likely requires additional regulation to maintain even qualitative homeostasis across the mammalian survival range. Of course, such temperature-based feedback could be used in cells to sense temperature.

The temperature dependence of fast MT-based transport can be far more complex in lower species than in mammals (2). This suggests one of two possibilities. First, it is possible that cytoplasmic dynein, like its axonemal counterpart (43), is thermally adaptable to match the thermal range of its species. A tantalizing alternative is that an

as yet unidentified cofactor(s) can regulate the temperature dependence of dynein motility. This is hinted at by the observation that cold acclimation in poikilotherms can lead to increased rates of FAT at low temperatures (44). Either way, the thermal properties of motor-driven transport and its regulation clearly warrant further study.

SUPPORTING MATERIAL

Supporting Materials and Methods, eight figures, and three movies are available at http://www.biophysj.org/biophysj/supplemental/S0006-3495(16)30664-6.

AUTHOR CONTRIBUTIONS

M.V. initiated and guided the project. W.H. and O.O. performed experiments. A.K. directed and guided the theoretical modeling. A.T. implemented the theoretical modeling and contributed to conceptual model refinement. All authors co-wrote the manuscript.

ACKNOWLEDGMENTS

We thank the members of Dr. Richard Vallee's lab for purifying and supplying the mammalian cytoplasmic dynein motors, Dr. R. McKenney and Dr. R. Vale for the generous gift of purified yeast dynein, and Dr. S. Gross and J. Bergman for helpful discussions.

A.K. is supported in part by the Industrial Research and Consultancy Centre at IIT Bombay and by an Innovative Young Biotechnologist Award from the Department of Biotechnology (grant number BT/06/IYBA/2012). This work was supported by National Science Foundation grant number ENG-1563280 to M.V.

REFERENCES

1. Carey, H. V., M. T. Andrews, and S. L. Martin. 2003. Mammalian hibernation: cellular and molecular responses to depressed metabolism and low temperature. *Physiol. Rev.* 83:1153–1181.
2. Cancalon, P. 1985. Influence of temperature on various mechanisms associated with neuronal growth and nerve regeneration. *Prog. Neurobiol.* 25:27–92.
3. Mallik, R., A. K. Rai, …, A. Kunwar. 2013. Teamwork in microtubule motors. *Trends Cell Biol.* 23:575–582.
4. Gross, S. P., M. Vershinin, and G. T. Shubeita. 2007. Cargo transport: two motors are sometimes better than one. *Curr. Biol.* 17:R478–R486.
5. Müller, M. J. I., S. Klumpp, and R. Lipowsky. 2010. Bidirectional transport by molecular motors: enhanced processivity and response to external forces. *Biophys. J.* 98:2610–2618.
6. Soppina, V., A. K. Rai, …, R. Mallik. 2009. Tug-of-war between dissimilar teams of microtubule motors regulates transport and fission of endosomes. *Proc. Natl. Acad. Sci. USA.* 106:19381–19386.
7. Hendricks, A. G., E. Perlson, …, E. L. F. Holzbaur. 2010. Motor coordination via a tug-of-war mechanism drives bidirectional vesicle transport. *Curr. Biol.* 20:697–702.
8. Böhm, K. J., R. Stracke, …, E. Unger. 2000. Effect of temperature on kinesin-driven microtubule gliding and kinesin ATPase activity. *FEBS Lett.* 466:59–62.
9. Kawaguchi, K., and S. Ishiwata. 2000. Temperature dependence of force, velocity, and processivity of single kinesin molecules. *Biochem. Biophys. Res. Commun.* 272:895–899.
10. Kawaguchi, K., and S. Ishiwata. 2001. Thermal activation of single kinesin molecules with temperature pulse microscopy. *Cell Motil. Cytoskeleton.* 49:41–47.
11. Zhao, Y. C., F. J. Kull, and J. C. Cochran. 2010. Modulation of the kinesin ATPase cycle by neck linker docking and microtubule binding. *J. Biol. Chem.* 285:25213–25220.
12. Adio, S., and G. Woehlke. 2009. Properties of the kinesin-3 NcKin3 motor domain and implications for neck function. *FEBS J.* 276:3641–3655.
13. McKenney, R. J., M. Vershinin, …, S. P. Gross. 2010. LIS1 and NudE induce a persistent dynein force-producing state. *Cell.* 141:304–314.
14. Smith, T. E., W. Hong, …, M. Vershinin. 2013. Single-molecule inhibition of human kinesin by adociasulfate-13 and -14 from the sponge Cladocroce aculeata. *Proc. Natl. Acad. Sci. USA.* 110:18880–18885.
15. Reck-Peterson, S. L., A. Yildiz, …, R. D. Vale. 2006. Single-molecule analysis of dynein processivity and stepping behavior. *Cell.* 126:335–348.
16. Vershinin, M., B. C. Carter, …, S. P. Gross. 2007. Multiple-motor based transport and its regulation by Tau. *Proc. Natl. Acad. Sci. USA.* 104:87–92.
17. Svoboda, K., C. F. Schmidt, …, S. M. Block. 1992. Conformation and elasticity of the isolated red blood cell membrane skeleton. *Biophys. J.* 63:784–793.
18. Mao, H., J. R. Arias-Gonzalez, …, C. Bustamante. 2005. Temperature control methods in a laser tweezers system. *Biophys. J.* 89:1308–1316.
19. Bennet, M. A., P. R. Richardson, …, A. C. Jones. 2011. Optically trapped microsensors for microfluidic temperature measurement by fluorescence lifetime imaging microscopy. *Lab Chip.* 11:3821–3828.
20. Fernandez, A. C., and G. D. J. Phillies. 1983. Temperature dependence of the diffusion coefficient of polystyrene latex spheres. *Biopolymers.* 22:593–595.
21. Müller, C. B., and W. Richtering. 2008. Sealed and temperature-controlled sample cell for inverted and confocal microscopes and fluorescence correlation spectroscopy. *Colloid Polym. Sci.* 286:1215–1222.
22. Chung, K., J. K. Cho, …, H. Lu. 2009. Three-dimensional in situ temperature measurement in microsystems using Brownian motion of nanoparticles. *Anal. Chem.* 81:991–999.
23. Li, S., K. Zhang, …, H. Yang. 2007. Single quantum dots as local temperature markers. *Nano Lett.* 7:3102–3105.
24. Kunwar, A., S. K. Tripathy, …, S. P. Gross. 2011. Mechanical stochastic tug-of-war models cannot explain bidirectional lipid-droplet transport. *Proc. Natl. Acad. Sci. USA.* 108:18960–18965.
25. Kunwar, A., M. Vershinin, …, S. P. Gross. 2008. Stepping, strain gating, and an unexpected force-velocity curve for multiple-motor-based transport. *Curr. Biol.* 18:1173–1183.
26. Schlager, M. A., H. T. Hoang, …, A. P. Carter. 2014. In vitro reconstitution of a highly processive recombinant human dynein complex. *EMBO J.* 33:1855–1868.
27. McKenney, R. J., W. Huynh, …, R. D. Vale. 2014. Activation of cytoplasmic dynein motility by dynactin-cargo adapter complexes. *Science.* 345:337–341.
28. Shubeita, G. T., S. L. Tran, …, S. P. Gross. 2008. Consequences of motor copy number on the intracellular transport of kinesin-1-driven lipid droplets. *Cell.* 135:1098–1107.
29. Brimijoin, S., J. Olsen, and R. Rosenson. 1979. Comparison of the temperature-dependence of rapid axonal transport and microtubules in nerves of the rabbit and bullfrog. *J. Physiol.* 287:303–314.
30. Yi, J. Y., K. M. Ori-McKenney, …, R. B. Vallee. 2011. High-resolution imaging reveals indirect coordination of opposite motors and a role for LIS1 in high-load axonal transport. *J. Cell Biol.* 195:193–201.
31. Eshel, D., L. A. Urrestarazu, …, I. R. Gibbons. 1993. Cytoplasmic dynein is required for normal nuclear segregation in yeast. *Proc. Natl. Acad. Sci. USA.* 90:11172–11176.

32. Bellocq, C., I. Andrey-Tornare, …, S. J. Edelstein. 1992. Purification of assembly-competent tubulin from Saccharomyces cerevisiae. *Eur. J. Biochem.* 210:343–349.

33. Fink, A. L., and S. J. Cartwright. 1981. Cryoenzymology. *CRC Crit. Rev. Biochem.* 11:145–207.

34. Qiu, W., N. D. Derr, …, S. L. Reck-Peterson. 2012. Dynein achieves processive motion using both stochastic and coordinated stepping. *Nat. Struct. Mol. Biol.* 19:193–200.

35. DeWitt, M. A., A. Y. Chang, …, A. Yildiz. 2012. Cytoplasmic dynein moves through uncoordinated stepping of the AAA+ ring domains. *Science.* 335:221–225.

36. Nicholas, M. P., P. Höök, …, A. Gennerich. 2015. Control of cytoplasmic dynein force production and processivity by its C-terminal domain. *Nat. Commun.* 6:6206.

37. Höök, P., A. Mikami, …, R. B. Vallee. 2005. Long range allosteric control of cytoplasmic dynein ATPase activity by the stalk and C-terminal domains. *J. Biol. Chem.* 280:33045–33054.

38. Kon, T., T. Oyama, …, G. Kurisu. 2012. The 2.8 Å crystal structure of the dynein motor domain. *Nature.* 484:345–350.

39. Hwang, W., M. J. Lang, and M. Karplus. 2008. Force generation in kinesin hinges on cover-neck bundle formation. *Structure.* 16:62–71.

40. Khalil, A. S., D. C. Appleyard, …, M. J. Lang. 2008. Kinesin's cover-neck bundle folds forward to generate force. *Proc. Natl. Acad. Sci. USA.* 105:19247–19252.

41. Cubero, D., and F. Renzoni. 2016. Brownian Ratchets: From Statistical Physics to Bio and Nano-motors, 1st ed. Cambridge University Press, Cambridge, UK.

42. Underhill, M. F., and C. M. Smales. 2007. The cold-shock response in mammalian cells: investigating the HeLa cell cold-shock proteome. *Cytotechnology.* 53:47–53.

43. King, S. M., S. P. Marchese-Ragona, …, H. W. Detrich, 3rd. 1997. Inner and outer arm axonemal dyneins from the Antarctic rockcod Notothenia coriiceps. *Biochemistry.* 36:1306–1314.

44. Edström, A., and M. Hanson. 1973. Temperature effects on fast axonal transport of proteins in vitro in frog sciatic nerves. *Brain Res.* 58:345–354.

Biophysical Journal, Volume *111*

Supplemental Information

The Effect of Temperature on Microtubule-Based Transport by Cytoplasmic Dynein and Kinesin-1 Motors

Weili Hong, Anjneya Takshak, Olaolu Osunbayo, Ambarish Kunwar, and Michael Vershinin

Supporting Material

Title:

The effect of temperature on microtubule-based molecular motor transport

Authors

W. Hong, A. Takshak, O. Osunbayo, A. Kunwar, M. Vershinin

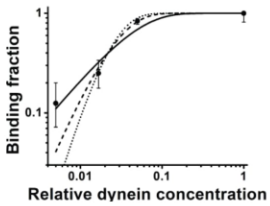

Fig. S1 Single motor activity of cytoplasmic dynein. The binding fraction data for dynein is best fit by single molecule Poisson distribution 1-exp(-n/b) but not by two molecule distribution: 1-exp(-n/b)-(n/b)exp(-n/b) or three molecule distribution 1-exp(-n/b)-(n/b)exp(-n/b))-(n/b)2exp(-n/b)/2 (solid, long dash and short dash curves respectively). Error bars: CI for binomial distribution.

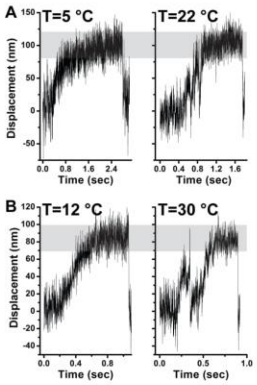

Figure S2. Single motor stalls were experimentally observed for both dynein and kinesin. The stalls were quantified (Fig. 2) for temperatures where motility allowed efficient data collection. Representative examples of motor stall shapes are reported here. Representative stall events for kinesin (A) and dynein (B) motors are shown.

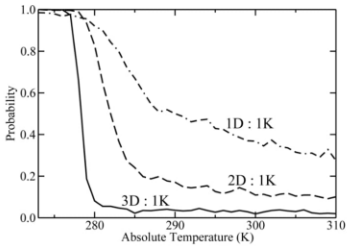

Figure S3. Kinesin "winning probability" for different motor ensembles as a function of temperature. Here, individual dynein (D) and kinesin (K) motor forces were assumed balanced at 2.5 pN. The number of motors in an ensemble is as indicated for each curve. Simulations were performed using the *in-vivo* kinesin-1 and *in-vivo* cytoplasmic dynein parameters given in Text S1 in the Supplementary Material.

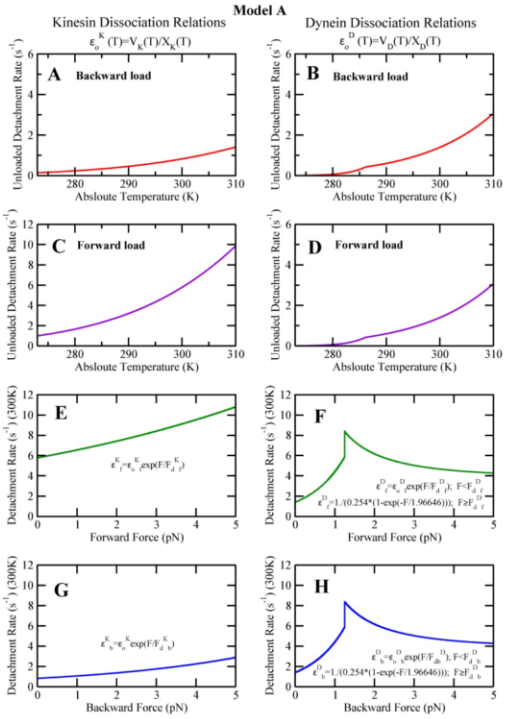

Figure S4. Force- dissociation relations for kinesin-1 and cytoplasmic dynein used in this work for simulations in Fig.3 and the figures in the supplement.

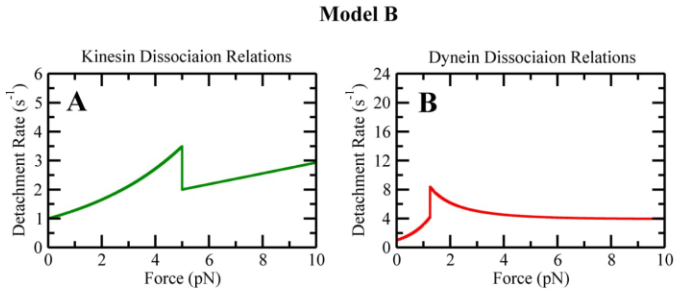

Figure S5: Simulations results in Fig. 4 were performed using detachment kinetics shown in (A) and (B) for Kinesin and Dynein motors respectively.

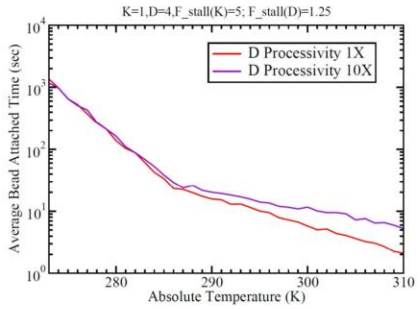

Figure S6. Cargo attachment times show signature of dynein velocity crossover for ensembles of 4 dyneins (1.25 pN stall) and 1 kinesin (5 pN stall) (compare with Fig. 3B). 10X means dynein processivity was increased by a factor of 10.

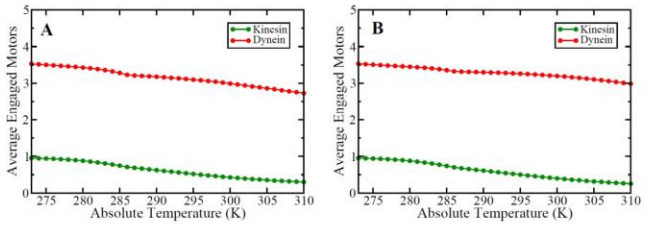

Figure S7. Average ensemble composition for engaged motors. The average number of engaged kinesin and dyneins was calculated for a cargo carrying 4 kinesins and 1 dynein using Model A parameters. We have used 1X (A) and 10X (B) dynein processivity in the simulations but only minor changes at higher temperatures are apparent in the simulated ensembles.

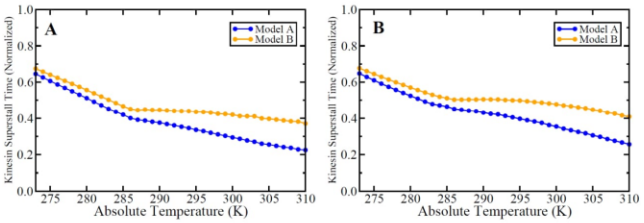

Figure S8. The fraction of time kinesin spends in superstall regime. The gradual decrease in kinesin superstall time fraction as temperature increases is similar for simulations with 1X (A) and 10X (B) dynein processivity.

Movie S1. Simulations of bi-directional transport (Fig. 3) driven by 4 dynein motors and one kinesin at 273 K yielded simulated positions of all motors and the cargo. This data for one representative simulation is shown in movie form (dynein – red, kinesin – green, cargo – black). Motors which are not attached to the MT are not shown so that the number of motors visualized may change from frame to frame.

Movie S2. Simulations of bi-directional transport (Fig. 3) driven by 4 dynein motors and one kinesin at 286 K yielded simulated positions of all motors and the cargo. This data for one representative simulation is shown in movie form (dynein – red, kinesin – green, cargo – black). Motors which are not attached to the MT are not shown so that the number of motors visualized may change from frame to frame.

Movie S3. Simulations of bi-directional transport (Fig. 3) driven by 4 dynein motors and one kinesin at 310 K yielded simulated positions of all motors and the cargo. This data for one representative simulation is shown in movie form (dynein – red, kinesin – green, cargo – black). Motors which are not attached to the MT are not shown so that the number of motors visualized may change from frame to frame.

Text S1.

- **Monte-Carlo Simulation of Temperature Dependent Bi-directional Cargo Motility**

To simulate bidirectional cargo under *in-vitro* and *in-vivo* conditions, we considered a cargo having Kinesin and Dynein motors with various parameters (listed in appropriately labeled Tables later). A Cargo with 'n' Kinesin (Kinesin-1) and 'm' Dynein Motors (Cytoplasmic Dynein) instantaneously attached to the microtubule is abbreviated as (K=n, D=m) in the main text. We used the stochastic model developed by Kunwar *et al.* in [1,2] to simulate the temperature dependence of bidirectional cargo transport by multiple molecular motors of opposing types. The model uses experimentally established parameters for motor function and accurately accounts for many prior experimental results, e.g. the force-velocity curve for kinesin-1[3]. We developed two distinct models to simulate bidirectional cargo motility depending on the detachment kinetics of the involved motors.
In Model A, we considered the anisotropic detachment of Kinesin motors under forward and backward loads measured by Andreasson *et al.* [4], and temperature dependence of unloaded detachment rate of both Kinesin and Dynein motors. While in Model B, we considered isotropic detachment for both sets of motors and used earlier measured detachment kinetics of Kinesin and Dynein motors by Kunwar *et al.* [1].

The common features of both Model A and Model B are briefly described below:

For both models, simulations were performed for temperatures (T) in the range of 273K-310K (0ºC-37ºC) in intervals of 1K. A maximum N number of Kinesin motors and M number of Dynein motors were put on cargo. The motors of both types were modeled as special linkages which exert a restoring force only when they are stretched beyond their rest length and buckle without any resistance when compressed [1,2].The spring constants for both motor types was taken to be k=0.32pN/nm [1,2].The radius of the cargo (r) was taken to be 0.25 μm and the medium viscosity η to be 0.003Pa-s. In our simulations, the velocity of Kinesin and Dynein was dependent on both load felt by the motor, and system temperature.

For both models, Kinesin was considered a simple Arrhenius enzyme whose maximum velocity at zero load (V_o^K) varied with absolute temperature as:

$$V_o^K(T) = A^K * \exp(-E_a^K/(k_B T))$$

Where A^K is the Arrhenius constant for Kinesin; E_a^K is its Activation energy; k_B is Boltzmann Constant and T is the Absolute Temperature. However, Dynein was considered a complex Arrhenius Enzyme because the temperature dependence of its velocity has two distinct domains with two Activation energies: below a critical temperature T_c, Dynein velocity at zero load (V_o^D) is given by

$$V_o^D(T) = A^D * \exp(-E_a^{D1}/(k_B T))$$

While above T_c,

$$V_o^D(T) = A^D * \exp((E_a^{D2}-E_a^{D1})/T_o) * \exp(-E_a^{D2}/(k_B T))$$

Where A^D is the Arrhenius constant for Dynein and E_a^{D1} and E_a^{D2} are its two Activation energies. Kinesin's velocity was considered to reduce sub-linearly with load/ force (F) as

$$V^K(F,T) = V_o^K(T) * (1-(F/F_s^K)^2)$$

While for dynein, the force-velocity relation was super-linear:

$$V^D(F,T) = V_o^D(T) * (1-(F/F_s^D)^{0.25})$$

In both models, each simulation was started with all motors attached to the microtubule. Attached Kinesin and Dynein motors start to step along microtubule in opposite directions with stepping rates obtained from force velocity relations i.e. dividing velocity at any given force and temperature by motor step size. Thus motor can get engaged in a tug-of-war if both sets of motors are simultaneously attached to the microtubule. While engaged in a tug-of-war, a motor could experience load in the same or opposite direction of its stepping. It was assumed that forward load had no effect on the motor velocity and only backward load reduced its velocity/stepping rate.

In our models, individual attached motors can either step on the microtubule or detach from the microtubule, at each time step. Conversely, at each time step unattached motors can reattach to the microtubule with re-attachment probabilities determined from their respective on-rates. The cargo continues along the microtubule, instantaneously driven by a number n of engaged Kinesin motors and/or m number of Dynein motors (where $n \leq N$, $m \leq M$ respectively), and is updated at every time step according to motors'

attachment and detachment events, until the simulation ends, or n+m= 0; indicating all motors have fallen off the microtubule.

In our simulations, motor's detachment rate was influenced by both forward as well as backward load. The detachment kinetics of individual type of motors was different in the two models.

In Model A, the unloaded detachment rate of both sets of motors was considered temperature dependent; and was explicitly calculated by dividing the velocity of motors at a particular temperature T by the travel distance (runlength) at that T:

$$\epsilon_o^K(T) = V_o^K(T) / X_o^K(T) \quad (1)$$

Where $V_o^K(T)$ and $X_o^K(T)$ are the unloaded velocity and runlength of Kinesin at a particular temperature T. $X_o^K(T)$ was assumed to be varying exponentially with temperature as:

$$X_o^K(T) = 0.1*\exp(T/32.64)$$

Further, the detachment kinetics of Kinesin was taken to be anisotropic as studied by Andreasson *et al.* [4]. Anisotropic means that the detachment kinetics was different under the influence of forward and backward loads experienced by the motor. A forward load is the one which the motor feels in the same direction as its stepping; while the backward load opposes/hinders motor's stepping. For Kinesin, the detachment kinetics was uniformly exponential throughout for both forward and backward loads [4]. The forward ($F_d^K{}_f$) and backward detachment forces ($F_d^K{}_b$) for Kinesin were considered to be constant (temperature independent) at 8pN [4] and 4pN [1] respectively. Thus the expressions for Kinesin detachment (as a function of both force and temperature) are:

$$\epsilon^K{}_f(F,T)=\epsilon_o^K{}_f(T)*\exp(F/F_d^K{}_f) \quad \text{forward loads (2)}$$

$$\epsilon^K{}_b(F,T)=\epsilon_o^K{}_b(T)*\exp(F/F_d^K{}_b) \quad \text{backward loads (3)}$$

Similarly, the temperature dependence of unloaded detachment rate of Dynein was modeled as:

$$\epsilon_o^D(T) = V_o^D(T) / X_o^D(T) \quad (4)$$

Where the value of $X_o^D(T)$ was taken to be constant at 689 nm. The detachment kinetics of Dynein was considered isotropic as in [1,2], i.e., the detachment kinetics was similar for both forward and backward loads. Also, the detachment kinetics was different for sub-stall and super-stall regimes for both types of loads. The rate of detachment of Dynein motors was taken to be increasing exponentially with load up to stall force (i.e.

$F<F_s^D$ for both forward and backward loads. For loads greater than or equal to single motor stall force experimentally-measured detachment rates were used [1]. The forward ($F_d^D{}_f$) and backward detachment forces ($F_d^D{}_b$) for Dynein were considered to be constant (temperature independent) as for Kinesin; however, their magnitudes were the same at 0.87pN [1,2]. Thus the expressions for Dynein detachment (as a function of both force and temperature) are:

$$\epsilon^D{}_f(F,T)=\epsilon_o^D{}_f(T)*\exp(F/F_d^D{}_f) \quad \text{sub-stall forward loads (5)}$$

$$\epsilon^D{}_f(F,T)=1./(0.254*(1.-\exp(-F/1.96646))) \quad \text{super-stall forward loads (6)}$$

$$\epsilon^D{}_b(F,T)=\epsilon_o^D{}_b(T)*\exp(F/F_d^D{}_b) \quad \text{sub-stall backward loads (7)}$$

$$\epsilon^D{}_b(F,T)=1./(0.254*(1.-\exp(-F/1.96646))) \quad \text{super-stall backward loads (8)}$$

Plots of equations (1)-(8) are shown in Figure S4. Results obtained from simulation of Model A are shown in Fig 3.

In Model B, the rate of detachment of both Kinesin and Dynein motors was taken to be increasing exponentially with load up to stall force (i.e. $F<F_s^K$ for Kinesin and $F<F_s^D$ for Dynein). Thus, the dependence of Kinesin's and Dynein's detachment rate on force up to stall force is given by

$$\epsilon^K=\epsilon_o^K\exp(F/F_d^K) \quad (9)$$

$$\epsilon^D=\epsilon_o^D\exp(F/F_d^D) \quad (10)$$

For loads greater than or equal to single motor stall force experimentally-measured detachment rates were used [1]. For Kinesin detachment rate in super-stall regime ($F \geq Fs$) is given by

$$\epsilon^K=1.07+0.186*F \quad (11)$$

for *in-vitro* conditions [1]. Experimentally measured detachment rate of Dynein in super-stall regime [1] is given by

$$\epsilon^D=1./(0.254*(1.-\exp(-F/1.96646))) \quad (12)$$

While the rate of detachment of engaged motor was considered to be dependent on load only, there-attachment/on-rates were taken to be independent of both load and Temperature.

Plots of equations (9)-(12) are shown in Figure S5. Results obtained from simulation of Model B are shown in Fig 4.

Time in each simulation was incremented in discrete time intervals of $\Delta t=10^{-5}$s (time step); since this is appropriately smaller than the rate of the fastest event in our system (viz., the detachment rate of Dynein motor at 310K at $F=F_s^D$). The instantaneous probabilities for motor stepping, detachment and reattachment were calculated by multiplying the respective rates with Δt.

Our simulations included the effect of both thermal noise and the viscous drag. The thermal diffusion of the cargo due to T was assumed to be normally distributed with a mean of $(2D\Delta t)$; where D is the temperature-dependent diffusion coefficient of the cargo [1]. D can be calculated via Einstein's Diffusion relation

$$D = (k_B T)/\gamma$$

Where γ is the drag coefficient of the cargo; which for a spherical cargo is a function of the surrounding medium viscosity (η) and the cargo radius (r) as

$$\gamma=6\pi\eta r$$

At each time step Δt, the net force on the cargo due to all attached motors (say F_{net}) was calculated by the algebraic addition of individual forces exerted by all motors. At each time step Δt, net displacement of the cargo due to motors forces and thermal was obtained by adding displacement X_{drift} caused by F_{net} i.e.

$$X_{drift} = (F_{net}/\gamma)*\Delta t$$

and thermal noise X_{random}; which was drawn from a normal distribution with mean square displacement $(2D\Delta t)$.

The final cargo position (x_f) was obtained after the end of simulation and compared with initial position (x_i). If (x_f-x_i) was positive, then Kinesin was considered to win the Tug-of-War; else Dynein. The above procedure was repeated for 1,000 configurations for each Absolute Temperature from 273K-310K; and the probabilities of motor winning as functions of T were analyzed.

- **Parameters used in Simulations for Model A**

1. *In-vitro* Kinesin-1 Parameters

Parameter	**Symbol**	**Magnitude**
Arrhenius Constant	A^K	1.72448E14 nms^{-1}
Activation Energy	$E_a{}^K$	65.05869 kJ/mol
Spring Constant	k_K	0.32 pN/nm
Rest Stalk Length	L_K	110 nm
Step size	d_K	8 nm
Stall Force	$F_s{}^K$	5.00 pN
Forward Detachment Force	$F_{d\_f}{}^K$	8.00 pN
Backward Detachment Force	$F_{d\_b}{}^K$	4.00 pN
Rate of attachment	π^K	5 s^{-1}

2. *In-vitro* Cytoplasmic Dynein Parameters

Parameter	**Symbol**	**Magnitude**
Arrhenius Constant	A^D	1.68497E39 nms^{-1}
Critical Temperature	$T_C{}^D$	286.1722 K
Activation Energy for $T<T_C{}^D$	$E_a{}^{D1}$	201.3638 kJ/mol
Activation Energy for $T\geq T_C{}^D$	$E_a{}^{D2}$	60.9441 kJ/mol
Spring Constant	k_D	0.32 pN/nm
Rest Stalk Length	L_D	50 nm
Step size	d_D	8 nm
Stall Force	$F_s{}^D$	1.25 pN
Forward Detachment Force	$F_{d\_f}{}^D$	0.87 pN
Backward Detachment Force	$F_{d\_b}{}^D$	0.87 pN
Rate of attachment	π^D	5 s^{-1}
Unloaded Runlength	$X_o{}^D$	689 nm

3. *In-vivo* Kinesin-1 Parameters

Parameter	**Symbol**	**Magnitude**
Arrhenius Constant	A^K	1.72448E14 nms^{-1}
Activation Energy	$E_a{}^K$	65.05869 kJ/mol
Spring Constant	k^K	0.32 pN/nm
Rest Stalk Length	L_K	110 nm
Step size	d_K	8 nm
Stall Force	$F_s{}^K$	2.50 pN
Forward Detachment Force	$F_{d\_f}{}^K$	8.00 pN
Backward Detachment Force	$F_{d\_b}{}^K$	2.00 pN
Rate of attachment	π^K	5 s^{-1}

4. *In-vivo* Cytoplasmic Dynein Parameters

Parameter	**Symbol**	**Magnitude**
Arrhenius Constant	A^D	1.68497E39 nms^{-1}
Critical Temperature	To	286.1722 K
Activation Energy for T<To	E_a^{D1}	201.3638 kJ/mol
Activation Energy for T≥To	E_a^{D2}	60.9441 kJ/mol
Spring Constant	k_D	0.32 pN/nm
Rest Stalk Length	L_D	50 nm
Step size	d_D	8 nm
Stall Force	F_s^D	2.50 pN
Forward Detachment Force	$F_{d\_f}^D$	1.74 pN
Backward Detachment Force	$F_{d\_b}^D$	1.74 pN
Rate of attachment	π^D	5 s^{-1}
Unloaded Runlength	X_o^D	689 nm

- **Parameters used in Simulations for Model B**

1. *In-vitro* Kinesin-1 Parameters

Parameter	**Symbol**	**Magnitude**
Arrhenius Constant	A^K	1.72448E14 nms^{-1}
Activation Energy	E_a^K	65.05869 kJ/mol
Spring Constant	k_K	0.32 pN/nm
Rest Stalk Length	L_K	110 nm
Step size	d_K	8 nm
Stall Force	F_s^K	5.00 pN
Detachment Force	F_d^K	4.00 pN
Rate of attachment	π^K	5 s^{-1}
Rate of detachment at zero load	ϵ_o^K	1 s^{-1}

2. *In-vitro* Cytoplasmic Dynein Parameters

Parameter	**Symbol**	**Magnitude**
Arrhenius Constant	A^D	1.68497E39 nms^{-1}
Critical Temperature	T_C^D	286.1722 K
Activation Energy for $T<T_C^D$	E_a^{D1}	201.3638 kJ/mol
Activation Energy for $T\geq T_C^D$	E_a^{D2}	60.9441 kJ/mol
Spring Constant	k_D	0.32 pN/nm
Rest Stalk Length	L_D	50 nm
Step size	d_D	8 nm
Stall Force	F_s^D	1.25 pN
Detachment Force	F_d^D	0.87 pN
Rate of attachment	π^D	5 s^{-1}
Rate of detachment at zero load	ϵ_o^D	1 s^{-1}

3. *In-vivo* Kinesin-1 Parameters

Parameter	**Symbol**	**Magnitude**
Arrhenius Constant	A^K	1.72448E14 nms^{-1}
Activation Energy	E_a^K	65.05869 kJ/mol
Spring Constant	k^K	0.32 pN/nm
Rest Stalk Length	L_K	110 nm
Step size	d_K	8 nm
Stall Force	F_s^K	2.50 pN
Detachment Force	F_d^K	2.00 pN
Rate of attachment	π^K	5 s^{-1}
Rate of detachment at zero load	ϵ_o^K	1 s^{-1}

4. *In-vivo* Cytoplasmic Dynein Parameters

Parameter	Symbol	Magnitude
Arrhenius Constant	A^D	1.68497E39 nms^{-1}
Critical Temperature	To	286.1722 K
Activation Energy for T<To	E_a^{D1}	201.3638 kJ/mol
Activation Energy for T≥To	E_a^{D2}	60.9441 kJ/mol
Spring Constant	k_D	0.32 pN/nm
Rest Stalk Length	L_D	50 nm
Step size	d_D	8 nm
Stall Force	F_s^D	2.50 pN
Detachment Force	F_d^D	1.74 pN
Rate of attachment	π^D	5 s^{-1}
Rate of detachment at zero load	ϵ_o^D	1 s^{-1}

- **References**

1. Kunwar A., Tripathy S.K., Xu J., Mattson M.K., Anand P., Sigua R., Vershinin M., McKenney R., Yu C.C., Mogilner A. and Gross S.P. (2011) Mechanical Stochastic Tug-of-War Models cannot explain Bidirectional Lipid-droplet Transport: *PNAS 108:*18960-18965.

2. Kunwar A., Vershinin M., Xu J. and Gross S.P. (2008) Stepping, Strain-Gating andan Unexpected Force-Velocity curvefor Multiple-Motor-Based Transport: *Current Biology 18:*1173-1183.

3. Schnitzer M.J., Visscher K., Block S.M. (2000) Force production by single kinesin motors. *Nat Cell Biol.* 2:718–723.

4. Andreasson J.O.L., Milic B., Chen G.Y., Guydosh N., Hancock W.O., Block S.M. (2015) Examining kinesin processivity within a general gating framework: eLife 2015:e07403.

CHAPTER 5

COMPLEX NEARLY IMMOTILE BEHAVIOR OF MICROTUBULE-ASSOCIATED CARGOS

5.1 Abstract

We report a minimal microtubule-based motile system displaying signatures of tug-of-war motility. The system consists of a single model cargo driven by an ensemble of N340K NCD motors along a single microtubule. Despite the absence of cytosolic or cytoskeleton complexity, the system shows complex behavior, characterized by sub-diffusive motion for short time lag scales. In addition, the linear MSD dependence for longer time lags is also shown to have non-Gaussian character and cannot be ascribed to a canonical diffusion process. We use variable temperature single particle tracking and analysis to identify the origin of these behaviors as enzymatic activity of mutant NCD. Our results suggest that some of the anomalous motility of cargos commonly observed in cells may be due to tug-of-war states of cargos on a single filament and need not always reflect the properties of the cytoskeletal network or the cytosol.

5.2 Introduction

Microtubule-associated motility enables essential intracellular functions and processes in eukaryotic cells. Hence, observation and modeling of this process is a major

modern research direction. Much less attention is devoted to studies of how cargos do *not* move. The temporary lack of directed cargo motion is often seen but rarely analyzed in depth in particle tracking and analysis studies. It can significantly affect net cargo velocity for one particle and net cargo flux for a population of cargos. In addition, cargos driven by multiple molecular motors can remain immotile for extended periods of time at microtubule intersections due to being bound to multiple filaments at once[1–4]. In such cases, the cargos act as dynamic cross-links for the cytoskeleton and their function bridges the fields of motility and biomechanics[5,6]. Extended stationary periods are therefore a distinct class of motile behavior which requires extensive *in-vitro* and *in-silico* modeling, as well as additional experimental tools to establish the underlying root causes of such events.

Intracellular cargo tracks tend to be highly complex because motion can be driven by a variety of causes, including mechanochemical enzymes[7] and passive diffusion[8] (equivalently, motion can be driven by causes that obey or break detailed balance[9]). The distinction between passive and active motion is crucial. For example, one might use positional fluctuations of an intracellular cargo to calibrate in vivo optical trapping[10], but it is essential to first establish that the chosen cargos are not subject to motor activity. On the other hand, if enzymatic contribution is established, then one can proceed to probe the properties of molecular motors mediating the motility[e.g. 11,12]. It is thus desirable in many experimental contexts to have a simple way to distinguish between active and passive motility.

Mean-squared displacement (MSD) analysis[13] is commonly used to classify single particle motion. Pure Brownian motion leads to linear MSD curves while motion of

individual mechanochemical enzymes often proceeds at constant velocity which produces a quadratic MSD dependence[13,14]. An important subtlety is that Brownian motion is not the only stochastic process that leads to linear MSD curves[15,16]. For example, all it takes is for balanced ensembles of mechanochemical enzymes to oppose each other's motion and a linear MSD can very well arise from an active process. MSD analysis may be convenient and easy to perform, but it is not always appropriate to distinguish active from passive motility.

Motility analysis and modeling is rapidly changing[16,17]. Interest in active fluctuations and awareness of complications in practical data analysis is growing[18,19]. Practical examples of enzymatically driven diffusion are now well established[12]. However, theoretical approaches to teasing out various diffusion and active motility modes from single particle tracking data[15] are still under active development[20,21] and a single standardized approach has yet to emerge. It is however clear that in general, mere tracking and associated analysis is insufficient to relate cargo-scale phenotype to constituent single molecule contributions. There is thus an acute additional need for new experimental probes of complex motility. In this work, we construct a minimal model of an active but apparently diffusive process. We then examine the resulting motility and demonstrate that even in our minimal system, the overall ensemble phenotype is complex. We then capture the fundamental dynamics in our system in a minimal theoretical model and further show how active contribution to the apparent diffusion can be isolated via a simple experimental approach.

5.3 Results and discussion

We have modeled complex motility under controlled conditions by constructing a bead assay in which multiple microtubule-based motors could cross-bridge a cargo to a filament and subsequently engaged in a balanced tug-of-war. To keep the system minimal we have used a single type of motor: N340K mutant of kinesin-14 NCD (non-claret dysfunctional)[22]. Wild type NCD is nonprocessive with a bias for minus-end directed powerstroke[22–26]. The N340K mutant is a bi-directional motor, with more balanced preference for stepping in either direction. Ensembles of N340K NCD motors were previously used in a microtubule gliding assay and showed ensemble bi-directional motility. Most of the motility was reported to be localized, but some contiguous displacements in either direction were too long to be ascribed to diffusion even though overall motile random process appeared roughly stationary[22]. The general view regarding this phenomenon is that the cooperative activity of NCD motors is sufficient to temporarily power directed displacement[9] but the choice of direction occurs via spontaneous symmetry breaking and need not be biased in a specific direction. However, diffusive motion has not been fully ruled out[8].

We studied NCD N340K driven motility in a bead assay to more closely model active bi-directional cargo motion (although technically the glass slide in gliding assays can be thought of as a cargo). The observed motility was consistent with gliding assay phenotype[22]: most beads exhibited limited localized motions while some beads had more extensive bi-directional motility (Figure 5.1). The MSD analysis of tracks revealed that the motion is strongly sub-diffusive on short time scales (Figure 5.1). This prompted us to re-examine them using a more extensive time–averaged MSD (TA-MSD) analysis[5,27,28]

(Figure 5.2A) which revealed a broad distribution of anomalous exponents for lag dependence from near zero to slightly above unity (Figure 5.2B). On the other hand, measurement time dependence showed robust convergence (Figure 5.2A), suggesting that the sub-diffusive process is ergodic. We therefore tentatively consider this behavior to fit in the class of fractional Brownian motion (fBm)[15]. Indeed, the microscopic picture we have is bead-microtubule coupling via variable number of motors at a variety of relative binding positions and hence a variety of coupling strengths, which is the type of a complex system where fBm phenomena are known to arise[28,29]. An essential feature of fBm processes is some form of memory effect built into the system dynamics. In our case, it is likely that the motors themselves provide such memory effect, perhaps due to their complex response under load (which remains poorly characterized for NCD). In this picture, when a motor detaches or attaches to the microtubule, the system then slowly evolves to a new motile state. We would then expect that after some lag time, memory effects would become negligible. This is indeed seen in our data (Figure 5.1B, 5.2A). Beyond about 1 second lag time, MSD curves do show a linear trend. Therefore, on long lag time scales, the system becomes a good model of apparently diffusive behavior.

We then wanted to examine whether the complex behavior above could be directly attributed to the enzymatic activity of NCD. The central idea behind our approach is that biological enzymes typically undergo dramatic changes in activity over a biologically relevant temperature range[30–32] whereas passive processes like diffusion show much less pronounced variation with temperature. We demonstrate below that temperature dependent single particle tracking is indeed a rapid and convenient approach to analyzing the active contribution to apparent diffusion. The linear fits[14] to the long lag

time portion of the MSD curves revealed that the distribution of the effective diffusion coefficients is not Gaussian. At all temperatures, it is highly skewed and reasonably approximated by an exponential distribution (Figure 5.3A,B). This feature is unexpected: approximately Gaussian distributions typically arise in this type of analysis due to the central limit theorem for large data sets. Indeed, this observation is in contrast to e.g. simple Brownian motion of beads in water, for which the distribution of diffusion coefficients is of course approximately Gaussian and varies slowly with temperature (Figure 5.3 C, D). Though exponential density is unusual, it does provide us with a decay scale which we can then use as the characteristic of diffusion at a given temperature. We first highlight that the diffusion coefficient scale at room temperature is 0.008 m^2/sec – more than an order of magnitude lower than the typical diffusion coefficients for regular diffusion of proteins along microtubules[8,33]. This is consistent with the picture that the random process generating the linear MSD is a complex multi-motor interaction. Next, we observed that the characteristic diffusion coefficients extracted in this fashion yielded an excellent fit to the Arrhenius model but not to the linear one (Figure 5.3). The activation energy extracted from the Arrhenius fit was 130 KJ/mol – somewhat high but within the range of activation energies observed for kinesin motors especially for a system of multiple motors where a stepping enzyme would see significant opposing load[34]. It is unlikely that another energy barrier relevant to our system is in this range. For example, the activation energies for protein diffusion along the microtubule lattice are not generally precisely known but are thought to be more than an order of magnitude lower[8]. The energy barriers relevant for the motor-microtubule detachment are of order 10 KJ/mol[35]. We conclude that the apparent diffusion is actually an active process. The last

question we need to address is the unexpected finding that the distribution of effective diffusion coefficients in our assays is extremely skewed. This type of a phenomenon has been observed in many systems and has been recently modeled using the diffusing diffusivities approach[17]. However, this type of a model does not easily map onto the case of enzymatically driven motion. We therefore need a conceptually related theoretical model which would capture the essential features of our system: active power-stroke driven bi-directional motion and passive diffusion without necessarily describing the complex details of multi-motor dynamics. These considerations lead to a bi-directional jump diffusion process, described in 1 dimension by the probability density of the temporal displacement *p(x,t),* which is governed by the Fokker-Planck equation[36]

$$\partial_t p(x,t) = D\partial_{xx} p(x,t) - 2\lambda p(x,t) + \lambda p(x-\delta,t) + \lambda p(x+\delta,t) \quad (1)$$

When the rate of jumps λ is set to zero, this describes the classical diffusion process. For simplicity, jumps in either direction are assumed to have fixed characteristic distance δ and occur at the same rate, so that the system is symmetric. This system then is highly reminiscent of the more general continuous-time random walk (CTRW) processes[15], but our model lacks the long tailed correlations. The advantage of this model is its simplicity: all the moments μ_j of the distribution $p(x,t)$ can be computed analytically (see the appendix below with the derivations done by Christopher Miles in Dr. James Keener group, Department of Mathematics at University of Utah). For example, the model process is first-order stationary, consistent with the assumed dynamics being bi-directionally symmetric.

Ultimately, we are interested in the distribution of diffusion coefficients. That is, we associate an empirical diffusivity with each trajectory, reflecting how the squared

displacement scales with time. In other words, for a given trajectory, we are effectively sampling the random variable:

$$D_s = \frac{x(t)^2}{2t} \tag{2}$$

where *t* is the time between samples, or the inverse of sampling frequency. Then, one could think of the estimate of *D* for each path as an average of these samples. That is, a naïve estimator is just $D_{est} = \frac{1}{N}\sum_{i=1}^{N} D_s^{(i)}$, where N is the number of sample points on a path. Although the actual practice of estimating D for a path using these random variables is considerably more complicated (a weighted linear regression[14]), this estimator can provide the intuition for the curious statistics observed in experiments. The most notable feature of these statistics that we utilize is that the MSD for this process is still linear and the slope can be computed explicitly as the mean estimate of D:

$$E[D_{est}] = D + \lambda\delta^2 \tag{3}$$

We immediately notice that if λ=0, this indeed recovers the true underlying passive diffusion coefficient. We can also see that for enzymatically driven jumps, whose rate λ scales with temperature per Arrhenius law, the effective diffusion coefficient will have identical scaling with the same activation energy. This suggests that our intuition is correct: if passive diffusion is dominant, the empirical diffusivity should scale linearly, and if active, it will scale as a Boltzmann factor.

Further statistics of the process also provide insight into how this active diffusion process can be distinguished from classical diffusion. We recall that the distribution of D was considerably skewed in experimental results. This result can be compared with theoretical prediction for jump diffusion. The skewness of each sample is:

$$skew[D_s] = \frac{32D^3t^2 + 96\delta^2D^2\lambda t^2 + 24\delta^4D\lambda t(4\lambda t+1) + \delta^6\lambda(8\lambda t(4\lambda t+3)+1)}{t\left(4D^2t + 8\delta^2D\lambda t + \delta^4\lambda(4\lambda t+1)\right)\sqrt{8D^2 + 16\delta^2D\lambda + \frac{2\delta^4\lambda(4\lambda t+1)}{t}}} \quad (4)$$

Of course, if each path is an average of N samples, then $skew[D_{obs}] = skew[D_s]/\sqrt{N}$. In the absence of jumps (λ=0), the skewness of each sample is $2\sqrt{2}$, as expected for the chi-squared distribution with 1 degree of freedom. However, when λ>0, the skewness grows. If $\lambda \gg {}^{1}/_{t}$, then the situation is similar in spirit to classical CTRW models: the tails become relatively long and lead to strong deviations from Brownian behavior. But the skewness is enhanced considerably even for $\lambda \sim {}^{1}/_{t}$. Although the skewness does indeed decay with the number of samples as predicted by the Central Limit Theorem, the rate of convergence is dependent on the magnitude of the skewness. Hence, as skewness is enhanced, convergence (to a Gaussian) becomes quite slow (Figure 5.4), even without violating the central limit theorem or ergodicity. This result is quite intuitive as a sampling issue. As experimental setups (and consequently, this random variable) effectively are "snapshots" of the process and we have no memory effects built into our model, then each sample is effectively an independent identically distributed random variable representing diffusion and jumps occuring in a fixed amount of time (sampling time). The relationship between the sampling rate and the effective rate at which these jumps occur is therefore crucial in determining the statistics. In such cases, limited experimental data sets can still produce strongly skewed distributions for slopes of mean squared dispacement curves without violating ergodicity. This observation has been made in other branches of scientific literature (for instance, finance[37]) but seems to be underappreciated in this context. We can simulate the jump-diffusion process described

and compute the skewness as a function of experimentally tunable quantities (with one spatial and one temporal scale free, we set λ=1 and D=1 in the simulations). We immediately confirm that the skewness for the process with jumps is considerably higher than for pure diffusion (Figure 5.4A). Even though skewness for both processes decays with N and asymptotically converges to zero, the difference is large for practical data sizes. We can also examine the prediction from equation 4 that as dt becomes much smaller than $1/\lambda$, the skewness should increase. Our simulated skewness does indeed does grow as expected within a wide range of dt (Figure 5.4B). Of course, we have a technical limit on the number of samples (N) we can reasonably process, but we can fix N to be large and vary the sample time dt (meaning that the total simulation time N*dt also varies). Consequently, for any finite simulation, it is always possible to examine low enough values of dt, so that the length of simulation is not long enough to capture accurate statistics of the jump component and we extended our modeling up to this range of dt (Figure 5.4B). Lastly, we show that skewness estimation can be robust when the number of paths (M) is large (Figure 5.4C). In all cases, we observe a slight over-estimate for skewness, reflecting the bias of the estimating approach used here.

The fact that our observations for a complex system with a high and variable number of motors on a cargo can be reduced to a very simple theoretical picture of jump diffusion suggests that this may be a fairly common intracellular phenomenon. To test this possibility, we have examined a lipid droplet motility system in mammalian Cos-1 cells. Lipid droplet motility is known to be driven by kinesin-2 and dynein motors[38] and is also known to show a diverse array of phenotypes, from long distance directed motion to more stationary displacements (Figure 5.5). Moreover, lipid droplet motility in

mammalian cells has been used as a probe of viscoelasticity of the cytoskeleton[39]. Indeed, subdiffusive behavior has been found at short time scales but hints of linear MSD curves have been seen at longer time scales[39].

We examined the lipid droplet motility at long time scales only and focused on apparently diffusive transport; the MSDs which fit to the quadratic model better than the linear model using the Akaike information criterion were ignored in our analysis. The resulting tracks are not all stationary. As discussed above, linear or sub-diffusive MSD curves can arise from active motion if it is saltatory, or if it is a minor part of a longer record. All these cases are seen in Figure 5.5A. The average MSD curve is broadly consistent with linear trend (Figure 5.5B). Any minor sub-diffusive curvature for short lags is not significant, although such a feature would be expected from and consistent with prior report[39]. However, the distribution of apparent diffusion coefficients (Figure 5.5C) is inconsistent with Brownian motion and is instead highly skewed. The strong similarity between these observations and our *in-vitro* data is of course insufficient to infer the microscopic picture of lipid droplet motility in cells. It is, however, sufficient to call into question whether viscoelastic contributions can be unambiguously attributed to the cytoskeletal filaments or cytosol in general. They may be partially or even wholly due to the motor contribution instead. It is also sufficient to call into question whether cytoskeletal motor contribution to nanoscale biomechanics in cells is purely elastic[40].

In conclusion, we have demonstrated that tug of war events for cytoskeleton transport can lead to complex motile behaviors in the absence of the cytosol, in the absence of microtubule movement[5], and indeed even in the absence of multiple cytoskeletal filaments[6]. Some of the motility we observed (short lag times) is clearly in

the class of anomalous diffusion while longer lag time motility remains to be fully understood.

Cytoskeletal transport has often been conceptualized as a process of cargos getting trapped in small spatial compartments and occasional jumps between such compartments[e.g. 28]. Our work suggests that stationary segments of cytoskeletal cargo motion may not always be due to compartment trapping but dynamic tug-of-war trapping instead. In addition, models of molecular motor transport often assume motor crosslinks to be purely elastic springs[41,42]. This assumption is convenient and computationally efficient but a more detailed model may be warranted in the future.

On a practical level, we show that when dealing with cytoskeletal motility experiments which produce linear MSD curves, it is a good idea to examine the distribution of effective diffusion coefficients because devaitions from Gaussian (or high-degree-of-freedom chi-squared) behavior can be a signature of a complex diffusion process. We also show that varying temperature is an excellent and easily experimentally accessible technique for probing active contributions to single particle motion in the cytoskeletal context.

5.4 Materials and methods

●Bead assays: Taxol stabilized microtubules were deposited on a glass coverslip, washed, then the coverslip surface was blocked and the bead/motor sample was subsequently admitted into the flow cell, as previously described[43]. Briefly, glass coverslips were coated with poly-L-lysine, and attached to sapphire slides (Swiss Jewel Company, Philadelphia, PA) via double-sided tape (3M, Maplewood, MN). Taxol

stabilized microtubules (MT) were diluted into the flow buffer and then deposited into flow cell and incubated for 15 mins. The flow buffer was PMEE (35 mM Pipes, 5 mM MgSO4, 1mM EGTA, 0.5 mM EDTA) supplemented with 20 μM taxol and 1 mM GTP. Excess MTs were then washed away and the surface was blocked with buffer containing 22 mg/mL casein (Sigma-Aldrich, St. Louis, MO). Carboxylated Ø1 m polystyrene beads (Polysciences, Warrington, PA) were incubated with excess NCD N340K kinesin diluted in PMEE buffer augmented with 105 mM of NaCl, 5mM of ATP, and 5 mM Dithiothreitol and incubated at 4 C for 30 mins. Beads were observed to bind to microtubules without detachment during the entire observation period consistent with multiple NCD motors tethering the beads to microtubules. Control beads without NCD did not bind to microtubules in a parallel assay (data not shown).

●Imaging and temperature control: Motility data were collected in a biologically relevant temperature range as previously described[32]. Briefly, flow cells were constructed as usual but sapphire window was used in place of the cover glass. A customized Peltier thermoelectric stage (PE120; Linkam, Tadworth, UK) was placed in direct contact with the sapphire cover glass for maximum heat conductivity between the assay and the stage. Dry condenser was used to minimize thermal coupling to the microscope. Imaging was performed at ~20 frames per second. Bead positions were then extracted and analyzed via custom tracking software (Matlab, Mathworks, Natick, MA).

●MSD analysis for long lag times: Linear fits were performed for lag times between 1 and 3 seconds. Longer time lags were penalized in the fit because variance between MSDs for particle trajectories grows with lag[14]. Our regression also used inverse estimated variance as fitting weights[14] to improve estimation. A few exceptional

trajectories showed motion consistent with ballistic (constant velocity) transport. Akaike information criterion was used to filter out MSD curves which fit the quadratic model better than the linear one. Inclusion of such trajectories is somewhat ambiguous in principle, since a linear fit need not produce a meaningful estimate, but in practice it does not substantially alter the results above (not shown).

●Protein purification: N340K mutant of NCD with N-terminal 6xHis tag was bacterially expressed in BL21DE3. Lysis was accomplished by sonication for 45 mins at 4 °C. Lysis buffer: 50 mM Tris pH 7.5, 300 mM NaCl, 10% glycerol, 20 mM imidazole, 10 M PMSF, 2 mM bME with EDTA-free Roche mixture inhibitors. Cell lysis was followed by immobilized metal ion affinity chromatography purification (two washes and elution). Wash buffer 1: 50 mM Tris pH 7.5, 700 mM NaCl, 10% glycerol, 40 mM imidazole, 0.02% Triton X-100, 2 mM bME. Wash buffer 2: 50 mM Tris pH 7.5, 300 mM NaCl, 10% glycerol, 75 mM imidazole, 2 mM bME. Elution buffer: 25 mM Tris pH 7.5, 300 mM NaCl, 10% glycerol, 500 mM imidazole, 2 mM bME. Gene synthesis and purification were performed by Bionexus, Inc.

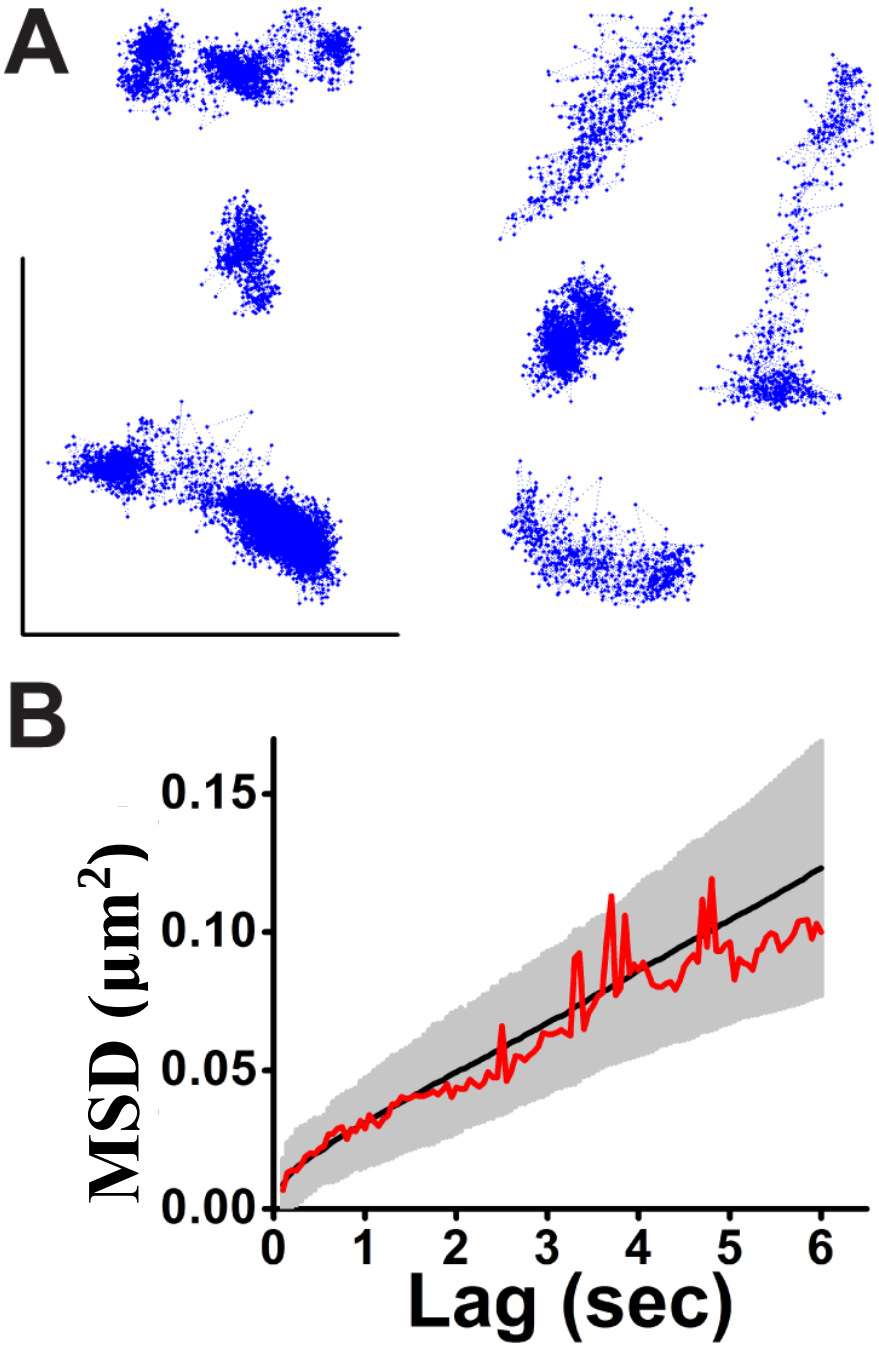

Figure 5.1 Bead motility at room temperature. (A) Representative tracks show non-negligible but slow motility which has a linear MSD for time lags above 1 sec (B). Time-averaged MSD curve (solid black) and associated 95% C.I. (grey region) are shown. The sample-averaged MSD (red) is not significantly different from time average. Scale bars in (A): 1 m.

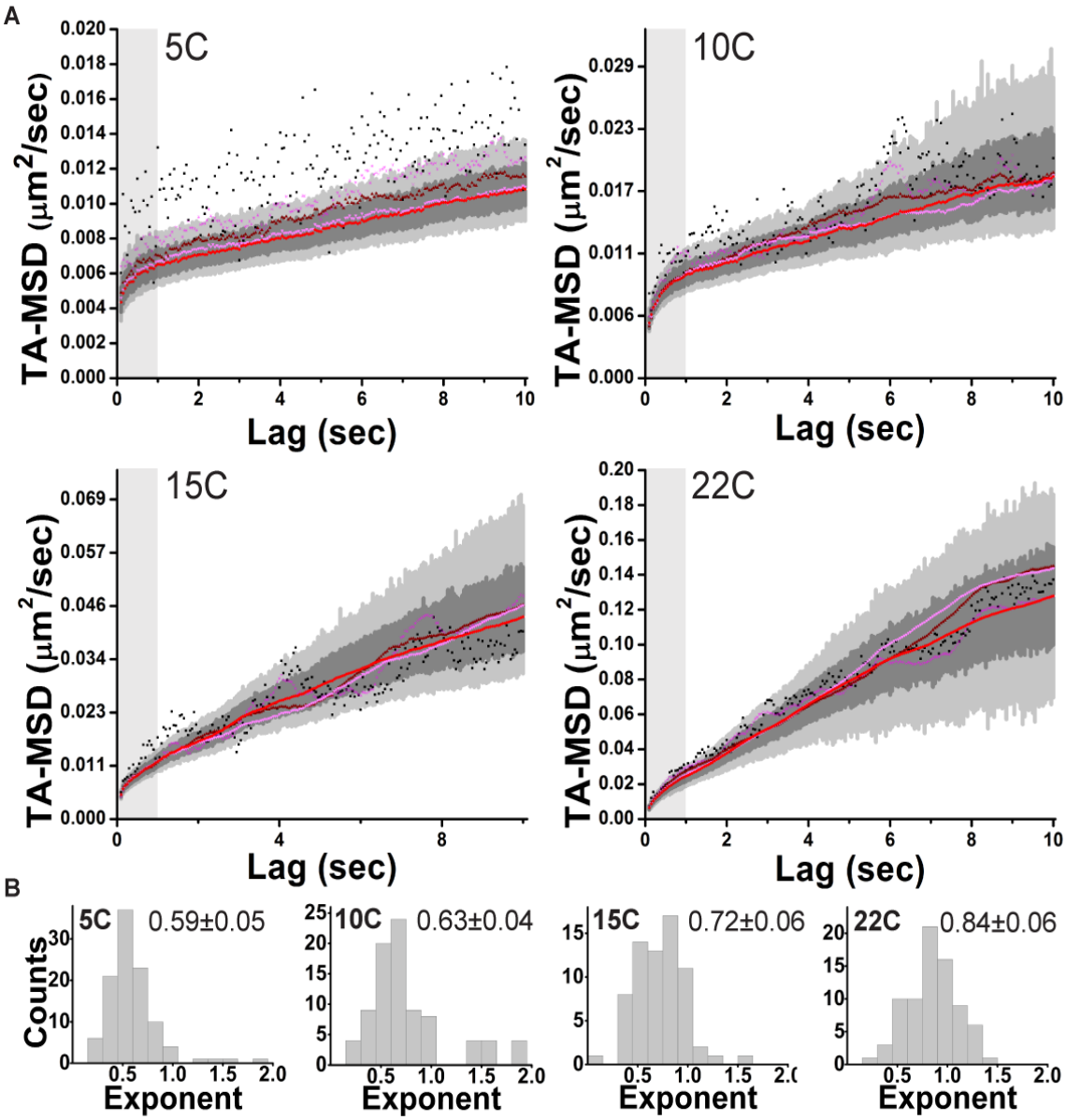

Figure 5.2. Anomalous features of bead motility. (A) TA-MSD curves were computed for 5, 10, 15, 22 C data as labeled. In each case average TA-MSD was computed for several measurement times: 0.05 sec (black), 0.5 sec (dark magenta), 2.5 sec (burgundy), 5 sec (light magenta), 10 sec (red). One sigma (0.32) and two sigma (0.05) C.I. were estimated for the 5 sec data via 1000 sample bootstrap for each lag point (dark and light grey respectively). (B) Sub-diffusive anomalous exponents for MSD records below 1 sec (grey region in (A)) at 5, 10, 15, 22 C as labeled. Peak locations and 0.05 C.I. are shown for each panel. Anomalous exponents were estimated via loglog linearization after adjustment for noise[44]

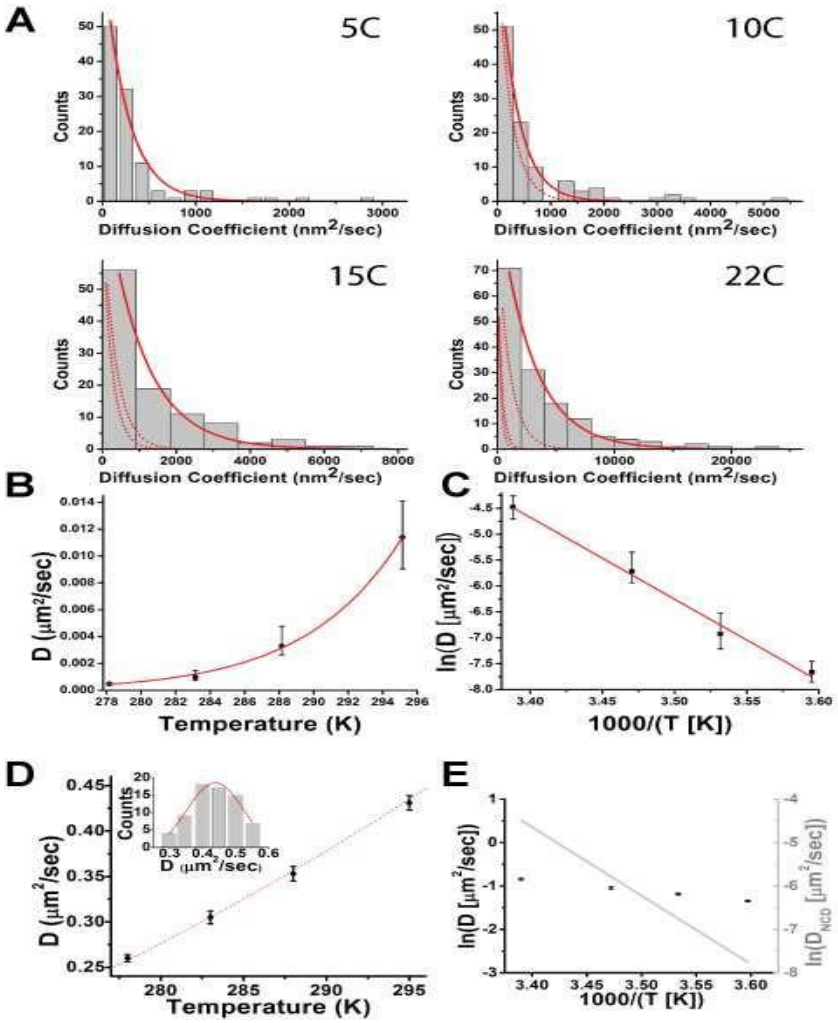

Figure 5.3 Temperature dependence of apparent diffusion coefficients. (A) Histograms of diffusion coefficients for 5, 10, 15, 22 °C are shown as labeled. In each panel, a fit to exponential density is shown (solid red). Because x-axis values needed to be rescaled for data at variable temperatures, fits to exponential densities at lower temperatures are shown for higher temperature panels (dashed red) for reference of overall scale. Characteristic diffusion coefficient for each temperature and a best fit Arrhenius curve (red) are shown on linear (B) and Arrhenius style (C) plots. For comparison, diffusion coefficients for free diffusion of 1μm diameter beads in water (D,E) show weak temperature dependence. Fit to Stokes-Einstein equation for bead radius 505 nm is shown (D, red dashed line); nominal bead radius is 499±19 nm. (inset) Histogram of diffusion coefficients at 22 °C and a Gaussian fit (red). (E) Arrhenius style plot: bead diffusion in water (black) is superimposed on linear trend for N340K NCD diffusion (C).

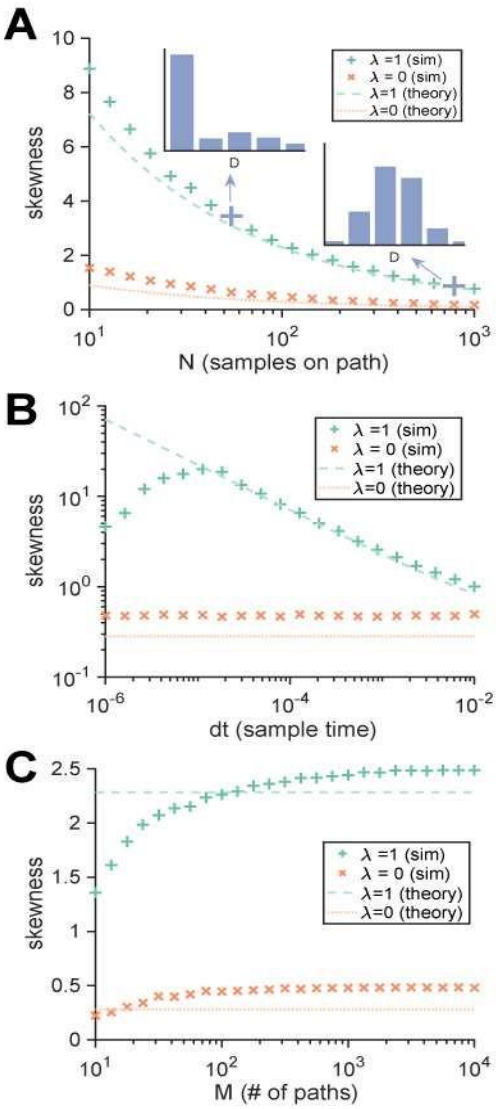

Figure 5.4 Analytic and simulation predictions for the skewness of the distribution of empirical diffusion coefficients. Classical diffusion (λ=0) and jump diffusion (λ=1) cases are shown. (A) Skewness decays asymptotically to zero as a function of the number of points on each path (N). Simulation results are slightly but consistently higher than analytic predictions due to estimator bias. (B) The skewness grows with the sampling rate following analytical curve. The effect of finite simulation size is seen for low dt. (C) Simulated skewness as a function of the number of trajectories (M) shows asymptotic convergence to analytic prediction (up to estimator bias) for large M. Analytic curves: dashed lines. Simulated results: crosses. Parameters (unless noted): D=1, M=1000, N=100, dt=1e-3, delta=0.8.

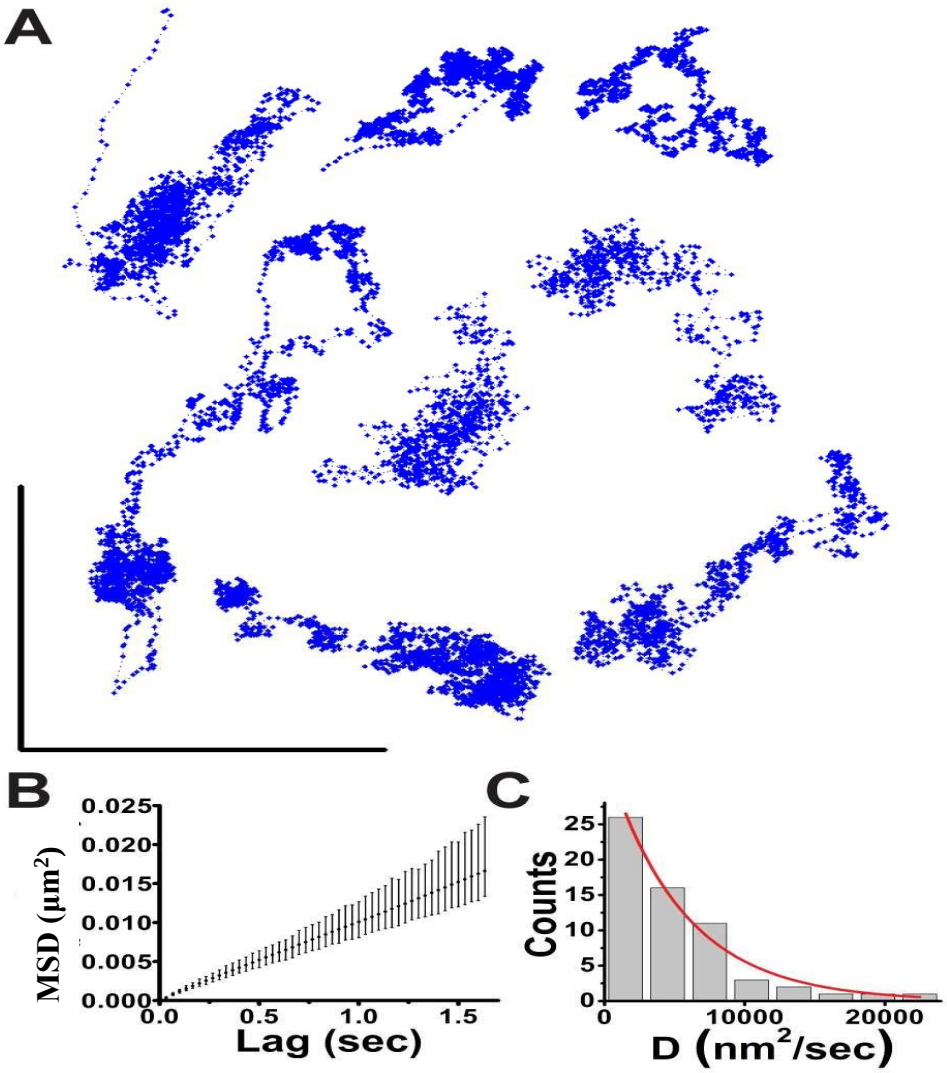

Figure 5.5 Apparently diffusive subset of lipid droplet motility in Cos-7 cells. (A) Representative droplet tracks at 37 °C (blue). (B) The average MSD curve and (C) the distribution of effective diffusion coefficients for lipid droplets which do not show active motion. Fit to exponential density is shown in red. Scale bars in (A): 1 μm.

5.5 Appendix

Appendix

Let $p(x,t)$ be the probability density of a jump-diffusion process in one dimension governed by the Fokker-Planck equation (1). We are interested in observations of the random variable D_s defined by equation (2). Moments of D_s can be related to moments of x by

$$\langle {D_s}^j \rangle = \frac{1}{(2t)^j}\langle x^{2j}\rangle = \frac{\mu_{2j}}{(2t)^j}, \qquad \mu_j \coloneqq \langle x^j \rangle,$$

Multiplying (1) by x^j and integrating, we find the explicit evolution of these moments

$$\frac{\mathrm{d}\mu_j}{\mathrm{d}t} = Dj(j-1)\mu_{j-2} + 2\lambda \sum_{k=1}^{\lfloor j/2 \rfloor} \binom{j}{2k} \delta^{2k}\mu_{j-2k},$$

where $\lfloor \cdot \rfloor$ is the floor operator.

This system of ordinary differential equations is "lower triangular" in the sense that μ_j only depends on μ_k for $k < j$. That is, we can solve these moments equations sequentially. For the first moment, we have $\mathrm{d}\mu_1/\mathrm{d}t = 0$, so that $\mu_1 \equiv 0$. This is intuitive, as diffusion and symmetric jumps produce no displacement on average.

The remaining equations of interest are

$$\begin{aligned}
\frac{\mathrm{d}\mu_2}{\mathrm{d}t} &= 2D + 2\lambda\delta^2 \\
\frac{\mathrm{d}\mu_4}{\mathrm{d}t} &= 12[D + \lambda\delta^2]\mu_2 + 2\lambda\delta^4 \\
\frac{\mathrm{d}\mu_6}{\mathrm{d}t} &= 30[D + \lambda\delta^2]\mu_4 + 30\lambda\delta^4\mu_2 + 2\lambda\delta^6
\end{aligned}$$

As highlighted in the main text, the mean-squared displacement μ_2 is indeed still linear even with the jump component, and the estimated diffusivity from this linear MSD is

$$\langle D_s \rangle = \frac{\mu_2}{2t} = D + \lambda\delta^2.$$

We can proceed on to the variance, using

$$\widetilde{\sigma}^2 \coloneqq \mathrm{var}[D_s] = \frac{1}{(2t)^2}[\mu_4 - \mu_2^2] = 2\delta^4\lambda^2 + 2D^2 + 4\delta^2 D\lambda + \frac{\delta^4\lambda}{2t}.$$

Notably, if $\lambda = 0$ (i.e. no jumps, classical diffusion), there is no dependence on t (the sampling time). However, with $\lambda \neq 0$, $\widetilde{\sigma}^2 \to \infty$ as $t \to 0$.

The next moment, the skewness, is found to be

$$\widetilde{g} \coloneqq \mathrm{skew}[D_s] = \frac{32D^3t^2 + 96\delta^2D^2\lambda t^2 + 24\delta^4 D\lambda t(4\lambda t + 1) + \delta^6\lambda(8\lambda t(4\lambda t + 3) + 1)}{t(4D^2t + 8\delta^2 D\lambda t + \delta^4\lambda(4\lambda t + 1))\sqrt{8D^2 + 16\delta^2 D\lambda + \frac{2\delta^4\lambda(4\lambda t + 1)}{t}}}.$$

Similar to the previous moment, in the absence of jumps ($\lambda = 0$), there is no t dependence. However, with $\lambda \neq 0$, as $t \to 0$, then $\widetilde{g} \to +\infty$.

We can relate d to experimentally observed quantities by considering the observations of a single trajectory denoted

$$\{x_1, x_2, \dots, x_N\},$$

where each observation occurs at a fixed time interval Δt, so $x(i) \approx x_0 + i\Delta t$. Then, define each squared displacement, scaled by time, denoted ${D_s}^{(i)}$

$${D_s}^{(i)} \coloneqq \frac{[x_i - x_{i-1}]^2}{2\Delta t}.$$

This is inherently an estimate of the diffusivity. Although the actual procedure is considerably more complex, we can use these observations as an estimator for D along an observed trajectory

$$D_{est} = \frac{1}{N}\sum_{i=1}^{N} {D_s}^{(i)},$$

Because each ${D_s}^{(i)}$ is independent, the statistics of the collection of diffusion coefficients over several paths become

$$\langle D_{est} \rangle = \langle D_s \rangle, \qquad \mathrm{var}[D_{est}] = \tilde{\sigma}^2 / N, \qquad \mathrm{skew}[D_{est}] = \tilde{g} / \sqrt{N}.$$

The main difference is that in the actual procedure, samples are *not* independent and introduce correlation. Consequently, these are lower bounds for the variance and skewness.

5.6 References

1. Olaolu Osunbayo *et al.* Cargo transport across microtubule intersections: evidence for prolonged tug of war. *Biophys. J.* (2015).

2. Ross, J. L., Shuman, H., Holzbaur, E. L. F. & Goldman, Y. E. Kinesin and dynein-dynactin at intersecting microtubules: motor density affects dynein function. *Biophys. J.* **94,** 3115–3125 (2008).

3. Lombardo, A. T. *et al.* Myosin Va molecular motors manoeuvre liposome cargo through suspended actin filament intersections *in vitro*. *Nat. Commun.* **8,** ncomms15692 (2017).

4. Vershinin, M., Carter, B. C., Razafsky, D. S., King, S. J. & Gross, S. P. Multiple-motor based transport and its regulation by Tau. *Proc. Natl. Acad. Sci. U. S. A.* **104,** 87–92 (2007).

5. Kulić, I. M. *et al.* The role of microtubule movement in bidirectional organelle transport. *Proc. Natl. Acad. Sci.* **105,** 10011–10016 (2008).

6. Scholz, M. *et al.* Cycling State that Can Lead to Glassy Dynamics in Intracellular Transport. *Phys. Rev. X* **6,** 011037 (2016).

7. Vale, R. D. The molecular motor toolbox for intracellular transport. *Cell* **112,** 467–480 (2003).

8. Cooper, J. R. & Wordeman, L. The diffusive interaction of microtubule binding proteins. *Curr. Opin. Cell Biol.* **21,** 68–73 (2009).

9. Jülicher, F & Prost, J. Cooperative molecular motors. *Phys. Rev. Lett.* **75,** 2618–2621 (1995).

10. Hendricks, A. G., Holzbaur, E. L. F. & Goldman, Y. E. Force measurements on cargoes in living cells reveal collective dynamics of microtubule motors. *Proc. Natl. Acad. Sci.* **109,** 18447–18452 (2012).

11. Soppina, V., Rai, A. K., Ramaiya, A. J., Barak, P. & Mallik, R. Tug-of-war between dissimilar teams of microtubule motors regulates transport and fission of endosomes. *Proc. Natl. Acad. Sci. U. S. A.* **106,** 19381–19386 (2009).

12. Lin, C. *et al.* Active diffusion and microtubule-based transport oppose myosin forces to position organelles in cells. *Nat. Commun.* **7,** ncomms11814 (2016).

13. Qian, H., Sheetz, M. P. & Elson, E. L. Single particle tracking. Analysis of diffusion and flow in two-dimensional systems. *Biophys. J.* **60,** 910–921 (1991).

14. Saxton, M. J. Single-particle tracking: the distribution of diffusion coefficients. *Biophys. J.* **72,** 1744–1753 (1997).

15. Metzler, R., Jeon, J.-H., Cherstvy, A. G. & Barkai, E. Anomalous diffusion

models and their properties: non-stationarity, non-ergodicity, and ageing at the centenary of single particle tracking. *Phys. Chem. Chem. Phys.* **16,** 24128–24164 (2014).

16. Wang, B., Anthony, S. M., Bae, S. C. & Granick, S. Anomalous yet Brownian. *Proc. Natl. Acad. Sci.* **106,** 15160–15164 (2009).

17. Chechkin, A. V., Seno, F., Metzler, R. & Sokolov, I. M. Brownian yet Non-Gaussian Diffusion: From Superstatistics to Subordination of Diffusing Diffusivities. *Phys. Rev. X* **7,** 021002 (2017).

18. Shinkai, S. & Togashi, Y. Energetics of single active diffusion trajectories. *EPL Europhys. Lett.* **105,** 30002 (2014).

19. Vandebroek, H. & Vanderzande, C. The effect of active fluctuations on the dynamics of particles, motors and hairpins. *ArXiv161102123 Cond-Mat Physicsphysics* (2016).

20. Robson, A., Burrage, K. & Leake, M. C. Inferring diffusion in single live cells at the single-molecule level. *Philos. Trans. R. Soc. Lond. B. Biol. Sci.* **368,** 20120029 (2013).

21. Model Comparison and Assessment for Single Particle Tracking in Biological Fluids: Journal of the American Statistical Association: Vol 111, No 516. Available at: http://amstat.tandfonline.com/doi/abs/10.1080/01621459.2016.1158716. (Accessed: 29th June 2017)

22. Endow, S. A. & Higuchi, H. A mutant of the motor protein kinesin that moves in both directions on microtubules. *Nature* **406,** 913–916 (2000).

23. Foster, K. A., Mackey, A. T. & Gilbert, S. P. A mechanistic model for Ncd directionality. *J. Biol. Chem.* **276,** 19259–19266 (2001).

24. Furuta, K. & Toyoshima, Y. Y. Minus-end-directed motor Ncd exhibits processive movement that is enhanced by microtubule bundling in vitro. *Curr. Biol. CB* **18,** 152–157 (2008).

25. Wendt, T. G. *et al.* Microscopic evidence for a minus-end-directed power stroke in the kinesin motor ncd. *EMBO J.* **21,** 5969–5978 (2002).

26. Butterfield, A. E., Stewart, R. J., Schmidt, C. F. & Skliar, M. Bidirectional power stroke by ncd kinesin. *Biophys. J.* **99,** 3905–3915 (2010).

27. Snider, J. *et al.* Intracellular actin-based transport: How far you go depends on how often you switch. *Proc. Natl. Acad. Sci. U. S. A.* **101,** 13204–13209 (2004).

28. Tabei, S. M. A. *et al.* Intracellular transport of insulin granules is a subordinated random walk. *Proc. Natl. Acad. Sci.* **110,** 4911–4916 (2013).

29. Weigel, A. V., Simon, B., Tamkun, M. M. & Krapf, D. Ergodic and nonergodic processes coexist in the plasma membrane as observed by single-molecule tracking.

Proc. Natl. Acad. Sci. **108,** 6438–6443 (2011).

30. Fink, A. L. & Cartwright, S. J. Cryoenzymology. *CRC Crit. Rev. Biochem.* **11,** 145–207 (1981).

31. Kawaguchi, K. & Ishiwata, S. Temperature dependence of force, velocity, and processivity of single kinesin molecules. *Biochem. Biophys. Res. Commun.* **272,** 895–899 (2000).

32. Hong, W., Takshak, A., Osunbayo, O., Kunwar, A. & Vershinin, M. The Effect of Temperature on Microtubule-Based Transport by Cytoplasmic Dynein and Kinesin-1 Motors. *Biophys. J.* **111,** 1287–1294 (2016).

33. Hinrichs, M. H. *et al.* Tau Protein Diffuses along the Microtubule Lattice. *J. Biol. Chem.* **287,** 38559–38568 (2012).

34. Bustamante, C., Chemla, Y. R., Forde, N. R. & Izhaky, D. Mechanical processes in biochemistry. *Annu. Rev. Biochem.* **73,** 705–748 (2004).

35. Uemura, S. *et al.* Kinesin–microtubule binding depends on both nucleotide state and loading direction. *Proc. Natl. Acad. Sci.* **99,** 5977–5981 (2002).

36. *Stochastic Methods - A Handbook for the Natural and Social | Crispin Gardiner | Springer*.

37. Aït-Sahalia, Y. Disentangling diffusion from jumps. *J. Financ. Econ.* **74,** 487–528 (2004).

38. Herms, A. *et al.* AMPK activation promotes lipid droplet dispersion on detyrosinated microtubules to increase mitochondrial fatty acid oxidation. *Nat. Commun.* **6,** ncomms8176 (2015).

39. Yamada, S., Wirtz, D. & Kuo, S. C. Mechanics of Living Cells Measured by Laser Tracking Microrheology. *Biophys. J.* **78,** 1736–1747 (2000).

40. Goychuk, I., Kharchenko, V. O. & Metzler, R. Molecular motors pulling cargos in the viscoelastic cytosol: how power strokes beat subdiffusion. *Phys. Chem. Chem. Phys. PCCP* **16,** 16524–16535 (2014).

41. Berger, F., Keller, C., Klumpp, S. & Lipowsky, R. Distinct transport regimes for two elastically coupled molecular motors. *Phys. Rev. Lett.* **108,** 208101 (2012).

42. Kunwar, A., Vershinin, M., Xu, J. & Gross, S. P. Stepping, strain gating, and an unexpected force-velocity curve for multiple-motor-based transport. *Curr. Biol. CB* **18,** 1173–1183 (2008).

43. Smith, T. E. *et al.* Single-molecule inhibition of human kinesin by adociasulfate-13 and -14 from the sponge Cladocroce aculeata. *Proc. Natl. Acad. Sci. U. S. A.* **110,** 18880–18885 (2013).

44. Kepten, E., Weron, A., Sikora, G., Burnecki, K. & Garini, Y. Guidelines for the

Fitting of Anomalous Diffusion Mean Square Displacement Graphs from Single Particle Tracking Experiments. *PLOS ONE* **10,** e0117722 (2015).

CHAPTER 6

CONCLUSION

The work presented in this dissertation focuses on how intracellular cargos remain immotile and the development of techniques to study this process. While most studies of intracellular transport have focused on cargos that move, less attention has been paid to cargos that do not move which can constitute a significant percentage of intracellular transport. In the following paragraphs, I will present summaries and impacts of Chapter 2, Chapter 3, Chapter 4, and Chapter 5.

Microtubule (MT) cytoskeleton is a complex network with multiple intersections at different angles [1,2]. Motor driven cargos will have to navigate multiple intersections to get to their destinations. These multiple intersections could be a regulator of intracellular transport. How kinesin motor driven cargos behave at intersection had been controversial. A study [3] argues that a significant fraction of kinesin driven cargos pause at intersections and most were able to switch only after deformation of the MT suggesting a tug-of-war. On the other hand, a paper [4], argues that kinesin driven cargos rarely pause. My work in Chapter 2 suggests that differences in both results might be due to the angle of intersecting microtubules. I studied pause duration at intersecting MTs at various angles and found that most long pauses occur at acute angle of counter aligned intersecting MTs. I also quantified theses pauses in terms of number of kinesin and affinity of kinesin, and my results suggests that the number of kinesins and the affinity of kinesin for MT can

regulate the duration of these pauses.

Another reason that has been postulated in the literature for the origin of pauses at intersections is that a traversing MT can be a significant barrier for molecular motor driven cargos at intersections *in-vivo* [5]. In addition to the barrier effect [5], the data presented in Chapter 2 suggest that a cargo can simultaneously engage on more than one MT and crosslink them in a tug-of-war *in-vivo*. The tug-of-war *in-vivo* is evinced by the deformation pattern of MT that suggests engaged motors are trying to move in different directions. Hence, Chapter 2 established the importance of microtubule (MT) geometry and bending in the routing of cargos throughout the cell.

The work mentioned in the previous paragraph was done in two-dimensional space with MT attached to a glass slide. In order to investigate the importance of MT geometry in physiologically relevant three-dimensional space *in-vitro*, a novel technique is needed for there is no prior technique that can reliably and easily accomplish this. I have helped develop a technique to accomplish this.

The ability to precisely manipulate and assemble MT in 3D has important implications for both engineering and scientific purposes. One notable challenge for nanotechnology is to design and assemble a "molecular shuttle" [6] that can reliably transport nanoscale quantities of materials in a regulated way. MT system could be an ideal "molecular shuttle" for nanotechnological applications as it evolved primarily to transport materials within the cell. MT-based systems have been designed as a proof of concept for "molecular shuttle" [7–10]. These methods have fixed and limited geometry with the molecular motors attached to a surface and overlaid with gliding MTs, or an assembly involving suspended MTs attached to ridges. These approaches are not

scalable and the geometry cannot rapidly be modified or precisely controlled in 3D. Therefore, prior approaches severely limit the ability to assemble customized MT network in 3D. In Chapter 3, we presented a novel technique that can rapidly and precisely manipulate multiple MTs with high fidelity using holographic optical tweezers in order to create a complex 3D MT network. This could have important nanotechnological applications for lab on chip devices, biosensors, *etc*. For large-scale technological application of MT system as a molecular "shuttle", the problem of protein degradation over time needs to be overcome and 3D assembly of MT networks via holographic tweezers we presented in Chapter 3 might need to be fully automated.

The ability to assemble MT networks in 3D also has important implications for science. The interest in how cargos navigate complex geometry of MT is growing [5,11] and how complex network of MT in 3D regulates intracellular transport is not well understood. In order to study the effect of complex geometry of MTs on motor driven cargos, there is often a need for a parallel and controlled *in-vitro* measurement. *In-vitro* reconstitution has a long history in cytoskeleton research [12] and *in-vitro* measurements remain a common approach to elucidate intracellular transport [13]. My contribution to the work in Chapter 3 now enables scalable, rapid, and faithful assemblage of MT networks in 3 dimensions, where the angles and the height separation can be controlled. I worked with Jared Bergman in Chapter 3 of this dissertation and he has taken the work even further by studying how the 3D geometric parameter of MT regulates kinesin driven cargos.

The motivating biological question for the work in Chapter 4 is to understand the origin of shut down of neuronal transport at temperature below 12 ^{0}C [14–16] and other low

temperature dependent transport phenotypes. Many organisms including hibernating mammals [17] survive temperature as low as 5 ^{0}C. This raises the question of how cold transport block happens and how it is overcome in some cold adapted organisms. It is known that the cold transport block is not due primarily to MT depolymerization [16]. I was interested in how temperature affects the ensemble properties of intracellular transport, and how this could lead to immobility. Therefore, we started with the basic question on how low temperature changes the properties of a single biological motor. We showed in Chapter 4 that kinesin and dynein have a completely different mechanochemical response to cold temperature within the range of temperature we measured. We found that rat cytoplasmic dynein, an organism not adapted to cold, switches to very high activation energy at about 15 ^{0}C; for yeast cytoplasmic dynein, the switch to high activation energy occurs at 8 ^{0}C. Kinesin-1 activation energy remains the same within the temperature range measured. These results suggest that dynein is the main modulator of low temperature transport phenotype observed at less than 12 ^{0}C. A future research goal might be to test the hypothesis that the activation energy of dynein switches to high value in other cold adapted organisms at temperature much lower than 15 ^{0}C and investigate the structural component of dynein that leads to these different temperature dependent switches. Another future direction might also be to test if the dynein switch to high activation energy can be regulated in hibernating mammals.

In Chapter 5, I continued my study on cargos that do not move. One reason for this immotile cargo fraction is due to opposite directed molecular motors engaged in a tug-of-war. Another possible reason for immotile fraction could be due to thermally activated passive diffusion [18]. Distinguishing these two processes, (1) active “diffusive”

processes resulting from motors activities from (2) passive diffusion, is critical as it leads to different areas of further investigation and it also limits the type of questions that can be asked. For example, if the immotile fraction is governed predominantly by passive diffusion, then questions relating to rheological properties of the cell could be asked. On the other hand, if the process is governed predominantly by active processes, then questions relating to the properties and regulations of the motors involved could be further investigated. Therefore, the very first question in study of immotile fraction should be how to easily tell apart these two processes. This work in Chapter 5 presents a noninvasive approach which uses variable temperature measurement and quantitative analysis to tell apart motor driven "active diffusion" from passive diffusion. In the minimal *in-vitro* tug-of-war system we constructed, I found that the spread of displacements of tug-of-wars, as measured by diffusion coefficients, is temperature dependent and obeys Arrhenius kinetic with activation energy twice as much as previously observed in Chapter 4 for the conventional kinesin. In addition, we showed in chapter five that these tug-of-war processes display complex behaviors which can be used to quickly identify "active" tug-of-war from passive diffusion.

One important complex behavior that can be used to identify tug-of-war is the skewed distribution of the diffusion coefficients. The skewness in this case represents an apparent deviation from the central limit theorem. In order to study the origin of the skewness generalizable to all tug-of-war models, we worked with Chris Miles, in Dr. James Keener group, in the Department of Mathematics at the University of Utah. We constructed a minimum theoretical model with a Fokker-Planck equation which contains bi-directional enzymatic jumps (e.g. powerstroke events) and some elements of passive

diffusion. These events are expected to be present in every molecular motor tug-of-war system. The mathematical model reveals that the mean square displacement (MSD) of the tug-of-war can be still be linear. The mathematical model also reveals that the distribution of diffusion coefficients, though asymptotically a normal distribution, might be skewed for practical purposes as the convergence is much slower for tug-of-war than for passive diffusion. The results in Chapter 5 could be applied in the studies of immotile fraction in different types of cargos, in different types of cells and in different types of organisms.

6.1 References

1. Zhang, Z., Nishimura, Y. & Kanchanawong, P. Extracting microtubule networks from superresolution single-molecule localization microscopy data. *Mol Biol Cell* **28,** 333–345 (2017).

2. Huang, B., Jones, S. A., Brandenburg, B. & Zhuang, X. Whole-cell 3D STORM reveals interactions between cellular structures with nanometer-scale resolution. *Nat Methods* **5,** 1047–1052 (2008).

3. Vershinin, M., Carter, B. C., Razafsky, D. S., King, S. J. & Gross, S. P. Multiple-motor based transport and its regulation by Tau. *Proc Natl Acad Sci U S A* **104,** 87–92 (2007).

4. Ross, J. L., Shuman, H., Holzbaur, E. L. F. & Goldman, Y. E. Kinesin and dynein-dynactin at intersecting microtubules: motor density affects dynein function. *Biophys J* **94,** 3115–3125 (2008).

5. Bálint, Š., Verdeny Vilanova, I., Sandoval Álvarez, Á. & Lakadamyali, M. Correlative live-cell and superresolution microscopy reveals cargo transport dynamics at microtubule intersections. *Proc Natl Acad Sci U S A* **110,** 3375–3380 (2013).

6. Silvi, S., Venturi, M. & Credi, A. Artificial molecular shuttles: from concepts to devices. *J. Mater. Chem.* **19,** 2279 (2009).

7. Hess, H. & Vogel, V. Molecular shuttles based on motor proteins: active transport in synthetic environments. *Reviews in Molecular Biotechnology* **82,** 67–85 (2001).

8. Ramachandran, S., Ernst, K.-H., Bachand, G. D., Vogel, V. & Hess, H. Selective loading of kinesin-powered molecular shuttles with protein cargo and its application to biosensing. *Small* **2,** 330–334 (2006).

9. Isozaki, N. *et al.* Sorting of molecular shuttles by designing electrical and mechanical properties of microtubules. *BioRxiv* (2017). doi:10.1101/107458

10. Tarhan, M. C., Orazov, Y., Yokokawa, R., Karsten, S. L. & Fujita, H. Suspended microtubules demonstrate high sensitivity and low experimental variability in kinesin bead assay. *Analyst (Lond)* **138,** 1653–1656 (2013).

11. Osunbayo, O. *et al.* Cargo transport at microtubule crossings: evidence for prolonged tug-of-war between kinesin motors. *Biophys J* **108,** 1480–1483 (2015).

12. Szent-Györgyi, A. The contraction of myosin threads. *Stud Inst Med Chem Univ Szeged* **1**:17–26 (1942).

13. Vale, R. D. Preface: the role of reconstitution in cytoskeleton research. *Meth Enzymol* **540,** xix–xxiii (2014).

14. Goldberg, D. J., Schwartz, J. H. & Sherbany, A. A. Kinetic properties of normal and perturbed axonal transport of serotonin in a single identified axon. *J Physiol (Lond)* **281,** 559–579 (1978).

15. Cancalon, P. Influence of temperature on various mechanisms associated with neuronal growth and nerve regeneration. *Prog Neurobiol* **25**, 27-92 (1985).

16. Brimijoin, S., Olsen, J. & Rosenson, R. Comparison of the temperature-dependence of rapid axonal transport and microtubules in nerves of the rabbit and bullfrog. *J Physiol (Lond)* **287,** 303–314 (1979).

17. Carey, H. V., Andrews, M. T. & Martin, S. L. Mammalian hibernation: cellular and molecular responses to depressed metabolism and low temperature. *Physiol Rev* **83,** 1153–1181 (2003).

18. Cooper, J. R. & Wordeman, L. The diffusive interaction of microtubule binding proteins. *Curr Opin Cell Biol* **21,** 68–73 (2009).